Characterization and Optimization of a Single-CCD Concept for the Pointing of Medium-Sized Telescopes (MSTs) for the Cherenkov Telescope Array (CTA)

Master's Thesis in Physics

Presented by
Yu Wun Wong
28 September 2018

Erlangen Centre for Astroparticle Physics
Friedrich-Alexander-Universität Erlangen-Nürnberg

Supervisor: Prof. Dr. Christopher van Eldik
Second Referee: Prof. Dr. Stefan Funk

Abstract

The Cherenkov Telescope Array (CTA) is the next generation ground-based observatory for the very-high-energy gamma-ray astronomy. It allows the detection of the gamma-ray in the energy regime from 20 GeV to 300 TeV, which will expand the current catalog by tenfold.

To determine the direction of a gamma quantum, it is crucial to carry out pointing calibration for telescopes, which is a correction for transforming a position in the telescope camera focal plane to sky coordinates. To do so, a single CCD-camera will be mounted on the mirror dish and track the pointing direction by taking night-sky images along with the telescope, aiming at the pointing accuracy of < 7". In this thesis, the pointing solution using a single CCD-camera for the Medium-Sized Telescopes (MSTs) for the CTA is investigated. This includes testing the image aberrations due to CCD-chip expansion and evaluating the performance of the camera housing. Finally, the pointing ability of the CCD-camera is examined on simulated and real images using an new software library **libpointingMST**.

It is found that the pointing center of the CCD-camera will shift for 1.6" if the chip temperature changes for 5 °C. Yet the housing ensures a stable chip temperature at -23 °C throughout the outdoor nighttime measurement in La Palama. It is determined that the star extraction efficiency from **libpointingMST** is 10 % higher than that from **astrometry.net**. By using **libpointingMST** in the reconstructions that include the mask area, the precise reconstruction (< 7") efficiency in the simulation reaches 71.6 % if the CCD-camera points with an elevation > 24° and 90 % if it points with an elevation > 35 °.

Table of contents

1 Motivation 1

2 Introduction to CTA 3

3 Pointing Calibration 9
- 3.1 Mispointing of Telescopes . . . 9
- 3.2 Calibration Method . . . 11
  - 3.2.1 Pointing Runs . . . 11
  - 3.2.2 Two-CCD Concept . . . 12
  - 3.2.3 Single-CCD Concept . . . 14

4 CCD-Camera Calibration 16
- 4.1 Working Principle of the CCD-Chip . . . 16
- 4.2 CCD-Chip Expansion Test . . . 17
  - 4.2.1 Set Up and Procedures . . . 18
  - 4.2.2 Result . . . 19
  - 4.2.3 Remark . . . 21
- 4.3 Summary . . . 22

5 Housing Characterization 23
- 5.1 Hardware . . . 23
  - 5.1.1 Housing Design . . . 23
  - 5.1.2 Dew Phenomenon and Glass Heater Design . . . 25
- 5.2 Chamber Measurements . . . 26
  - 5.2.1 Glass Heater Switch On Point . . . 27
  - 5.2.2 Optimization of the Chip Temperature . . . 29
  - 5.2.3 Stability of the Chip Temperature . . . 32
- 5.3 Outdoor Measurements . . . 34
  - 5.3.1 Dew Point and Stability Test . . . 35

5.4 Test Run at La Palma 38
5.5 Summary 39

6 Pointing Simulation 40
6.1 Workflow of Pointing Reconstruction 40
6.2 Workflow of Simulation 42
6.3 Star Extraction 44
6.3.1 Variation of Exposure Time 47
6.3.2 Parameter Optimization 48
6.3.3 Performance Comparison 50
6.4 Pointing 54
6.4.1 Problem of Fluctuating Matching Efficiency 56
6.4.2 Variation of Exposure Time 60
6.4.3 Fitting Iterations 61
6.4.4 Performance 63
6.5 Application on Real Images 74
6.6 Chip Expansion on Simulation 77
6.7 Summary 78

7 Summary and Outlook 80

References 82

Appendix A CCD-Camera Specifications 84

Appendix B Parameters for the Simulation 87

Appendix C Parameter Optimization for libpointingMST 88

Appendix D Nonlinear Optimization for the Fitting 89

Chapter 1

Motivation

Very-high-energy (VHE) gamma-ray astronomy, with energy ranging from 100 GeV to 100 TeV, is a highly motivated field for scientific research. For centuries, astronomers have had investigated the universe by looking at the optical light transmitted from sources on the sky. Not until 20th century, the modern astronomical achievement allows us the opportunity to investigate invisible parts, for the human eyes, of our Universe through the electromagnetic spectrum captured by telescopes that are sensitive to different wavelengths. The gamma-ray is especially interesting for astronomers as it is the latest new waveband for the exploration and gives a clue on many physics problems.

First, it gives a hint on the origin of the cosmic-rays, an important question that has been asked since their discovery by Hess in 1912. Since the cosmic-rays are charged particles, their paths are deflected by the magnetic field of the Galaxy and make it impossible to deduce their origin. However the VHE gamma-rays that are produced along with the cosmic-rays can travel straight in space and thus allows accurate determination of the production sites of these high energy cosmic-rays. Second, VHE gamma-rays are produced by high energy subatomic particles in the violent environment, namely through the interaction of accelerated hadrons, bremsstrahlung and the inverse Compton scattering of accelerated leptons (Stecker et al. [24], Aharonian [1]). Thus the detection of VHE gamma-rays reveals the mysterious non-thermal sources that accelerate particles to TeV energies, including supernova remnants, pulsar wind nebulae and extragalactic sources like active galactic nuclei. This facilitates the completion of the TeV universe survey. Third, the VHE gamma-rays can probe the frontier physics that is beyond the Standard Model, including the search for dark matter and the study of the extragalactic background light and cosmic void.

The current instruments with Imaging Atmospheric Cherenkov Telescope (IACT) systems, including H.E.S.S., MAGIC and VERITAS, consist of 2-5 telescopes have detected over 150 gamma ray sources (Oakes et al. [18]). Yet this is just a tip of the iceberg as the sensitivity of the current IACTs is limited by for example the background induced by air showers from cosmic rays (Ambrogia et al. [2]). To have a in-depth understanding of the gamma-ray sources, the next-generation ground-based gamma-ray observatory CTA (Cherenkov Telescope Array) aiming at the cosmic gamma radiation with energies from 20 GeV to 300 TeV has an order of magnitude more telescopes is under pre-construction, giving better angular resolution, larger effective area and improved sensitivity (CTAConsortium [6]).

To determine the direction of a gamma quantum, it is crucial to carry out pointing calibration for telescopes. Pointing is an offline correction for transforming a position in the telescope camera focal plane to a position on the sky (Gaug [8]). This is a very important task for the whole CTA project since the achievement of the scientific goals is based on the reconstruction ability for the precise incoming direction of the gamma quantum and this is directly related to the pointing precision of the telescope. Since the telescopes might be misaligned, the pointing cannot rely on its axes position. Instead the pointing will be done by equipping optical CCD-cameras to the mirror dish of the telescopes, in which they will track the pointing direction by taking night-sky images along with the telescopes. Thus it is important to evaluate the working ability of the CCD-camera in order to ensure the pointing direction of the telescopes.

This thesis is focused on the pointing solution using the single-CCD camera for the MSTs. The single-CCD is an new calibration concept that reduces operation costs and calibration complexity. In this thesis, the single-CCD camera concept is tested, this includes the testing of image aberrations due to the CCD-chip expansion and of how well the housing of the CCD-camera can provide an ultimate working environment for the CCD-camera. Finally, the pointing ability of the CCD-camera is examined using simulated and real images based on the reconstruction algorithm written by Domenico Tiziani called **libpointingMST**. In the next chapter, a more detailed description on the CTA and its working principle will be presented.

Chapter 2

Introduction to CTA

Gamma-rays cannot be directly detected on the ground since they will be absorbed by the atmosphere. Yet when gamma rays interact with the atmosphere, this interaction creates a subatomic particle cascade (electrons and positrons) as shown in Fig. 2.1, which will last until the ionization losses are equivalent to the radiative losses. Each electron loses half of its energy on average after a depth of $R = X_0 \ln 2$, where X_0 is the electromagnetic radiation length related to the atmospheric density (Mazin [15]). When these charged secondary particles pass through the medium, their velocities are higher than the speed of light in the medium and they polarize the corresponding molecules, resulting in the emission of Cherenkov photons with wavelength between 300 to 500 nm. This short lasting (5-20 ns) blue light is called Cherenkov light. It spreads with a cone opening angle $\cos\theta_c$ calculated from

$$\cos\theta_c = \frac{1}{\beta n} \tag{2.1}$$

where β is the ratio of particle velocity in medium and speed of light in vacuum and n is the refractive index that depends on the density of air. This angle is calculated as around 1.5° (Ong [20]) and the shower spreads over a large circular area with radius 120m on the ground if the spreading starts at 10km above the sea level (Mazin [15]).

The number of photons N emitted per unit track length z of a charged particle and per unit wavelength λ can be calculated by (Mazin [15]):

$$\frac{d^2N}{dz d\lambda} = 2\pi\alpha Z^2 \frac{\sin^2\theta_c}{\lambda^2} \tag{2.2}$$

where $\alpha = \frac{1}{137}$ is the fine structure constant and Z is the atomic number.

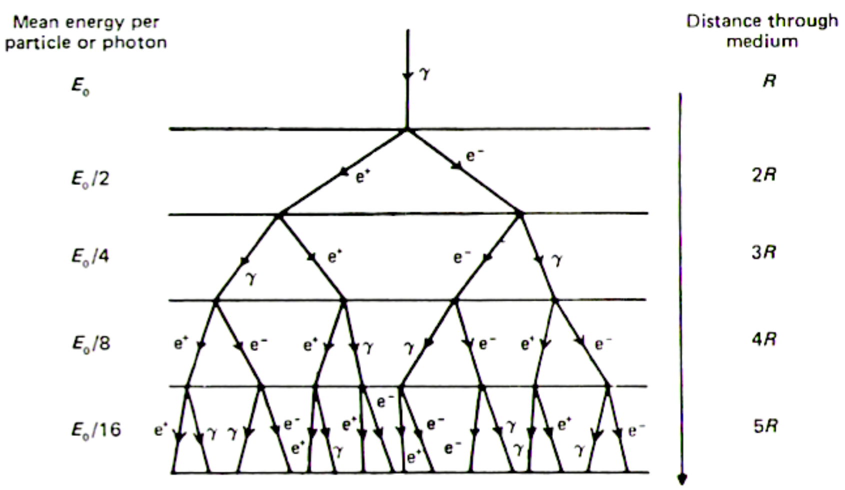

Fig. 2.1 A model for an electromagnetic shower. E_0 is the energy of the initial photon and R is the radiation length. (Longair [14])

Since the energy flux level drops rapidly and the photons spread over a large area on the ground, this gives faint signals for detection through a ground-based telescope. Thus the effective area for the detection has to be maximized by using a large array of wide-field telescopes which spreads over a grid of several square kilometers (Ambrogia et al. [2]). To capture this faint flash, a telescope with a large segmented mirror is required to reflect the Cherenkov light onto the photomultiplier tubes of the telescope camera, called the Cherenkov camera, which is designed to record Cherenkov flashes that only last for at most a few tens of nanoseconds. A shower will be captured by a few telescopes, the cascades appear as elliptical cones in the camera as shown in Fig. 2.2. By projecting the images of the same shower into one, the origin of the cascade can be identified by looking at the intersection point of these elliptical images from the major axis. One can then reconstruct the path and the energy of the initial gamma-rays and analyze them.

This technique for detecting the indirect gamma-rays is called the Imaging Atmospheric Cherenkov Telescopes (IACTs) technique. To have in-depth understanding of the gamma-ray sources, the next-generation ground-based gamma-ray observatory, Cherenkov Telescope Array (CTA), that have an order of magnitude more telescopes than the current IACT systems, including H.E.S.S., MAGIC and VERITAS, is under development. It will give a larger effective area and better angular resolution for the detection. The sensitivity will also be improved in the 100 GeV−10 TeV range (CTAConsortium [5]) as shown in the Fig. 2.3. With the help of the CTA, the current gamma-ray catalog can be extended by tenfold as indicated in Fig. 2.4.

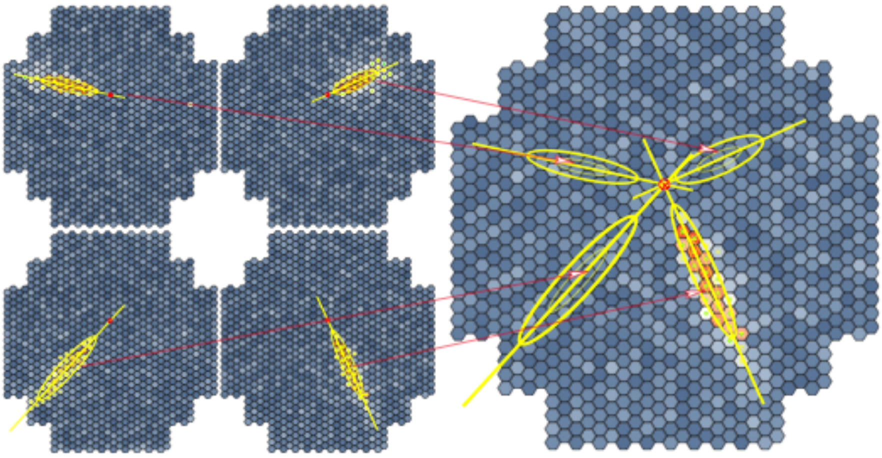

Fig. 2.2 Left: The images of a cascade taken by four different Cherenkov cameras. Right: The projection of the four images into one. The intersection of the major axes is the origin of the primary photon. (Völk and Bernlöhr [26])

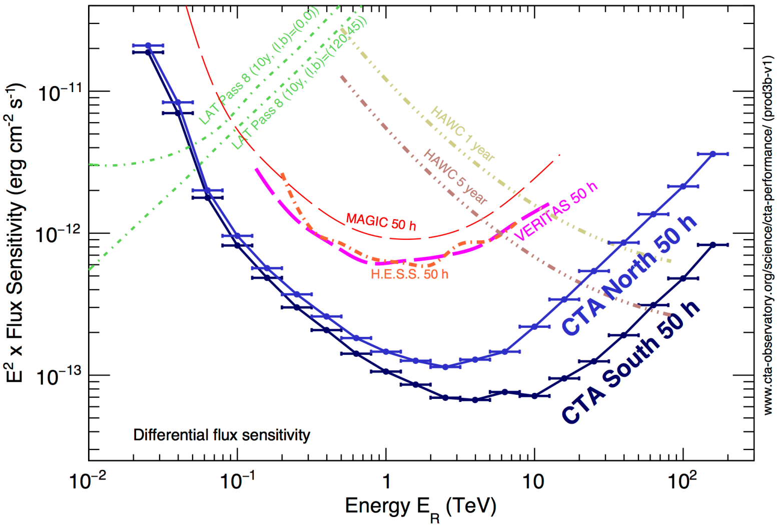

Fig. 2.3 The differential sensitivity for CTA compared to different gamma ray instruments like H.E.S.S. and MAGIC. (CTAConsortium [6])

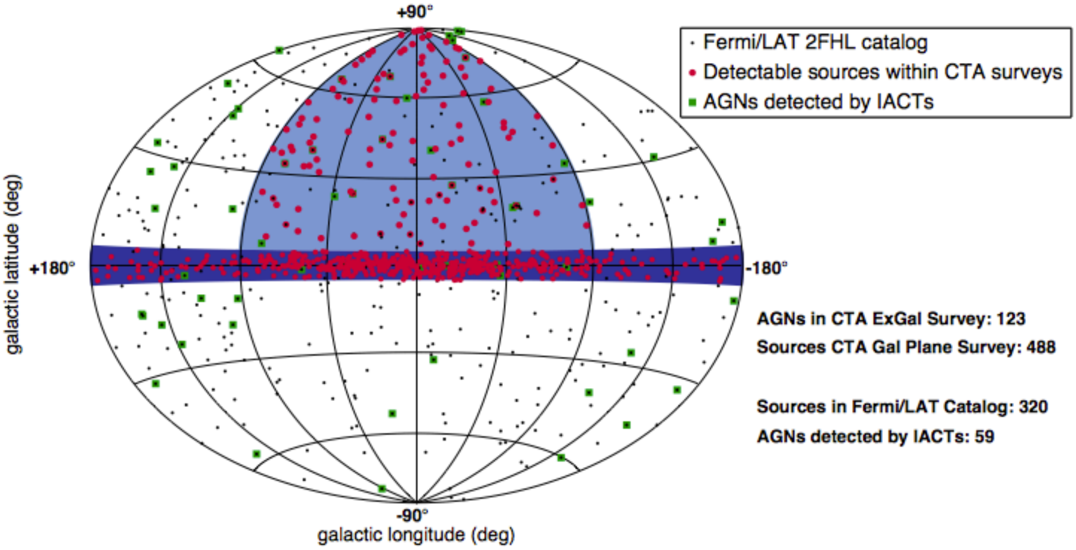

Fig. 2.4 The proposed extragalactic survey (light blue) and the Galactic Plane Survey (dark blue). Red points are the hypothetical sources to be detected by the CTA. Black dots are the Extragalactic and unidentified Fermi-LAT hard-spectrum sources. Green dots are the AGN that have been detected by the current IACTs. (CTAConsortium [6])

CTA consists of telescopes with three different sizes that are sensitive in different energy regimes. The Large-Sized Telescope (LST) targets at energy range 20 GeV−150 GeV, the Meidum-Sized Telescope (MST) targets at 150 GeV−5 TeV and the Small-Sized Telescope (SST) aims at 5 TeV−300 TeV (CTAWebsite [7]) as shown in Fig. 2.5 and Fig. 2.6. The arrays will provide full sky coverage by placing in the northern hemisphere, which focuses on the studies of Active Galactic Nuclei sources, and southern hemisphere, which enables a view onto the inner Galaxy (CTAConsortium [6]). The telescopes will be equipped with large mirrors and fast electronics to collect and read out the faint Cherenkov light flashes. The whole array will detect gamma rays with energies ranging from 20 GeV to 300 TeV, which foresees an excellent work on expanding the current catalog and search for the origin of cosmic rays.

This thesis is focused on the pointing solution of the MSTs. The MSTs will dominate sensitivity in the core energy range of the CTA as seen in Fig. 2.6. There are in total 40 MSTs planned for the CTA project, of which 25 will be located in the southern hemisphere and 15 in the northern hemisphere. To have a long lasting lifetime, they are made of steel to ensure high stiffness to support the optical structure under all elevation angles and to prevent tilting due to strong winds (Pühlhofer [22]). The optical design follows Modified Davies-Cotton, in which the reflector will have up to 90 hexagonal-shaped mirrors mounted

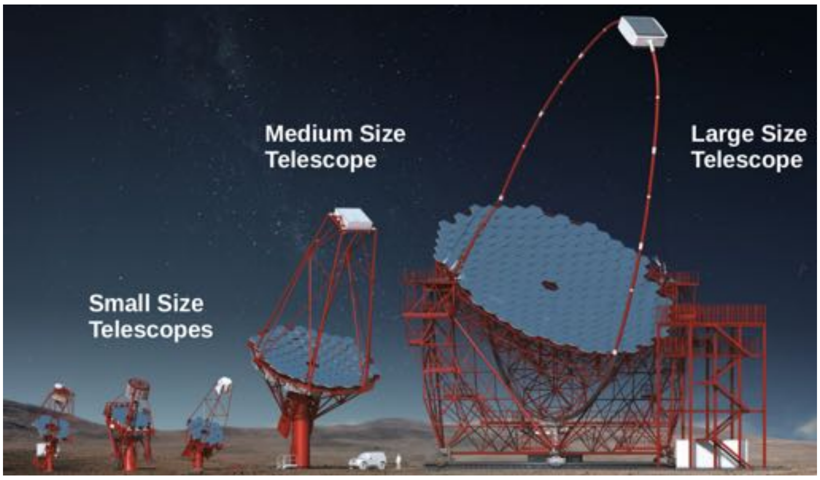

Fig. 2.5 Schematic view of three different sized telescopes optimized for three different energy ranges. (http://inspirehep.net/record/1600764/plots)

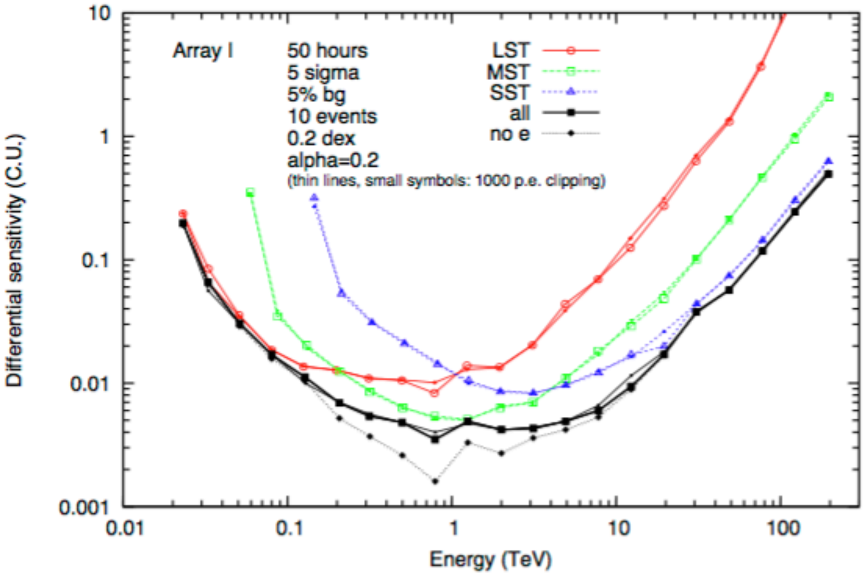

Fig. 2.6 The differential sensitivity of the LST, MST and SST. (Bernlöhr [3])

to the dish that align with an active mirror control (so-called actuators) assembly to create a uniform reflector (CTAWebsite [7]) as shown in Fig. 2.7. This reflector has 11.5 m diameter on a polar mount and provide an effective mirror area of 88 m^2 with a focal length of 16 m. Each telescope is equipped with an altitude-azimuthal mount, which allows rotations in both the altitude and azimuth direction in order to track gamma-ray sources in different directions. The telescopes are able to observe any astrophysical object with elevation larger than 24° (CTAWebsite [7]). The Cherenkov camera uses photomultiplier tubes (PMTs), and will cover about 8 degree field of view on the sky and requires a pointing precision to be smaller than 7 arcseconds (CTAWebsite [7]), enabling to determine gamma-ray sources rapidly.

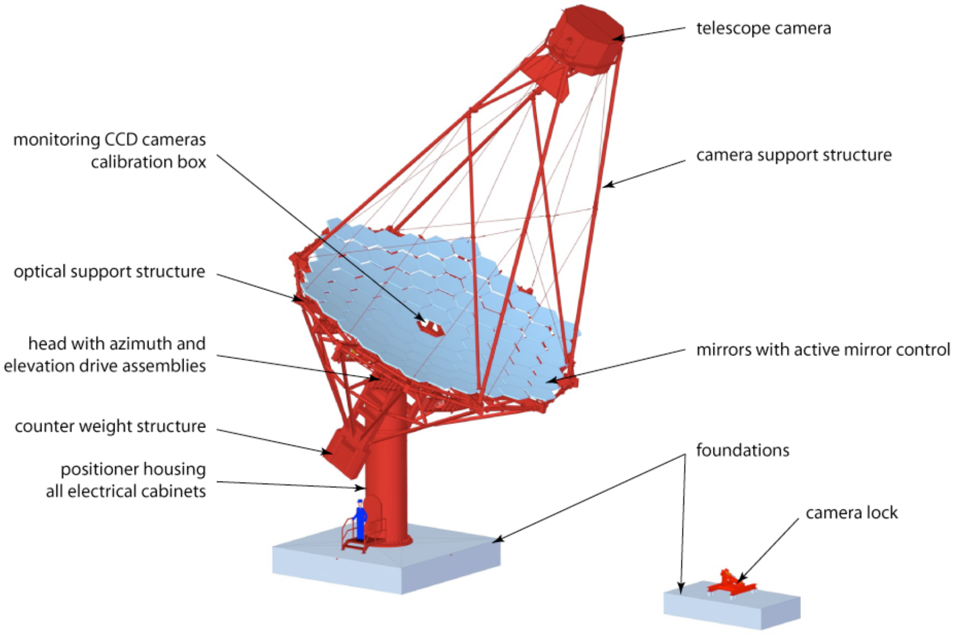

Fig. 2.7 A schematic illustration of main components of a MST. (https://portal.cta-observatory.org/Pages/MST.aspx)

Chapter 3

Pointing Calibration

CTA allows the reconstruction of the origin of the incoming gamma quantum with high sensitivity, relatively low energy threshold, good energy resolution and angular resolution compared to the current IACTs systems. To achieve a high resolution for the reconstruction, one must be able to relate a point captured by the Cherenkov camera in the camera focal plane to a position on the sky, thus the exact optical axis of the telescope has to be known and has to be close to the desired sky coordinates for online tracking. This is especially important for stereoscopic reconstruction because the pointing deviation is directly related to the deviations of the reconstructed shower direction with significant amplification factors (Pühlhofer et al. [23]). The pointing accuracy of the telescope should therefore be better than the desired reconstruction accuracy of the air shower. Also the pointing correction for the systematic and mechanical errors should be put in a model, which allows the interpolation of these errors and the calibration points, and ultimately give a precise origin of the sources (Panter and Puehlhofer [21]). For the MSTs, the pointing precision is aiming at < 7" and the maximal allowed final reconstructed systematic error on the localization of a point-like source is 3" (Gaug [8]).

There are numerous causes for telescope misalignment, thus images taken from the telescope camera require a correction of their orientation. The pointing calibration is therefore done by using bright stars on the night sky as references, which is called astrometry. In this section, different ways of pointing calibration will be discussed.

3.1 Mispointing of Telescopes

Though the telescope is equipped with an altitude-azimuthal mount and can be rotated for tracking, one cannot only rely on the axes position of the telescope for pointing since there are various causes for misalignments, including (Pühlhofer et al. [23], Gillessen [9]):

- shaft encoder (for controlling the altitude-azimuthal motor) non-linearities;
- zero-point offsets of the shaft encoders;
- misalignments of the azimuth axis and altitude axis;
- offset of the camera center with respect to the telescope optical axis;
- bending of telescope mount components;
- irreproducible errors, such as obstacles on the drive rails and wind loads.

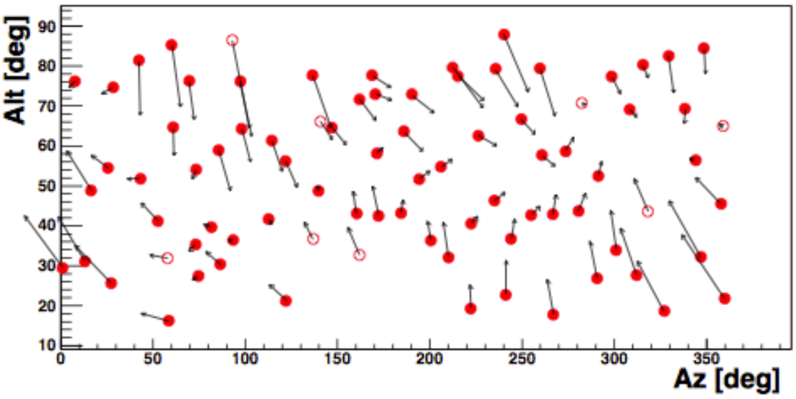

Fig. 3.1 Measured mispointing vector as a function of altitude and azimuth for H.E.S.S before correction. The raw pointing acurracy is 28". Arrows are 1500X enlarged. (Gillessen [9])

The reproducible errors can be predicted and corrected, while the irreproducible errors can only be corrected using the known positions of stars (Gillessen [9]). The Cherenkov camera however cannot be used to determine the correction as the point spread function of the dish is comparable or smaller than the size of the pixels of the array (Gillessen [9]), which means that the spot of stars is within one pixel on the image. The telescope has a PSF of order 360" whereas the pixel size is of order 300" to 864" and the required precision for locating a source for the CTA is 3" (Gaug [8], CTAWebsite [7]), therefore the precise location cannot be determined with the telescope alone. In the following, different ways of pointing calibration using bright stars on the night sky as references will be presented.

3.2 Calibration Method

3.2.1 Pointing Runs

Pointing Runs is the pointing calibration method used for the High-Energy-Gamma-Ray-Astronomy (HEGRA) system. The various types of detectors in the HEGRA IACT took data between 1987 to 2002. The point spread function of these telescopes is small compared to the pixel size. This means the image of a star cannot be localized better than the pixel size (Panter and Puehlhofer [21]) for pointing. Yet this indicates transits of stars from one pixel to another could be used (Gillessen [9]).

The pointing calibration is done by calibration measurement for the star in an image (Pühlhofer et al. [23]). A star with sufficient brightness is focused on the center of a photomultiplier camera. This image is then scanned across the central pixel by moving the azimuth motor while fixing the altitude motor, giving the distribution of current in the central pixel as a function of the distance between the expected star image and the pixel center as shown in Fig. 3.2 (Pühlhofer et al. [23]). The center of this distribution determines the center of the star in the image. The deviation of this point to the origin of the distribution is the deviation in telescope pointing.

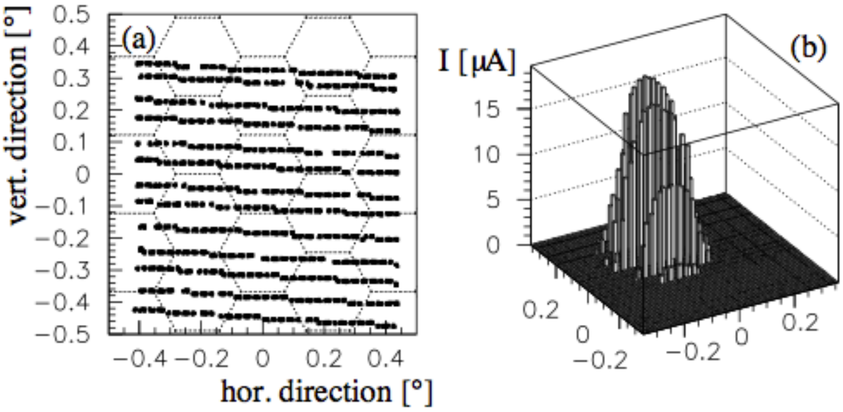

Fig. 3.2 An example of a pointing run, where a star is scanned across the central pixel by fixing the altitude motor. The scanlines appear slightly rotated in the camera since the star is moving. (a) Nominal star image positions in the camera. (b) Current in the central pixel as a function of the distance between the pixel center and the expected star image. The peak is not centered at 0, meaning there is a deviation in telescope pointing. (Pühlhofer et al. [23])

A typical scan takes 15 minutes and at least 30 pointing runs are needed for a new calibration, which take 8 to 10 hours calibration time (Pühlhofer et al. [23]). With this method, the pointing accuracy is better than 36" after the correction (Panter and Puehlhofer [21]).

3.2.2 Two-CCD Concept

The Two-CCD concept has been applied at the High Energy Stereoscopic System (H.E.S.S) experiment since 2012.

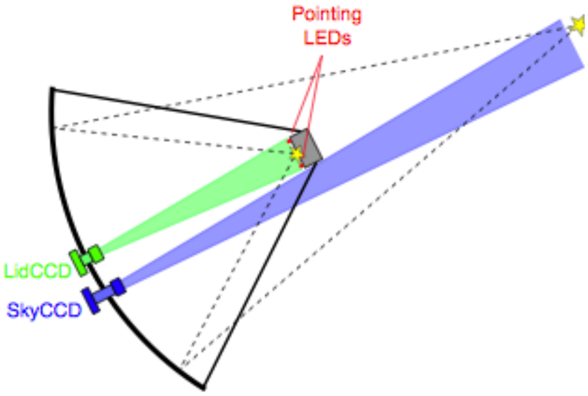

Fig. 3.3 Illustration of the Two-CCD camera method. (Herpich [11])

In this Two-CCD system, two CCD camera with different lenses are being mounted on the mirror dish as illustrated in Fig. 3.3. The first camera LidCCD has a 35 mm lens and gives a relatively small field of view that can only capture the Cherenkov camera (Oakes et al. [18]). It points along the optical axis of the Cherenkov camera and captures a reflected spot from a bright star on the closed lid of the Cherenkov camera. The position of this reflected spot can be measured with respect to the Pointing LEDs in the focal plane (Oakes et al. [18]) as shown in Fig.3.4. Thus the position of the Cherenkov camera can be derived and a complete pointing model can be derived. LidCCD can also be used to measure the reproducible error caused by the structural deformation of the optical support structure and telescope frame, which could improve the pointing model.

Notice that the LidCCD encounters the problem of spot deformation as illustrated in Fig.3.5, in which the position of LEDs deform in the image and create a problem on locating the center of the Cherenkov camera lid. The deformation is mainly related to the radial distance from center (deform from the center, the corners deform the most), the wavelength of source (red light deforms the most) and camera aperture (the higher the more deformation) (Molenaar [16]).

Since the LEDs are at the corner of the image and the deformation effects are cancelled out due to the radial symmetry, the calibration can still be done by finding the center of

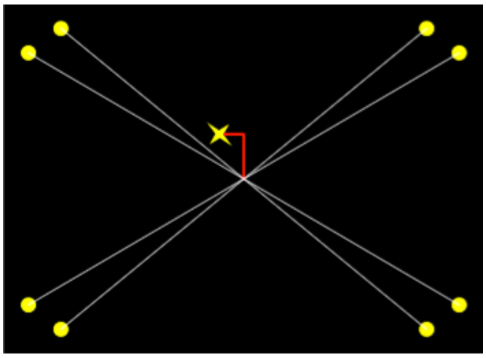

Fig. 3.4 An illustration of an image taken by the LidCCD camera. The center of the camera lid is determined from the positions of 8 LEDs (yellow spot) in image. Deviation of star positions in the image from this center gives the pointing errors. (Molenaar [16])

Fig. 3.5 Illustration of the spot deformation. The center spot is the standard appearance of a spot. (Molenaar [16])

gravity of LED spots and fit them to the known LED positions on the camera lid. From this transformation, the exact center of the Cherenkov camera shown in the image is known. The center position accuracy is within 3" for the H.E.S.S. telescope in Namibia (Molenaar [16]).

The second camera SkyCCD has an 85mm lens and gives a 4.26° × 3.21° field of view towards the sky image (Oakes et al. [18]). It serves as a guide telescope for the fine correction of the calibration. Images taken by the SkyCCD are analyzed and the observed stars are matched to indexed catalogs using a pattern match algorithm. This identifies the true pointing direction of the SkyCCD camera and determines the irreproducible error during the measurements, for example the wind drag. Through transforming the field of view between the SkyCCD and LidCCD, the pointing direction of the Cherenkov camera in the optical axis can be calculated from the SkyCCD images (Oakes et al. [18]).

The raw pointing accuracy for H.E.S.S is 28". After applying the model based on the LidCCD for the reproducible errors, the accuracy is 8". After the fine correction from the SkyCCD, the pointing accuracy is 2.5" (Gillessen [9]). This method gives high pointing accuracy and is less time consuming compared with the Pointing Runs used by HEGRA.

3.2.3 Single-CCD Concept

The Single-CCD concept is an new pointing calibration concept. This together with the two-CCD concept are currently undergo several tests on the MST prototype in Berlin (Adlershof). This method combines the SkyCCD and LidCCD, requiring only one CCD-camera with large field of view (20.77° × 15.58°) mounted on the mirror dish. With such a field of view, both the Cherenkov camera and its surrounding sky can be captured simultaneously. This Single-Pointing CCD allows determination of pointing direction and measurement of the structural deformation of the telescope structure at the same time.

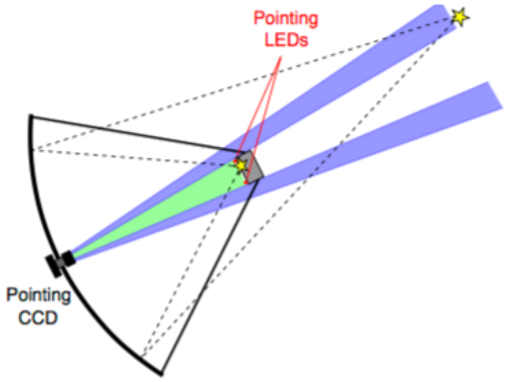

Fig. 3.6 Illustration of the Single-Pointing CCD method (Herpich [11])

Yet the deformation of stars at the edge of the image, the defocussing on both the Cherenkov camera (30 m) and the sky (∞) at the same time and the low resolution due to the large field of view remain the biggest inadequacies of this concept (Tiziani [25]). However the defocussing problem can be solved by focus the CCD-camera to a hyperfocal distance of 60 m, double the distance to the Cherenkov camera (Tiziani [25]). Also the cost saving and the reduction of calibration complexity are still powerful reasons to implement this method for the 40 MSTs.

The pointing ability by utilizing the Single-CCD is further studied in Chapter 6 using simulations and at the end the real images. Notice this thesis will only explore the pointing ability of the Single-CCD through analyzing sky images surrounding the closed lid of the Cherenkov camera.

Chapter 4

CCD-Camera Calibration

The pointing direction of the telescope is determined by analyzing sky images captured by the equipped Charge-Coupled-Device (CCD) camera. The camera is using a CCD imaging system, in which images are captured on the CCD-chip that is made up of thin silicon wafer. Since the calibration involves extracting the star positions in the sky images, it is important to assess the expansion and contraction of the CCD-chip at different chip temperatures which may cause optical deformations and image aberrations.

In this chapter, the working principle of the CCD-camera will be explained. A CCD-chip expansion test is performed in order to evaluate how much the position of points in an image will shift due to expansion/contraction of the CCD-chip. The CCD-camera used in this test is of the type Apogee Aspen CG8050 with a thermoelectric cooler that can control the chip temperature.

4.1 Working Principle of the CCD-Chip

The CCD is a major technology for digital imaging that is popularly used in the astronomical field. It is a device consisting of a thin silicon wafer divided into millions of tiny light sensitive squares, each square in the pixel grid corresponds to an individual pixel in the final image. When photons hit the silicon surface, they turn into electrical charges through the photoelectric effect and are attracted to the nearby pixel squares. Once the chip has been exposed to an image, charges move between the squares until they reach the charge amplifier. The output voltage is directly proportional to the number of photons that penetrate the tiny squares. This output voltage, which represents the brightness of the image at the corresponding pixel location, is then convert to a digital signal (Griffith [10]).

Materials will undergo expansion and contraction regarding to different temperatures. Consider the camera has taken two images, the first one is at the initial temperature and

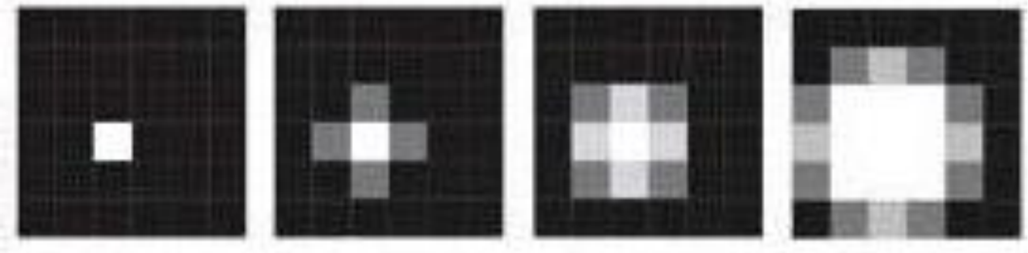

Fig. 4.1 An illustration of CCD-chip expansion effect. The CCD-chip is contracted with respect to the center of white square, shown from left to right, leading a decrease in field of view. The corners of the white square shifted to another pixel position. (http://www.andor.com/learning-academy/ccd-spatial-resolution-understanding-spatial-resolution)

the second one is at a lower temperature. When the temperature decreases, the CCD-chip contracts and the field of view of the camera will also decrease as shown in Fig. 4.1. Since the number of pixel squares is fixed, it is expected that the position of points in the first image will be shifted to another position in the second image. In other words, the positions of points at the boundary in the first image will not be seen in the second image. The degree of pixel position shift in an image is proportional to the expansion rate for the chip.

4.2 CCD-Chip Expansion Test

The CCD-camera used in this test is of the type Apogee Aspen CG8050. The camera is connected to an external 12 V power supply and has a 2 MHz Ethernet interface with a built-in web server. Communication with the camera is done by using the software **libApogee** on a scientific Linux virtual machine (Tiziani [25]). The camera objective is of the type Nikon AF NIKKOR, where the fixed focal length is 50 mm and its aperture allows a focal ratio between 1.8 and 22. The CCD-camera is put in an aluminium housing to prevent extra movement of the camera during the image taking process.

The camera chip is made by material that contains silicon. It has an array size of 3296×2472 in pixels and each pixel has a size of 5.5×5.5 μm. A more detailed CCD specifications can be found in Appendix A. The camera consists of a programmable thermoelectric cooler to vary the CCD-chip temperature. The heat sink and fans of this cooler have been removed to prevent dust entering the camera. This gives a maximum cooling for the chip of about 50 °C below ambient temperature. Both the exposure time and chip temperature can be controlled by the software **libApogee**. The analysis is based on the assumption that the chip is completely flat and has the standard pixel size of 5.5×5.5 μm at chip temperature 26 °C and no expansion at this temperature.

4.2.1 Set Up and Procedures

The experiment is conducted at room temperature (about 25 °C). To examine the chip expansion effect, a pattern of chessboard is placed in front of the CCD-camera as shown in Fig. 4.2. The distance between the camera and the screen is 50 cm. The aperture of the lens is set manually until the images taken are sharp enough to examine the pixel detail of the corners.

The expansion effect is evaluated by looking at how the corners of the chessboard shift in the same images taken by the CCD-camera at different chip temperatures. Since the uneven light distribution on the image will create great corner tracking errors and the paper sheet will move due to wind and humidity, this experiment was conducted in a dark room with the camera facing the chessboard image on the screen of a laptop instead.

Three sets of data have been taken, the sets are with different camera exposure times of 5 s, 3 s and 2.5 s. Each set consists of 6 images taken at chip temperature from 26 °C to -25 °C with 10°C step size.

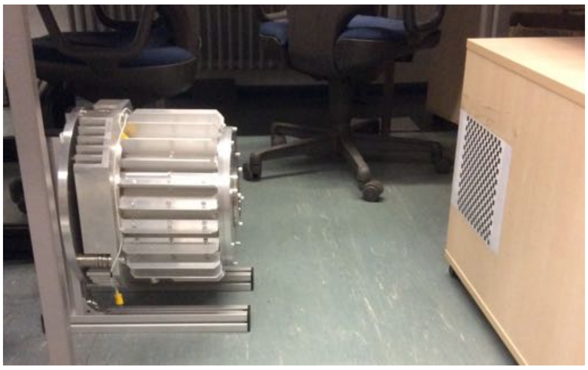

Fig. 4.2 The experimental set up for the chip expansion test. The chessboard sheet is later replaced by the screen of a laptop and the measurement is conducted in the dark.

Since the expansion of the CCD-chip is expected to be in the order of magnitude of nanometers, the corner position should be extracted with high precision. This is done by using several OpenCV libraries. The corner detection is done with the library based on the Shi-Tomasi Corner Detection method presented by J. Shi and C. Tomasi in 1994. This tracking method is the successor of the famous Harris Corner Detector and outputs the corner positions with better accuracy. After locating the possible corners, their positions are then refined and calculated with subpixel precision.

4.2.2 Result

The graph in Fig. 4.3 shows how the pixel positions of all square corners shift in an image taken at chip temperature -25 °C with respect to the image taken at chip temperature 26 °C. By assuming the chip is glued at a single point in the camera and all shifts relative to that fixed point, this glued point is determined using least square method to be at (2340.05, 2059.86).

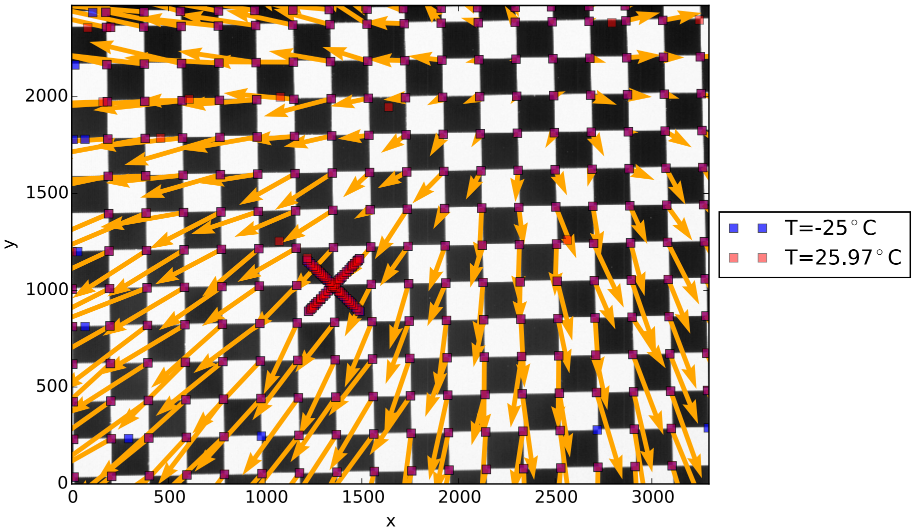

Fig. 4.3 The positions of corners in the image shift at chip temperature -25 °C with respect to the positions of corners at chip temperature 26 °C. The orange arrows indicate the pixel shift from 26 °C to -25 °C, they are 329.6X enlarged. The shift is relative to the glued point of the chip at (2340.05, 2059.86). The big red cross at (1400, 1000) is part of the chessboard image and is mis-extracted as corners by the OpenCV.

To see the trend of pixel shift at different temperatures, the corner at the bottom left is being picked for the tracking since it is furthest away from the fixed point and thus gives a smaller error relative to the glued center. The data can be fitted by a linear function as shown in Fig. 4.4, which indicates that the chip expands linearly.

The data set with the exposure time 5 s fluctuates more than the other two sets. The possible reason is that the observed chip temperature stability is ±0.5 °C. Thus the larger the exposure time, the greater the temperature fluctuates which blurs the corner position through optical deformation. Yet more corners can be extracted at high exposure times than at low exposure times, this gives a better accuracy on deriving the glued point of the chip.

The expansion factor β is defined as

$$\beta = \frac{d_{T=26^\circ C} - d_{gluedpoint}}{d_T - d_{gluedpoint}} \tag{4.1}$$

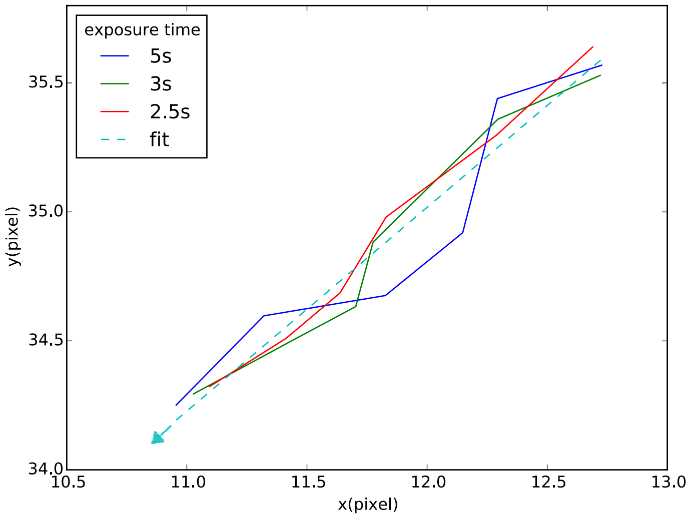

Fig. 4.4 The trend of pixel shift of at the bottom left corner in x- and y-direction at different temperatures. The arrow indicates the data taken at chip temperature from 26 °C to -25 °C.

where $d_{gluedpoint}$ is the position of glued point, $d_{T=26°C}$ is the position of a corner at T=26°C, d_T is the position of the same point at any given temperature.

The expansion factor β decreases when the chip temperature decreases, as this term is directly related to the expansion rate of the chip itself. The expansion factor in which the chip itself expands is fitted to the temperature T[°C] in Fig.4.5 by a linear function:

$$\beta_x = (1.38 \times 10^{-5}[°C^{-1}]T + 0.9996277) \tag{4.2}$$

$$\beta_y = (1.29 \times 10^{-5}[°C^{-1}]T + 0.9996624) \tag{4.3}$$

where the sum of the squares of the fit errors for β_x is 2.5×10^{-8} and for β_y is 3.1×10^{-8}. The discrepancy between the two expansion factors is due to the chip might not be glued at a single point. The corresponding pixel scale s in arcsecond per pixel can be calculated using the function:

$$\begin{aligned} s &= \frac{pixelsize}{focallengthscope} \\ &= \frac{5.5\times\beta}{50} \times 206.3[arcsecs/pixel] \\ &= 22.693 \times \beta[acrsecs/pixel] \end{aligned} \tag{4.4}$$

where the normalization constant $206.3[\frac{arcsec\times mm}{\mu m}]$ is from $\frac{360°}{2\pi}\frac{3600arcsec}{1°}\frac{1mm}{1000\mu m}$.

As shown in Fig.4.5, the pixel scale s with respect to the glued point decreases when the chip temperature decreases, which means the field of view of the camera is smaller at low temperatures. The pixel scale difference Δs_x is 0.01597"/pixel and Δs_y is 0.01493"/pixel if

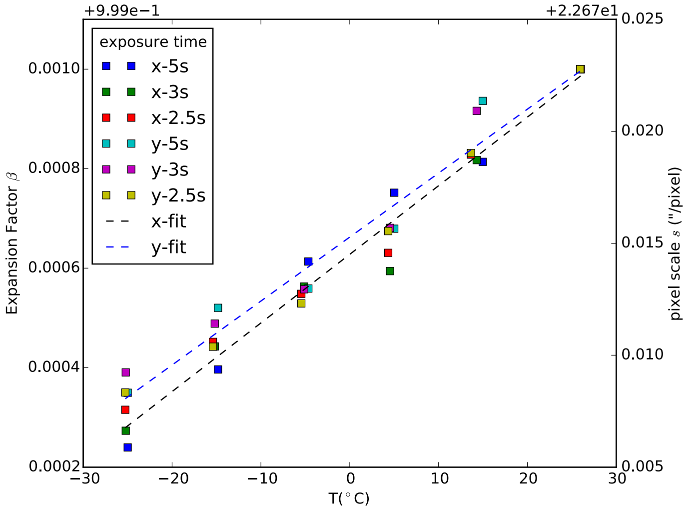

Fig. 4.5 The trend of expansion factor β and pixel scale s of the bottom left corner in x- and y-directions at chip temperature ranging from 26 °C to -25 °C. The corresponding fits in each directions are indicated in dashed lines.

the temperature decreases by 51 °C; Δs_x is 0.00157"/pixel and Δs_y is 0.00146"/pixel if the temperature difference is 5 °C.

The image center is at pixel position (1648,1236) where the optical axis of the camera center is located. When the chip contracts, this point moves further away from the glued point of the chip. This point will shift for $\Delta s \times (gluedpoint - imagecenter_{T=26°C})$ from its initial position. If the temperature difference is 5 °C, this will induce a pointing inaccuracy of 1.6" at the image center. Since the goal for the pointing accuracy is within 7" at the optical axis, it is crucial to keep the chip temperature constant to avoid any extra inaccuracy.

4.2.3 Remark

Notice when the chip temperature is at -25 °C, the expansion factor β_x is 0.9992827 and this corresponds to a decrease of (1-0.9992827)×5.5[μm] = 3.95 nm per pixel. For the case of pure silicon, the thermal coefficient α is determined empirically as (Okada and Tokumaru [19]):

$$\alpha(t) = (3.725(1 - \exp[-5.88 \times 10^{-3}(t - 124)]) + 5.548 \times 10^{-4} t) \times 10^{-6} [K^{-1}] \qquad (4.5)$$

where $\alpha(t) = \frac{1}{L}\frac{dL}{dt}$, L is the pixel size and t is the absolute temperature. This corresponds to a decrease of 0.65nm per pixels when the chip temperature is at -25 °C. This means the CCD-chip contracts 6 times more than pure silicon. Also it is expected that the expansion factor is isotropic, but the measured expansion factors in x- and y-direction are different as seen in equation 4.2 and 4.3.

The possible reasons for this huge discrepancy is that the CCD-chip is not made by pure silicon and it contains certain materials that are physically very sensitive to the temperature. The CCD-chip may also not be firmly glued at a single point such that the chip moves a bit each time when an image is being captured. Also one cannot ensure the surface of the chip is completely flat, this may give an extra optical deformation and image aberration.

Furthermore though the Shi-Tomasi Corner Detection method gives a better accuracy on the corner extraction, it is not supposed to track the corners with very high precision and in subpixel way. Further investigation using other software for the comparison is encouraged but it is beyond the scope of this thesis.

4.3 Summary

In this chapter we examined the chip expansion effect and determined the expansion factor at different chip temperatures from 26 °C to -25 °C. It gives an inaccuracy of 1.6" at the optical axis of the camera when the chip temperature changes for only 5 °C. To ensure the pointing accuracy within 7" and the fact that the chip may not be glued at the same point in every CCD-camera, which is hard for the calibration, the chip should be set at a fixed temperature such that the physical state of the chip stays constant throughout the working time of the MST without any expansion.

The extreme ambient working temperature for the MST is from -10 °C to 30 °C. It will be a challenge to determine a suitable chip temperature since the temperature difference is large and the CCD-camera will be put into an aluminum housing for safety, which will then affect the cooling efficiency of the camera. The optimization of the chip temperature together with testing on the housing will be performed in the next chapter.

Chapter 5

Housing Characterization

To protect the camera from any physical damages in the harsh environment at the CTA sites (La Palma and Paranal), it will be put into an aluminum housing for safety. In Chapter 4, the CCD-chip expansion effect was investigated and the necessity to maintain a stable chip temperature T_{chip} was shown in order to keep the pointing accuracy below 7". In this chapter, T_{chip} of the CCD-camera will be optimized to the CTA requirement for stable operations at the survival ambient temperature of -10 °C to 30 °C (CTAWebsite [7], the required ambient temperature is -5 °C to 25 °C). Since the heat produced by the camera is trapped inside the housing, the temperature inside the housing have to stay within the operating temperature range for the CCD-camera at the same time, which is -25 °C to 40 °C.

The first housing prototype was designed and several adjustments have been made since then (see Hofmann [12], Tiziani [25]). In the below sections, the housing design will be updated. A new glass heater design of the housing will be presented and the dew phenomenon will be explored. The climate chamber and outdoor measurement on the housing will be made. At the end, the outdoor performance of the housing on chip temperature stability at La Palma will be shown.

5.1 Hardware

5.1.1 Housing Design

The housing is made of aluminum with a total weight including the CCD-camera of about 30 kg. The schematics drawings of the housing are shown in Fig.5.1. The diameter of the housing is 280 mm and the length of its cylindrical body is 200 mm, where the CCD-camera is fitted in. The thickness of the wall is 10 mm. The access of the power supply, Ethernet and USB interface for the camera can be done via the external connector under the housing. A

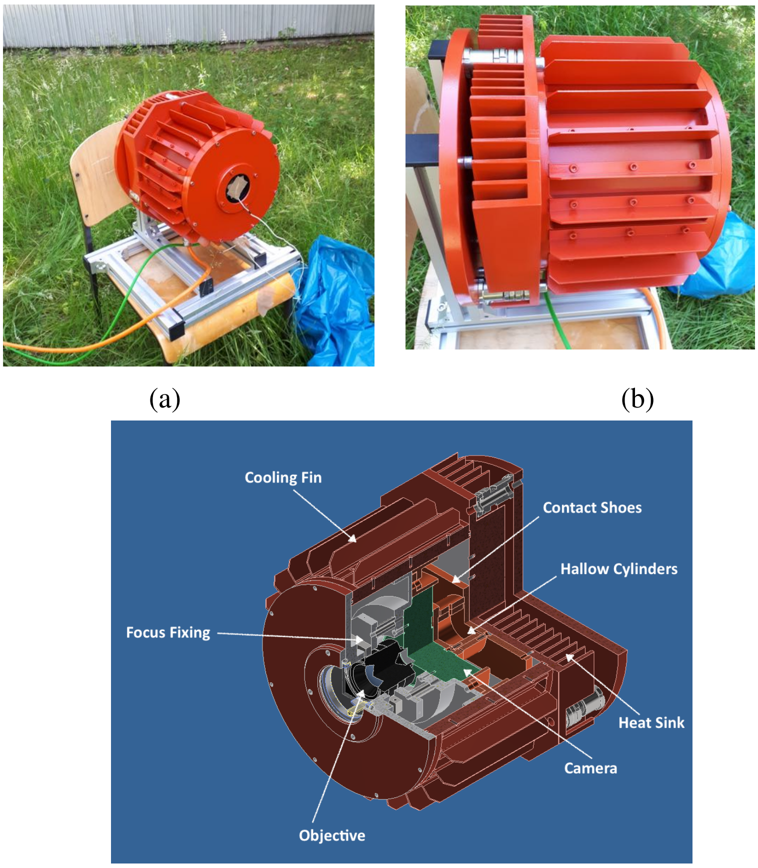

(a) (b)

(c)

Fig. 5.1 (a): The front view of the housing, where a glass covers the opening window. (b): The side view of the housing, heat sink is at the back of the housing. (c): Inside the housing where the camera is placed in (graphic from Johannes Depner).

window with the size of the camera objective is at the front plate of the housing, such that the camera is able to take sky images through the window. This window is covered by an anti-reflective coated glass.

Since the heat sink and fans are removed from the CCD-camera to avoid dusts entering the camera, the cooling of the camera is done by using two interlocking cooper hollow cylinders. One cylinder is attached to the warm side of the Peltier element of the camera and another cylinder is attached to the back plate of the housing, thus heat can transfer from the camera to the back of the housing (Tiziani [25]). A heat sink is connected to the back of the housing to facilitate heat loss through the thermal convection. There are also cooling fins attached on the cylindrical surface of the housing to increase the heat loss efficiency. Though black is the best color for cooling, it will heat up too much in the sunlight. Therefore the housing is painted in red since this color is a good compromise between efficient cooling as well as not absorb too much heat under the sunlight. These ensure no overheating inside the housing such that the camera can operate well. Both measurement without and with red painting are described in this chapter.

5.1.2 Dew Phenomenon and Glass Heater Design

It was observed in an older version of the housing that water condensation occurred on the inner and outer glass surface. This is due to the fact that when the air is being cooled down to a certain temperature, excess humidity starts condensing on cold surfaces. This temperature where the water condensation takes place is called the dew point. When this temperature is below the freezing point of water, frost will occur. Every air temperature with different humidity has its corresponding dew point. Fig. 5.2 shows an overall view of air temperature versus the dew pointing based on the following two equations:

$$P_a(T) = \frac{RH}{100} a \exp(\frac{bT}{c+T}) \tag{5.1}$$

$$T_{dp} = \frac{c \ln \frac{P_a(T)}{a}}{b - \ln \frac{P_a(T)}{a}} \tag{5.2}$$

where RH is the relative humidity, a=6.112, b=17.67 and c=243.5 (Bolton [4]). These parameters are derived from David Bolton in 1980 and give an accuracy of 0.1 % for air temperature -30 °C $\leqslant T \leqslant$ 35 °C.

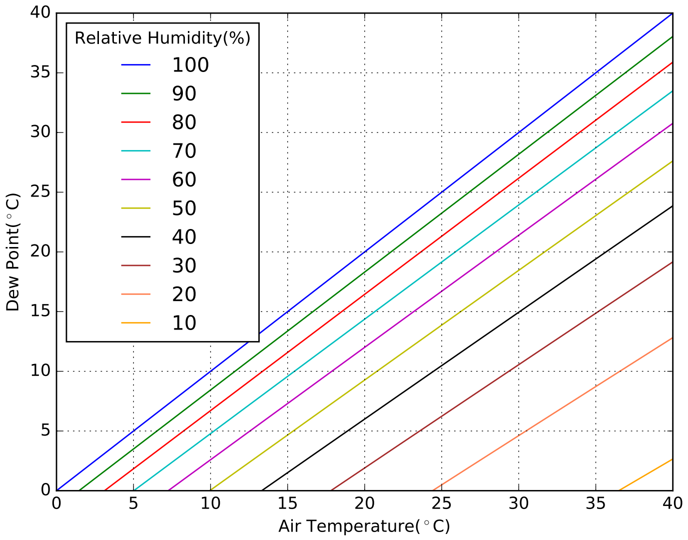

Fig. 5.2 The corresponding dew point of air with different temperatures at different relative humidities.

Notice that the dew point is always lower than the air temperature. If a surface has a temperature higher than the dew point of the surrounding air, the air cannot cool down to the dew point at the surfaces and thus no water condensation will occur on the surface.

Both dew and frost formation on the glass will seriously affect the image taking of the CCD-camera and thus affect the pointing measurements of the telescope. To get rid of mist and frost, the glass heater is needed to heat up the glass surface. There are two glass heater designs as shown in Fig.5.3 for warming the glass in order to prevent the water condensation on the glass surfaces. The original design was to attach a heating cotton on the front plate. However it has low efficiency on warming the inner glass and costs more. The new design is to enclose a heating cylinder around the inner glass, where a tiny sensor touches the inner glass. The heater warms the glass directly when the glass temperature is below the set temperature of the heater. This design indeed gives the best efficiency towards warming the glass and costs less. Thus the latter design is being used throughout the measurements in this chapter.

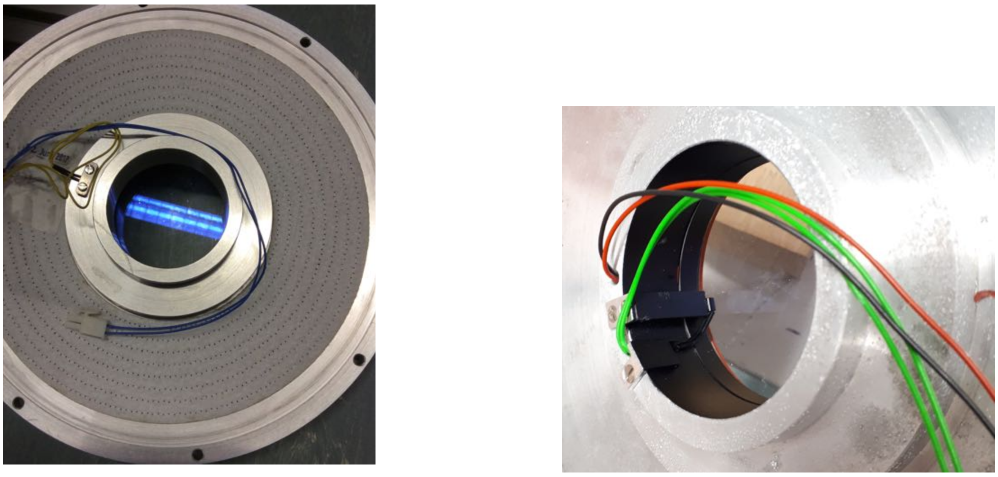

(a) (b)

Fig. 5.3 The old (a) and new (b) glass heater design for warming the glass. All the measurements below are done using the new heater design.

5.2 Chamber Measurements

The CTA requirement for the working ambient temperature range for MSTs in La Palma is -5 °C < $T_{ambient}$ < 25 °C (CTAWebsite [7]), while the extreme ambient temperature range is of -10 °C < $T_{ambient}$ < 30 °C. The survival temperature for the CCD-camera is -25 °C to 40 °C, in which the temperature inside the housing should not exceed this range.

(a) (b)

Fig. 5.4 The temperature measurement of the housing inside the temperature chamber.

To test the housing and the stability of the chip temperature, the measurement is firstly carried out inside a temperature chamber as shown in Fig. 5.4 where one can set the ambient temperature. Temperature sensors are attached to the inner and the outer surface of the front window and positioned to the air inside the housing as well as in the air inside the chamber for reference, they can measure temperature ranging from -20 °C to 250 °C. The recorded temperature can be read out from a data logger of the type VOLTCRAFT PL-125-T2USB VS. The chip temperature can be set and read out via the camera electronics. Notice that wind is circulating inside the chamber in order to maintain a stable ambient temperature. This will increase the cooling efficiency for the housing and thus it is expected that the air temperature inside the housing would be lower than in an outdoor measurement.

5.2.1 Glass Heater Switch On Point

The glass heater for warming the glass in order to avoid water condensation is built by the electronic workshop of the FAU ECAP. It will switch on when the temperature sensor detects the temperature at around 20 ° to 30 °C, yet the exact switch on point is unknown. The setting of the glass heater also changes a bit after the housing is painted in red for the safety reason, such that it will not burn the lens of the camera. Therefore in this section, the glass heater switch on point will be investigated for housing before and after painted.

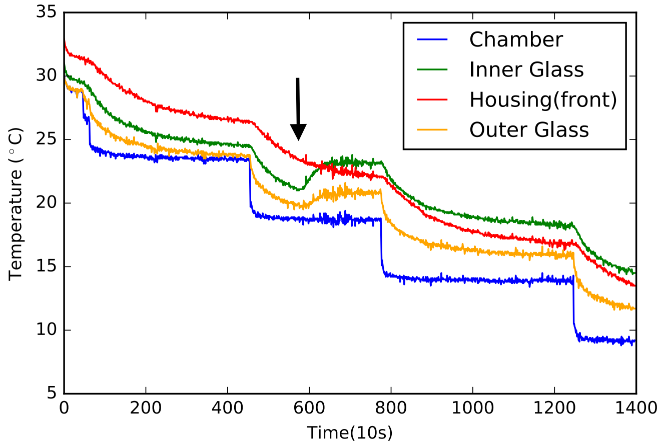

Fig. 5.5 Temperature of inner glass $T_{innerglass}$, outer glass $T_{outerglass}$ and the air inside the housing $T_{housing}$ correspond to the decreasing chamber temperature $T_{ambient}$. The black arrow is the point where the glass heater switches on. (Housing without red painting)

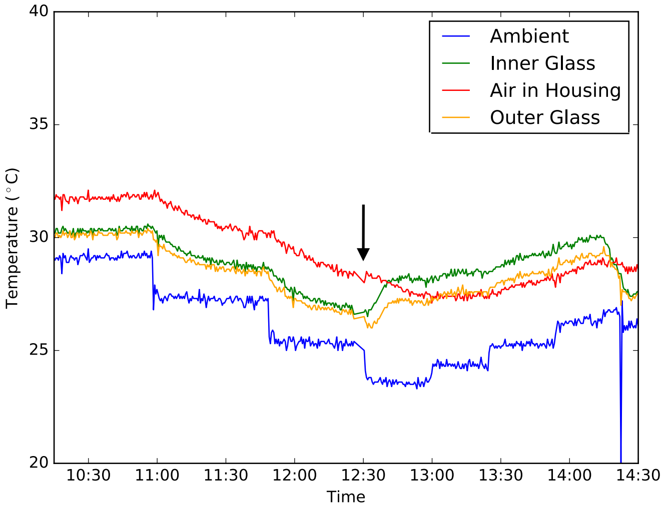

Fig. 5.6 Temperature of inner glass $T_{innerglass}$, outer glass $T_{outerglass}$ and the air inside the housing $T_{housing}$ correspond to the decreasing chamber temperature $T_{ambient}$. The black arrow is the point where the glass heater switches on. The sharp peak at time near 14:30 is where the chamber door is being opened. (Housing with red painting)

Housing without red painting

The chip temperature is set to -23 ° in this measurement and the chamber temperature is set to decrease step-by-step. From Fig. 5.5 one sees that the glass heater starts to work when the temperature inside the housing reaches around 24 °C whereas the inner glass temperature is around 21 °C. Due to the heating, both inner and outer glass temperatures increase to values greater than the temperature inside the housing and the chamber temperature respectively when the ambient temperature is set further down.

Housing with red painting

The chip temperature is set to -23 °C in this measurement and the chamber temperature is set to decrease step-by-step. From Fig. 5.6 one sees that the glass heater starts to work when the temperature inside the housing reaches around 28 °C whereas the inner glass temperature is around 27 °C. Both the inner and outer glass temperatures increase to values greater than the temperature inside the housing and chamber temperature respectively at this point.

5.2.2 Optimization of the Chip Temperature

The chip temperature cannot be set arbitrarily since there are maximum and minimum cooling power limit at each corresponding ambient temperatures. To determine a temperature where the chip can stay stable throughout the required and working temperature of CTA, the chamber temperature is set to -5 °C and -10 °C to explore the minimum cooling power that is needed; set to 25 °C and 30 °C to explore the maximum cooling power. Notice the optimization at the ambient temperature -5 °C, 25 °C and 30 °C for the red housing cannot be done within the scope of this thesis. However it is expected that the optimal chip temperature at high ambient temperature of 30 °C are similar for both versions of the housing since the heater will not be switched on yet at that point.

Housing without red painting

When the chamber temperature is at -5 °C, the chip temperature drops to -18.2 °C even if a higher temperature value is set to the chip as shown in Fig. 5.7 (a). When the chamber temperature is at -10 °C, the chip temperature drops to -23.2 °C even a higher temperature value is set to the chip as shown in Fig. 5.7 (b).

To explore the lowest possible chip temperature at the high ambient working temperature, the chamber temperature is further set to 25 °C and 30 °C. As shown in Fig.5.8, the chip was initially set at a higher temperature that the chip can reach and then set to a lower temperature. The chip can only be cooled down to a certain point. The chip temperature stays at that point and is unable to reach the set temperature. The lowest possible chip temperature is about -27.5 °C and -23.5 °C when the ambient temperature is at 25 °C and 30 °C respectively.

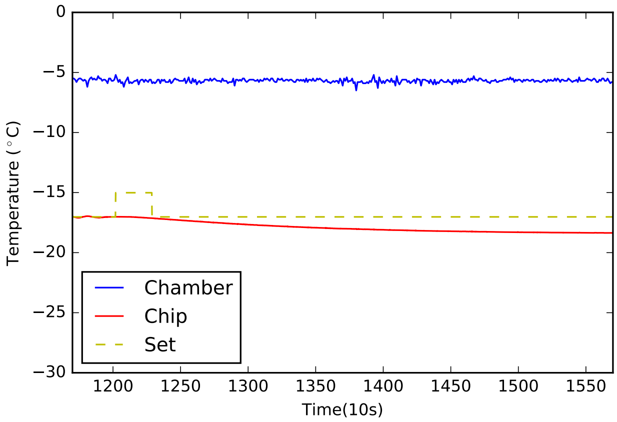

(a)

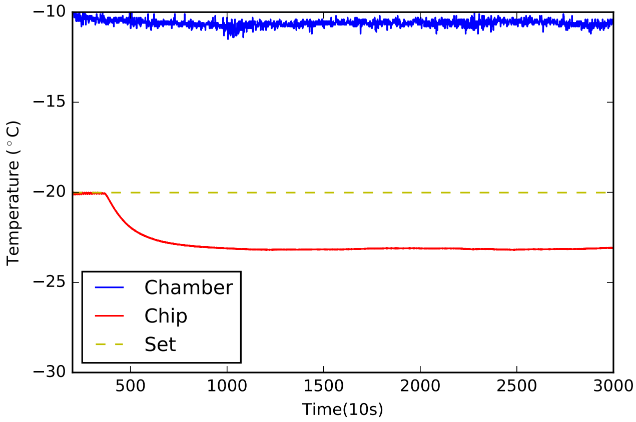

(b)

Fig. 5.7 Optimization of the chip temperature at the ambient temperature of -5 °C(a) and -10 °C(b). The blue line is the chamber temperature, the brown dashed line is the set temperature for the chip and the red line is the measured chip temperature. (Housing without red painting)

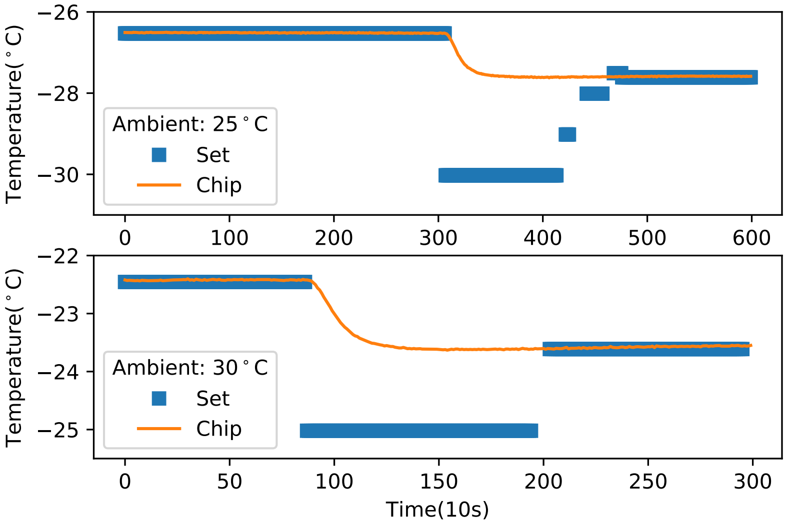

Fig. 5.8 Optimization of chip temperature at an ambient temperature of 25 °C (top) and 30 °C (bottom). The blue squares are the set temperature for the chip and the orange line is the measured chip temperature. (Housing without red painting)

Housing with red painting

When the chamber temperature is at -10 °C, the chip temperature drops to -22.6 °C even though the chip is set to a higher temperature as shown in Fig. 5.9.

The summary of the optimization test can be seen in Table 5.1. In short conclusion, it is observed that at low ambient temperature, the chip temperature will drop to a certain temperature even though a higher chip temperature is being set. For the housing without the red painting, T_{chip} drops to -18.2 °C when $T_{ambient}$ is at -5 °C, and T_{chip} drops to -23.2 °C when $T_{ambient}$ is at -10 °C. For the housing with the red painting, T_{chip} drops to -22.6 °C when $T_{ambient}$ is at -10 °C. The drop of the chip temperature at low ambient temperature is mainly because the heat produced by the camera during the operation is not enough to overcome the surrounding cold air, thus it decreases to the point where the heat loss and gain are in equilibrium. For the housing without the red painting, the lowest possible chip temperature is about -27.5 °C and -23.5 °C when the ambient temperature is at 25 °C and 30 °C respectively. The chip temperature cannot go further down because the surrounding air is too hot for the cooler to cool down the chip.

For $T_{ambient}$ at -10 °, the chip temperature is 0.6 °C higher in the red housing. This shows that either the red painting can prevent heat loss from the camera or the higher switch on point of the glass heater accumulates more heat inside the housing.

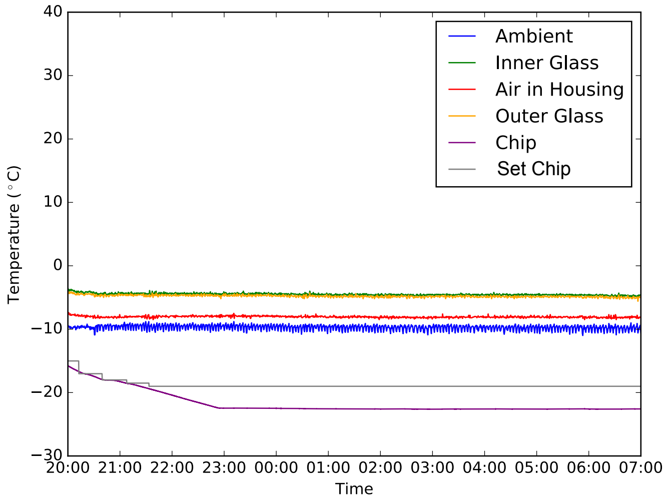

Fig. 5.9 Optimization of chip temperature at the ambient temperature of -10°C. The blue line is the chamber temperature, the gray line is the set temperature for the chip and the purple line is the measured chip temperature. (Housing with red painting)

Table 5.1 Summary on optimization of the chip temperature

$T_{ambient}$	Optimal T_{chip}	
	Housing without red painting	Housing with red painting
-10 °C	$\leq$-23.2 °C	$\leq$-22.6 °C
-5 °C	$\leq$-18.2 °C	/
25 °C	$\geq$-27.5 °C	/
30 °C	$\geq$-23.5 °C	/

By considering the high and low ambient temperature measurement results, the chip temperature at -23.2 °C for the housing without red painting and -22.6 °C for the housing with red painting is chosen to perform the stability test in the next section.

5.2.3 Stability of the Chip Temperature

According to the CTA requirement, the temperature of the chamber will be set from -10 °C to 30 °C to test the stability of the chip temperature in the extreme working temperature range of CTA.

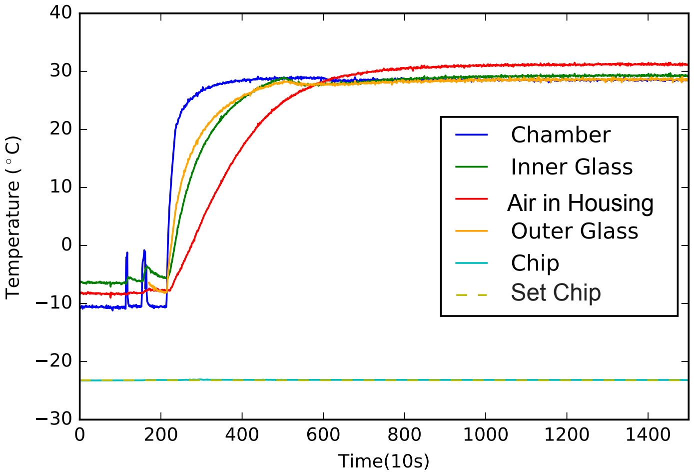

Fig. 5.10 Stability of the optimized chip temperature (-23.2 °C) at extreme working environment (-10 °C < $T_{ambient}$ < 30 °C) in the temperature chamber. The glass heater is switched off when the inner glass temperature is at 21 °C, therefore the air in the housing has a higher temperature than the glass when $T_{ambient}$=30 °C. (Housing without red painting)

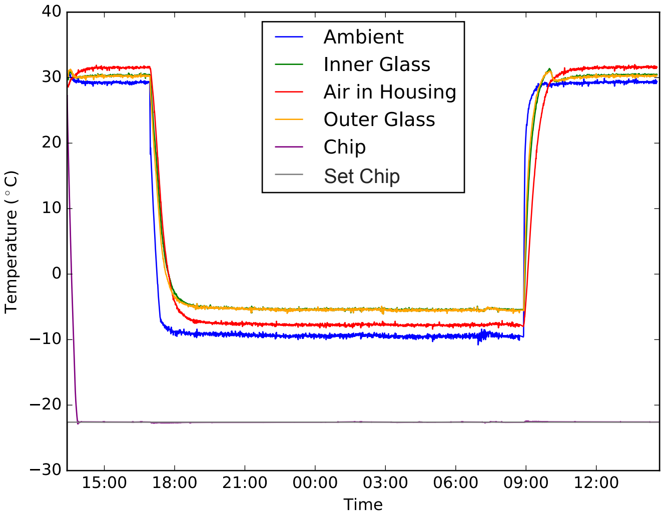

Fig. 5.11 Stability of the optimized chip temperature (-22.3 °C) at extreme working environment (-10 °C < $T_{ambient}$ < 30 °C) in the temperature chamber. The glass heater is switched on/off when the inner glass temperature is at 27 °C, therefore the air in the housing has a higher temperature than the glass when $T_{ambient}$=30 °C. (Housing with red painting)

Housing without red painting

The chip temperature of -23.2 °C is stable throughout the working temperature range in the chamber as shown in Fig. 5.10. The glass heater starts to work when the inner glass temperature is around 21 °C and the air inside the housing lays between -8.7 °C to 31 °C, which is within the working temperature for the CCD-camera itself.

Housing with red painting

The chip temperature of -22.6 °C is stable throughout the working temperature range in the chamber as shown in Fig. 5.11. The glass heater starts to work when the inner glass temperature is around 27 °C and the air inside the housing lays between -7.5 °C to 32 °C, which is within the working temperature for the CCD-camera itself. The slight shift of this range is because the glass heater has a higher switch on point, which accumulates more heat inside the housing.

In short conclusion, the optimized chip temperatures derived from the last section for the housing are stable throughout the stability test.

5.3 Outdoor Measurements

Fig. 5.12 Location for the outdoor measurement in a partially shadowed area in the summer time.

Since the air is ventilating inside the temperature chamber which facilitates the heat loss by carrying away the hot air from the heat sink, it is crucial to carry out outdoor measurements. The outdoor test was performed in a partially shadowed area in the summer time as shown in

Fig. 5.12. Due to the timing, the measurement without the painting was done in the winter time and that with the painting was done in the summer time.

In the below sections, the stability of the chip temperature, the air temperature inside the housing and the dew point for water condensation on the glass surface will be checked.

5.3.1 Dew Point and Stability Test

The dew phenomenon was discussed in section 5.1.2. To get rid of the mist, the inner and outer glass temperature must be higher than the dew point of the air inside the housing and outside the housing respectively.

Housing without red painting

The measurement is performed in the winter time over the time of nearly two weeks, where the ambient temperature nearly hit the extreme working temperature at -10 °C. During this period, both heavy snow and rain have occurred. The housing shows an excellent water resistance property. The chip temperature is set to be -23.2 °C and it is able to maintain throughout the measurement. The air inside the housing is always higher than -25 °C and lower than 40°C, indicating the CCD-camera can be operated in the housing.

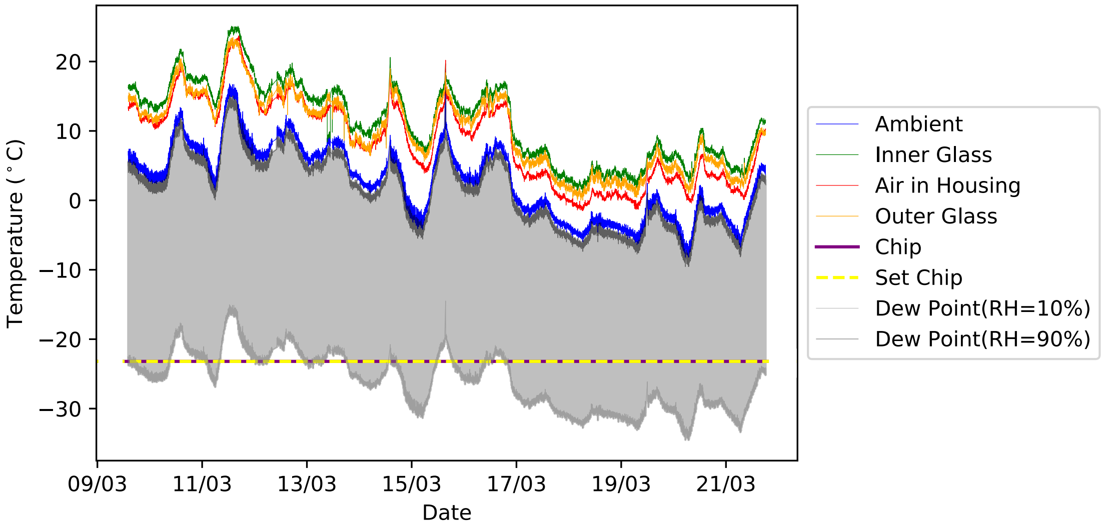

Fig. 5.13 Outdoor measurement in the Winter. The chip temperature is set to -23.2°C. The gray region is the dew point region, where mist will be formed if the glass temperature falls in this region. (Housing without red painting)

The inner glass temperature is always higher than the air temperature inside the housing, whereas the outer glass temperature is always higher than the air temperature outside the housing as shown in Fig. 5.13. Since both temperatures of the surfaces are above the dew point zone (the gray region in the graph), it is expected that no mist will be formed. This holds even if the relative humidity reaches 100 %, since both surface of the glass have higher temperature than $T_{ambient}$ and $T_{housing}$.

Housing with red painting

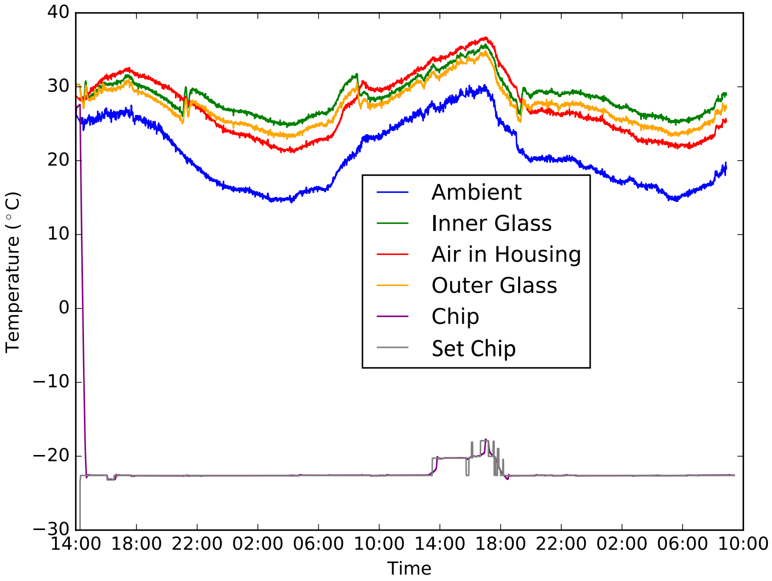

Fig. 5.14 Outdoor measurement in summer. The glass heater is switched on and off when the inner glass temperature is at 27 °C, this corresponds to the three sharp changes of inner glass temperature as shown. The chip temperature is set to -22.6 °C. The jump of the set chip temperature at 14:00 is controlled automatically by the camera to prevent overheating. The chip temperature is able to set back to -22.6 °C at 18:00. (Housing with red painting)

The measurement is performed in the summer time for nearly two days, where the maximum ambient temperature nearly hits the extreme working temperature at 30 °C. During this period, thunderstorm had happened. The housing again shows an excellent water resistance property. The chip temperature is set to be -22.6 °C.

The air temperature inside the housing is always higher than -25 °C and lower than 40 °C as shown in Fig. 5.14, indicating the CCD-camera can survive in the housing. However the chip temperature cannot stay stable. At the measuring time around 14:00 where the ambient temperature is about 28 °C, there is a sudden jump on the set chip temperature to about -20 °C. The jump is solely and automatically controlled by the camera. The possible reason is to prevent the camera from overheating since the cooling of the chip takes extra work and generates more heat to the camera. Until at 18:00 where the ambient temperature drops back to around 26 °C, the chip temperature can set back manually and stay at -22.3 °C.

For the dew point test, as the outer glass temperature is always higher than the ambient temperature as shown in Fig. 5.14, no mist is expected to form on the outer glass surface. While for the inner glass, its temperature nearly hits the dew point of the air inside the housing if the relative humidity in the housing is at 90 % as shown in Fig. 5.15. However this is much less likely to happens since the whole housing will be sealed to prevent the entrance of wet air and the housing has great water resistance to prevent any possible rain from entering.

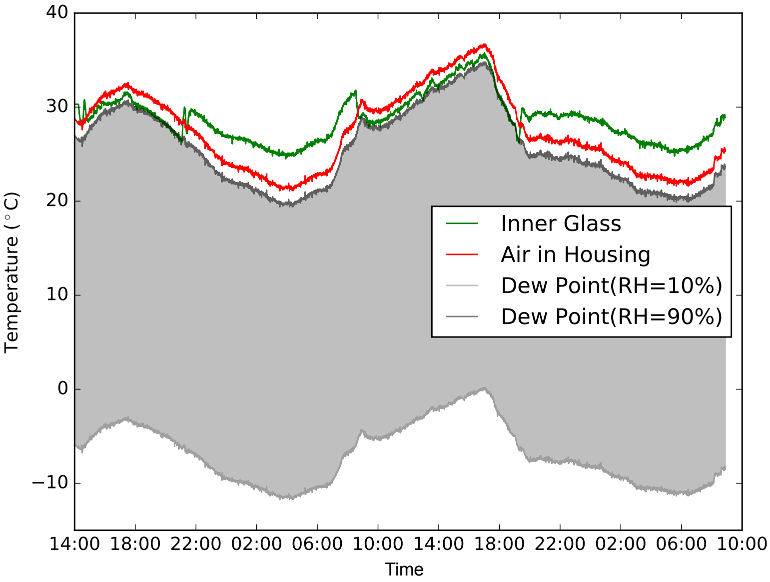

Fig. 5.15 Outdoor measurement in summer, the chip temperature set to -22.6°C. The gray region is the chip temperature that is set. (Housing with the red painting)

In conclusion, the chip temperature is stable at the required working temperature of the CTA and at the low extreme ambient temperatures, but not at the high extreme ambient temperature (which is above 28 °C). The inner glass may have mist being formed on its surface if the relative humidity in the housing is above 90% at the high working temperature.

These problems can be solved by switching on the cooler at night time and switching off at day time, since the telescope is not in operation at day time. This could prevent the overheating of the camera, which would causes a jump on the set chip temperature. Though the housing will be completely sealed to prevent wet air entering into the housing, an anti-humidity bag can be put inside the housing such that the humidity will not exceed 90 % for safety. The glass heater can also be set to switch on at a higher point, though it is not necessary in this case.

Notice that for the measurement with the red housing, the temperature sensor for measuring the ambient temperature is put under the housing, which is always in the shadow, while the housing is partially hit by the sun. In this case, $T_{housing}$ is at 33 °C when the $T_{ambient}$ is at 28 °. While for the chamber measurement, $T_{housing}$ is at 31 °C when the $T_{ambient}$ is at 28 °. The higher temperature in the housing during the outdoor measurement is because of lack of wind and partial exposure of the housing to the sun. Thus at the point where the chip temperature cannot stay stable, $T_{ambient}$ is probably already exceed 30 °C.

5.4 Test Run at La Palma

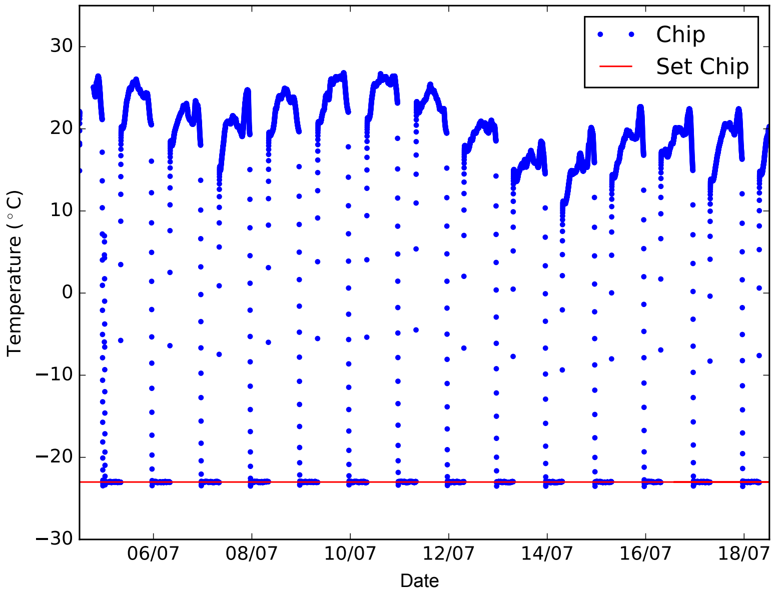

Fig. 5.16 Outdoor performance test in La Palma. The red line is the temperature set to the chip and blue dots are the measured chip temperature. The chip temperature is set at -23 °C. The thermoelectric cooler for cooling the chip is switched off during daytime.

Finally the red housing together with the CCD-camera is transported to La Palma to perform measurements under realistic conditions at the MAGIC telescope. The cooling element of the chip operates at night time and is turned off at day time. The external temperature sensors are not shipped to La Palma, therefore only the chip temperature can be read out. The chip temperature is set to be -23 °C and is able to maintain throughout the measurement at night time as shown in Fig. 5.16. The chip temperature is set lower than the optimized chip temperature in the red housing (-22.6 °C) by considering that no wind will be shielded at the measurement site at La Palma, which means the chip temperature has the chance to reach lower values. Also the thermoelectric cooler for the chip is not operating at day time where sun hits the housing, the decrease in the set chip temperature will not affect the chip temperature stability.

5.5 Summary

In this chapter, the design of the new housing is updated and the performance of the housing is being explored without and with the red painting. In all measurements, the air temperature inside the housing is in the range of -25 °C < $T_{housing}$ < 40 °C, which indicates that the camera can be operated in the housing. The optimal chip temperature at the extreme working environment is -23.2 °C using the housing without the red painting, and is -22.6 °C using the red housing based on the test in the temperature chamber. This chip temperature is only unstable at $T_{ambient}$ > 28 °C in the outdoor measurement. Yet it could be solved by turning the cooler off at day time to prevent the overheating of the camera. The chip temperature of -23 °C remains stable in the real measurements at La Palma. No mist is expected on both the outer and inner glass surfaces when the relative humidity inside the housing is below 90 %, meaning the new design for the glass heater works well.

Both the CCD-camera and the housing ensure the precise pointing. In the next chapter, the pointing ability of the single-CCD concept will be examined mainly using simulated images and at the end on real images. Finally the effect of the chip expansion on pointing will be investigated.

Chapter 6

Pointing Simulation

The pointing calibration is done by taking sky images using the CCD-camera that is mounted on the mirror dish of the Cherenkov telescope. To analyze the pointing direction, one needs to extract spots on sky images and calculate the transformation between spots and positions on the sky. To do so, the software **astrometry.net** (Lang et al. [13]) contains tools for the star extraction as well as for the transformation of the corresponding stars in pixel-coordinates to radec-coordinates. However the inner working algorithm of the code is largely undocumented and hard to understand in detail. It demands the input of various parameters for the spot extraction, which is confusing for the users. Also, it cannot get rid of the Cherenkov camera lid and the camera support structure that appear in real images. Due to these facts, the software libraries **libCCDCamera** and **libpointingMST** that are written in C++ have been developed by Domenico Tiziani in order to establish a simple and clear pointing reconstruction solution.

In this chapter, the working ability of the new tool **libpointingMST**, which includes the star extraction (**image2xy**) and pointing reconstruction (**xy2radec**) will be examined mainly using simulated images generated by **libCCDCamera** based on the Tycho-2 catalog at the exposure time of 20 s and 30 s, and at last will be tested on real images. Finally the effect of the chip expansion on pointing will be investigated.

6.1 Workflow of Pointing Reconstruction

As mentioned in Chapter 3, the pointing of MSTs can be done by mounting a CCD-camera on the telescope mirror dish such that the CCD-camera can capture images of both the Cherenkov camera and the surrounding night sky simultaneously. These images can be analyzed by comparing the known positions of reference stars on the sky with star positions in the image.

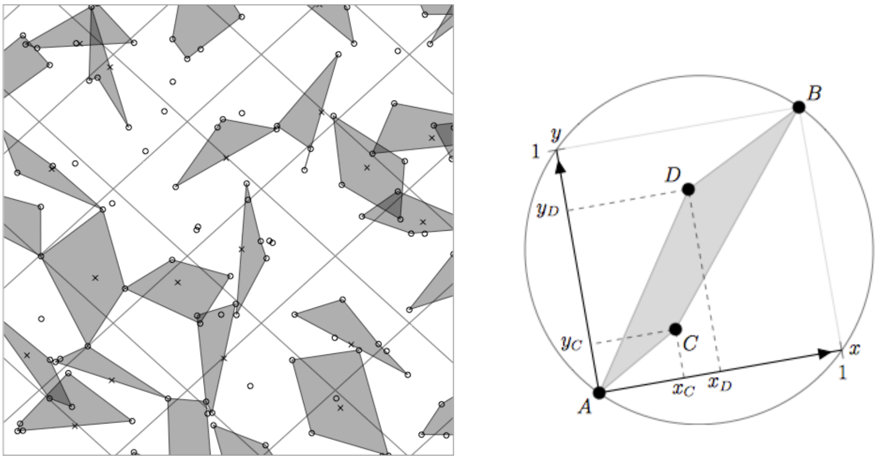

(a)

(b)

Fig. 6.1 (a) The building of the index file: a grid divides the sky into different sections. Four spots are being picked as the quad and the center of gravity of each quad falls into one grid. Each quad has the corresponding geometric hash code. (b) Illustration of the geometric hash code for a quad of stars. Stars A and B are defined in the local coordinate system as the origin and (1, 1) respectively, in which the positions of stars C and D are computed. The coordinates (x_C, y_C, x_D, y_D) are the geometric hash code that describe the relative positions of the four stars. The hash code is invariant under scaling, rotation and translation of the four stars. (Lang et al. [13])

To do so, one firstly needs to extract star positions in the image. This can be done by using the star extraction tool, **image2xy**, which is part of **libpointingMST**. After extracting the star positions in pixel-coordinates, they need to be reconstructed into sky positions in the equatorial-coordinates (right ascension and declination). This can be achieved by searching for 4-star constellations in the image in pre-compiled index-files which comprise geometric hash-codes of star positions taken from a star catalog. The building of the index file can be seen in Fig. 6.1(a). The geometric hash-code describing the relative positions of all stars in a quad is generated as shown in Fig. 6.1(b). The hash-code is invariant under translation, scaling, and rotation of the four stars (Lang et al. [13]). Once a hash-code matches the hash-code in the index file that is based on the Tycho-2 catalog, the remaining spots that also match the hypothetical positions of catalog stars will be fitted to the catalog stars positions in the index file. The fitting model will twist, rotate, scale and translate these stars with respect to the World Coordinate System (WCS).

The algorithm for the fitting is a loop of random search. It consists of four smaller loops of different nonlinear derivative-free optimizations (called fit1, fit2, fit3 and fit4, will be further discussed in Section 6.4.3) to search for the minimum χ^2. They will adjust the fitting parameters until the χ^2 reaches minimum or a specified time limit is hit (currently set to one minute because a rapid reconstruction is essential). If the reconstructed positions pass the χ^2 test of the fitting model, the result will be accepted and one gets the spot positions from pixel-coordinates to equatorial-coordinates; else spots will be fitted with another random seed until they pass the χ^2 test or when the processing time hits the time limit.

By comparing the reconstructed pointing direction (the best result from one of the nonlinear optimization loops) with the simulated pointing direction, the pointing accuracy can be determined.

6.2 Workflow of Simulation

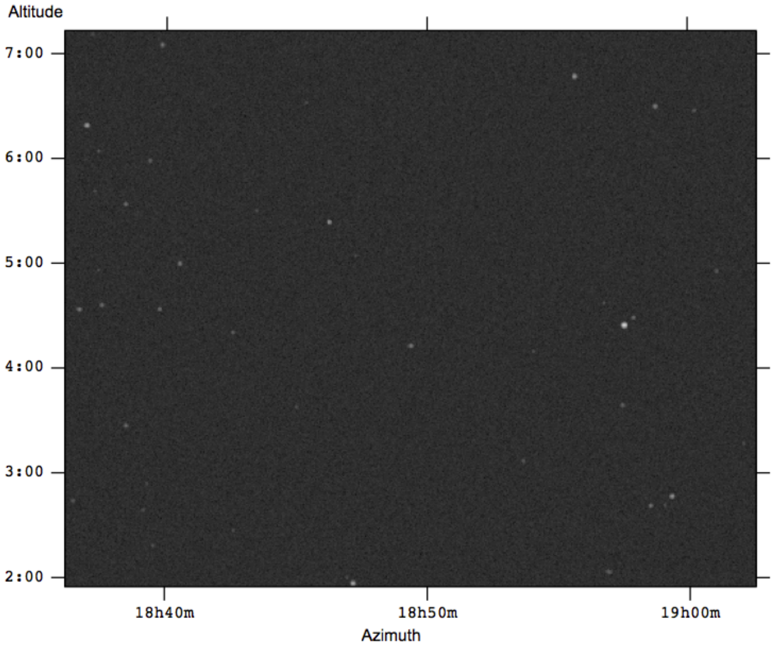

Fig. 6.2 An example of a simulated image (zoomed in).

The library **libCCDCamera** is the core for the simulation. In this library, stars in sky positions are retrieved from the Tycho-2 catalog that contains positions and proper motion information for the 2.5 million brightest stars in the sky (NASAWebsite [17]). The simulation requires the input of few parameters, including the date-time, the altitude and azimuth range for the observation, a cut on the maximum apparent magnitude of catalog stars to be included in the simulation, the exposure time, the focal length of objective, the CCD geometry and more. One can also simulate the atmospheric refraction, the horizon, the photon collecting efficiency and the confusion-factor which will be presented in the real application. The detail description of used parameters are shown in Appendix B. After the input, the corresponding star positions in the catalog are transformed into pixel-coordinates through projection. Since the catalog contains the proper motion information of the stars, their coordinates in discrete time-steps will be added up based on the exposure time (Tiziani [25]).

An example of a simulated image is shown in Fig. 6.2. Notice the effect of spot deformation as discussed in Section 3.2.2 is not included in the simulation.

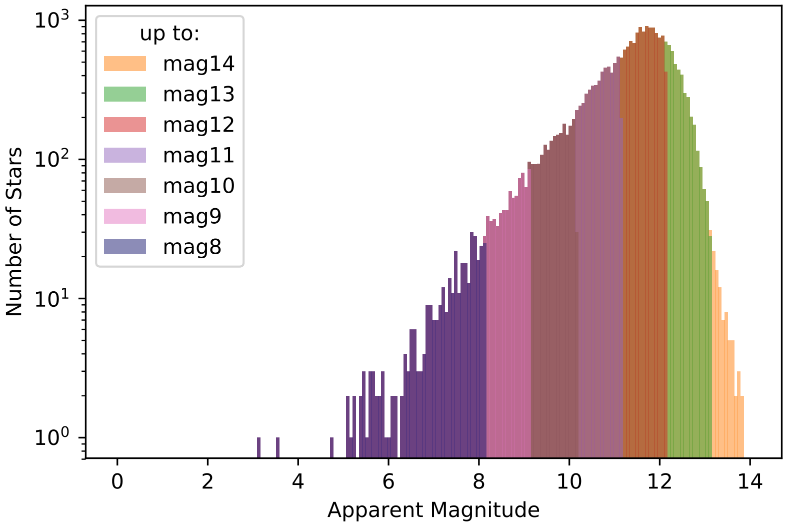

Fig. 6.3 The distribution of stars up to various apparent magnitudes (indicate with different colors) in the simulation based on the Tycho-2 catalog. The y-axis is in log-scale.

By changing the maximum magnitude of stars that will be included in the simulation, different star distributions arise as seen in Fig. 6.3. The catalog is not complete as there are less stars generated with apparent magnitude above 12 and it does not contain stars with apparent magnitude larger than 14. However stars with magnitude above 12 are not our observing targets since they only give faint brightness and thus easily miss-regarded as the background.

The background of the simulation is built based on a noise file. This noise file includes values for pedestal and noise level derived from measurements. It is crucial to have a double check on the background noise in the simulation before the test. By plotting the pixel value (intensity) of every pixel (3296×2472) in a simulated image with stars up to apparent magnitude 8, 9 and in the case where no star is simulated, the pixel intensity of the background noise is seen to be within the pixel range of the other two distributions as shown in Fig. 6.4. The typical background noise has pixel intensity ranging from 1600 to 2400, which is very faint.

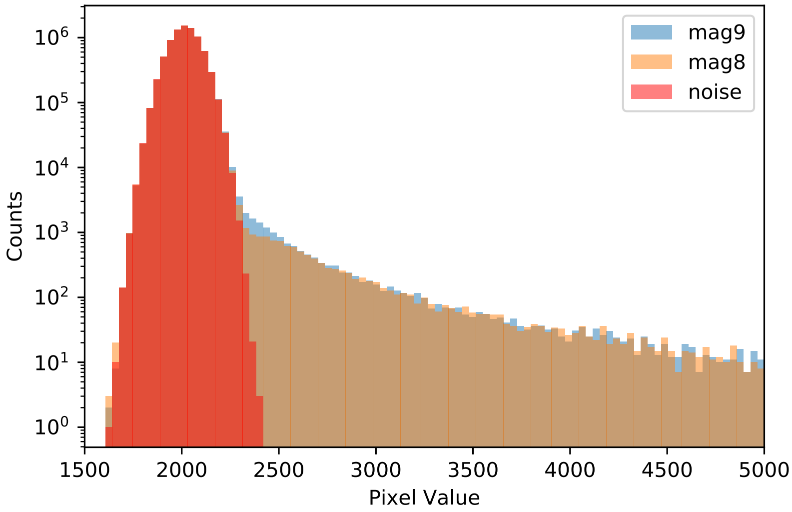

Fig. 6.4 Pixel value (intensity) distribution of all the pixels (3296×2472) in a simulated image. Red is the case where no stars are simulated, blue is the simulation with catalog stars up to magnitude 9 and orange is with catalog stars up to magnitude 8. The y-axis is in log-scale.

Notice the distribution with catalog stars up to magnitude 9 has a bit more stars at the pixel value range at 2350 to 2600. These extra stars are with the apparent magnitude 9 and their pixel intensities are close to the background noise. Stars with even less brightness are expected to fall further into this noise pixel range, leading one cannot distinguish and extract them out.

Although simulated images are different from real images (i.e. no star deformation in the simulation and the distribution of the background noise might deviate from the night sky background), the simulation is still a very good way to optimize the star extraction parameters and to check the reconstruction ability of **libpointingMST** in different conditions (i.e. how the exposure time affects the reconstruction ability). In the following sections, the performance of **libpointingMST** will be tested.

6.3 Star Extraction

The CCD-camera will capture the sky image together with the lid of the Cherenkov camera and the camera support structure (together called the mask), stars within the field of view cannot be all seen in the image as they are shadowed by this mask. Only about 1/3 of the stars that are within the image can be captured as shown in Fig. 6.5. To achieve a precise reconstruction, it is important to extract as many spots that match with simulated catalog stars

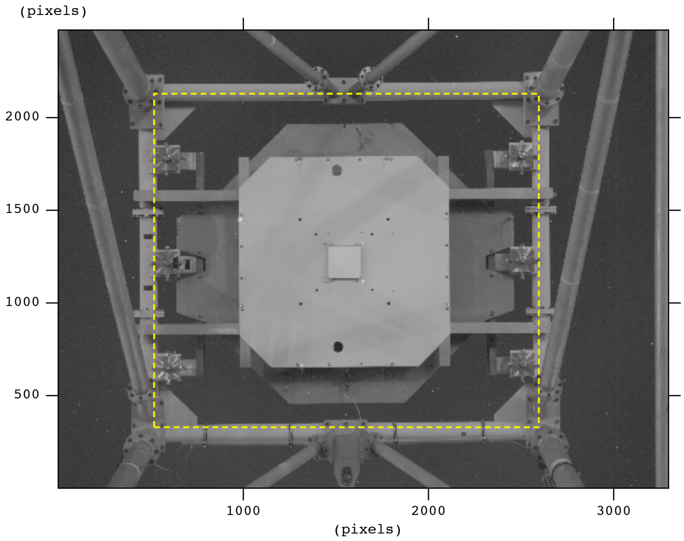

Fig. 6.5 An example of a real image. The camera support structure is shown and the Cherenkov camera will be mounted on the yellow dashed region in the image. Only 1/3 of the sky can be captured by the CCD-camera.

as possible because later more matches to the hypothetical reference stars can be found. This can reduce the chance of a wrong fitting by utilizing more reference spots. At the same time it is crucial to extract as little false positive, called noise spots, as possible, as these noise spots might create huge errors on fitting. These noise spots are mainly from the mis-extraction of the background.

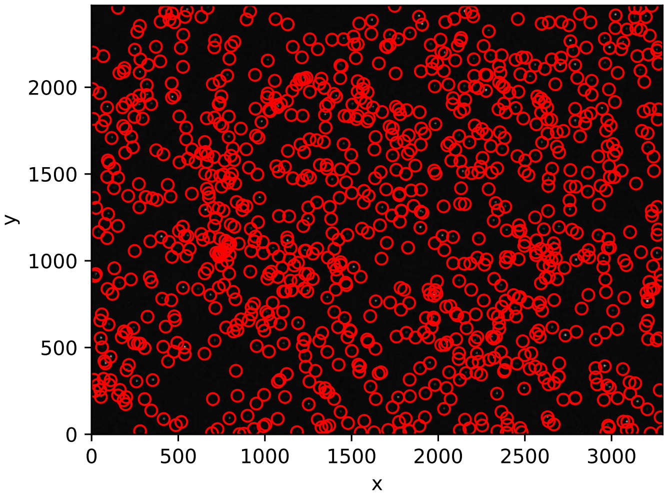

Fig. 6.6 A simulated image with a maximum magnitude cut at 9 showing an example of star extraction using **image2xy** in the **libpointingMST**. The x and y axis are in the unit of pixel. The red circles indicate extracted spots that match with simulated catalog stars in position.

To extract star positions for the reconstruction, a star extraction tool is needed. **Astrometry.net** is an open-source tool for star extraction and has been investigated if it can be used for CTA. However it requires the input of many parameters which is hard to utilize and cannot include the mask area in the extraction which will be important for the real application. Here **libpointingMST** present a new star extraction tool, **image2xy**, which demands the input of only two parameters, t and s, and a mask. The parameter t is the threshold pixel level above which every pixel in the image has to be. This threshold is calculated as $t \times \sigma$, where σ is the Gaussian sigma value of the background pixel intensity distribution of the corresponding image as shown in Fig. 6.4. The parameter s is the minimum and maximum spot size in pixels. Spots with sizes within this range will be regarded as stars. By comparing positions of extracted spots with positions of the catalog stars in pixel-coordinates using a nearest neighbor method, the number of matches (between the extracted spots and simulated catalog stars that are projected on the image) and noise spots (false positive) can be determined. Notice no precise reconstruction is done at this stage yet. An example of star extraction is shown in Fig. 6.6 where catalog stars up to magnitude 9 are simulated and being extracted.

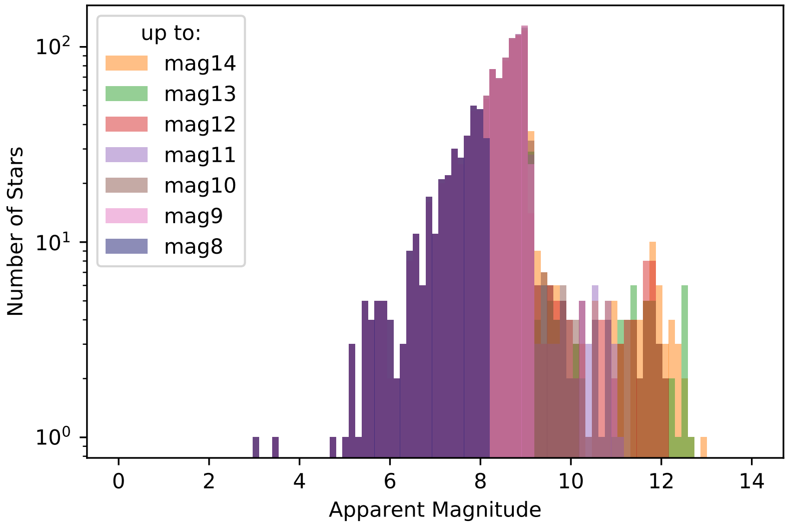

Fig. 6.7 The distribution of extracted spots that match catalog star positions of given apparent magnitudes (shown in different colors) from a simulation. Catalog stars with magnitude above 9 cannot be extracted.

Before the optimization, it is important to firstly test the limit of the star extraction tool. By using loosest possible parameters without exceeding the CPU time (the High Performance Computing of the Erlangen Regional Computing Center will kill a job if the proceeding time is too long), the maximum number of spots, as well as noise spots, are extracted. By plotting distributions of the number of matches in simulations with different cuts on the maximum apparent magnitude, one observes that the star extraction tool can only extract stars up to magnitude 9 even if a higher apparent magnitude cut is made, as shown in Fig.6.7. This is because stars with magnitude above 9 have small pixel intensity and require even looser parameters for extracting tiny and faint stars. Notice the little tail in distributions with the apparent magnitude above 9 is probably due to the false positive recognition by using the nearest neighbors method, since using loosest star extraction parameters outputs too many noise spots.

For the simulated image shown in Fig. 6.6, 1101 catalog stars are simulated. There are 2386 spots being extracted from this image by using loosest extraction parameters. 84 of them match with catalog star positions in pixel-coordinates and 1402 are noise spots. Since the goal is to extract as many spots that match catalog star positions as possible and as little noise spots as possible, this urges the need to optimize extraction parameters before use. The optimization will be done in section 6.3.2. By considering the simulation of stars with a high magnitude will be filtered out by using harder parameters and it requires much more simulation time, the cut on catalog stars up to magnitude 9 will be applied in the following sections.

6.3.1 Variation of Exposure Time

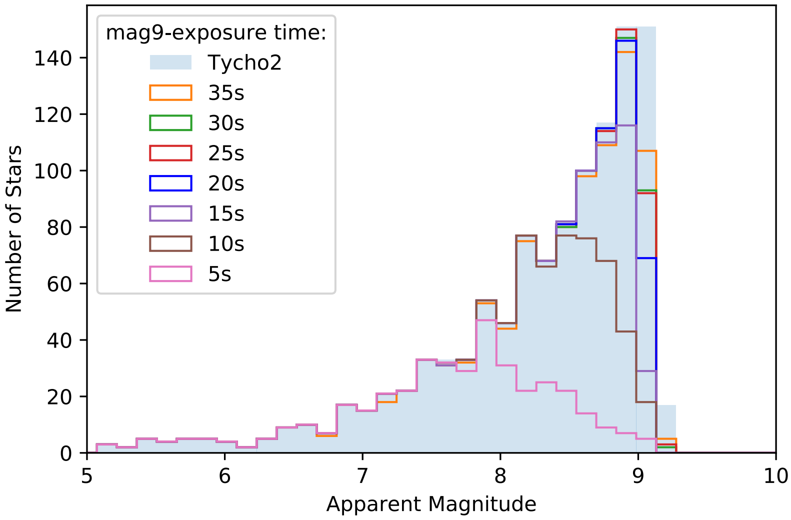

Fig. 6.8 Distributions of extracted spots matching (in position) catalog stars up to apparent magnitude 9 at the given exposure time (indicate with different colors) of the same simulated image. The distribution filled with blue is the catalog stars distribution, which is independent on the exposure time.

Since the exposure time affects the visibility of spots in images especially in the dark environment as demonstrated in Chapter 4, it is interesting to investigate how it affects the star extraction ability. By using simulations with a cut on catalog stars up to magnitude 9 with different exposure times and using loosest extraction parameters without exceeding the CPU time, the distribution of number of matches with the given exposure time is shown in Fig. 6.8. It is clear that by increasing the exposure time, more simulated stars with higher apparent magnitudes can be extracted. However this number reaches a critical value at the exposure time of 20 s, a further increase of the exposure time does not increase the number of matches much, the peak of the distribution is almost identical to that from the catalog. Therefore the exposure time of 20s will be chosen for the simulation by considering less simulation time is needed.

6.3.2 Parameter Optimization

Recalling Fig. 6.4 which shows pixel value (intensity) distributions in simulations with and without stars. It is clear that the pixel intensity of the background noise lays within the pixel intensity range of the distribution that is with simulated stars. To get rid of the noise, one can consider a cut on the pixel value at around 2400. Since the Gaussian sigma value σ of the distribution is around 74 and the minimum pixel value of an image is at around 1620, this indicates that the parameter t set at 10.6 can cut off all the noise in that image (corresponds to Fig. 6.6), only catalog stars are remained. However if this cut is applied, only 173 out of 1101 catalog stars are left, which is less than a quarter of original catalog stars for the extraction.

Providentially there is another way to optimize the extraction ability by using the other parameter s. Since noise spots are expected to be small and will take at most the area of one pixel, one can actually eliminate the noise spots by increasing the lower limit of the spot size. Here the effect on different t and s towards the matching efficiency and the percentage of noise is investigated. The test is based on 10 simulations with random pointing direction and with the cut on catalog stars at magnitude 9 with the exposure time 20 s.

By setting t from 2 to 3 and the lower limit of s from 2 to 4 (the upper limit of s is fixed at 500), one can see the general relationship of the normalized matching efficiency and normalized percentage of noise with different t and s from one of the results in Fig. 6.9. The remaining results can be seen in Appendix C. To extract the least number of noise spots, the best combination is using $t = 2$ and $s = [4, 500]$.

For the performance comparison in the next section, the star extraction tool from **astrometry.net** has to be optimized as well. Since the tool consists of numerous parameters and only the median-filtering scale s shows a greater effect on the extraction, the rest of the parameters

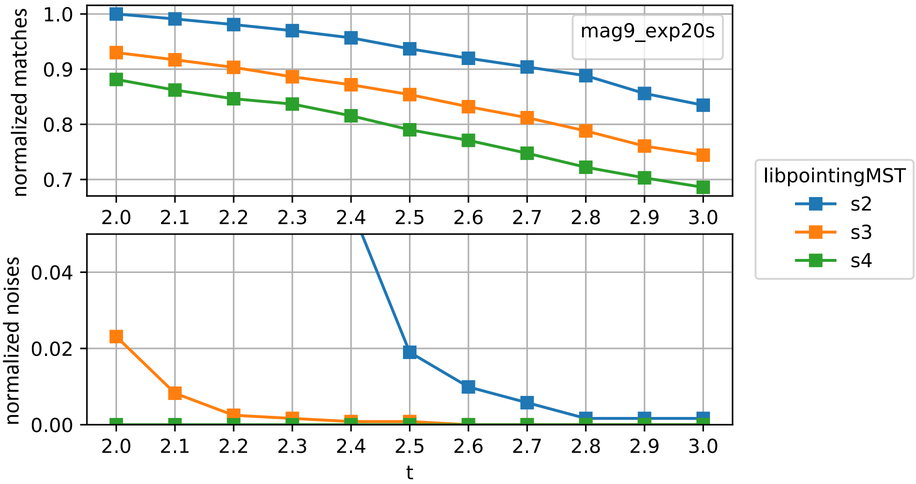

Fig. 6.9 Parameter optimization of the star extraction tool from **libpointingMST** for different t and the lower limit of s. The normalized matches and noises are shown on the y-axis. The x-axis indicates the different values of t, the different line colors represent different lower limits of s ($\min(s)$ = 2, 3 and 4 as indicated in the legend box).

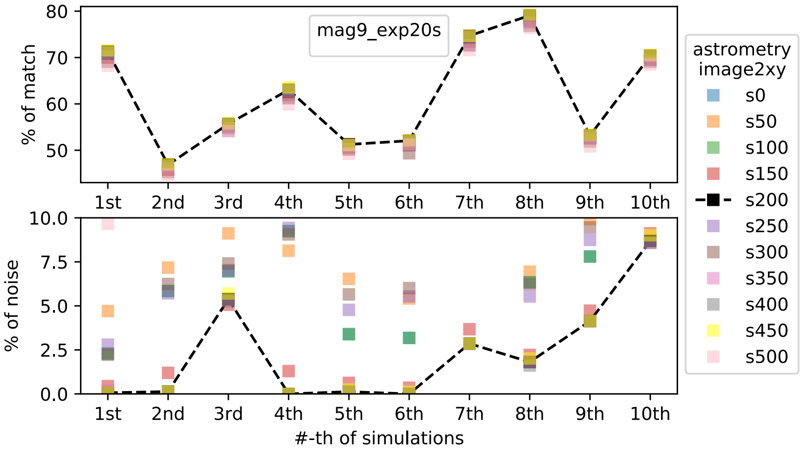

Fig. 6.10 Parameter optimization of the star extraction tool from **astrometry.net**. Different colored squares represent different values for the median-filtering scale s, the values are indicated in the legend box. The percentage of matches and noise are shown on the y-axis. The x-axis is the number-th of simulation.

are set to default values. The corresponding matching efficiency and noise percentage among 10 random images is shown in Fig. 6.10. The best extraction parameter for **astrometry.net** is $s = 200$.

Notice that the matching efficiency shown in Fig. 6.10 fluctuates among different simulated images. This feature is also seen when optimizing **libpointingMST**. The reason behinds will be discussed in Section 6.4.1.

6.3.3 Performance Comparison

The performance of stars extraction tools from both **libpointingMST** and **astrometry.net** will be explored in this section using 500 simulations with random pointing directions with a cut on catalog stars at magnitude 9 and exposure time of 20 s. The optimized star extraction parameters in the previous section are being used. Notice that some images are blank and are regarded as unusable due to the fact that they are simulated with a pointing direction below or too close to the horizon, which has large atmospheric refraction and hugely decrease the visible brightness of stars. Therefore almost no stars can be extracted in those simulated images.

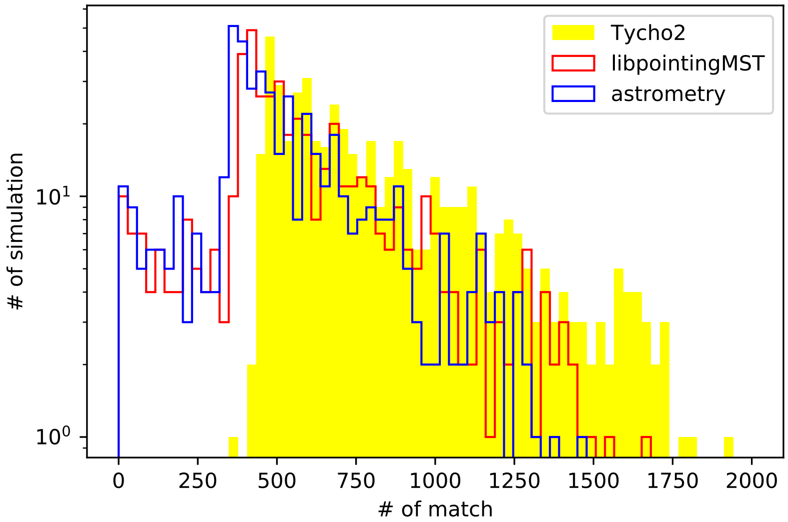

Fig. 6.11 The distribution of number of spots that matches the catalog stars positions in the simulation. Red is the distribution from **libpointingMST** and blue is the distribution from **astrometry.net**. Yellow is the distribution of number of catalog stars generated among 500 simulations.

The stars distribution extracted from 500 simulated images can be seen in Fig. 6.11. The distribution from **libpointingMST** is closer to the distribution from the catalog and there are much more distributions at 1300 to 1500 matches. This can be due to **libpointingMST** is more capable to extract faint stars with magnitude at 9.

The distribution of both tools in percentage of matches and percentage of noise is shown in Fig. 6.12. The matching efficiency of **libpointingMST** peaks at around 85% while that

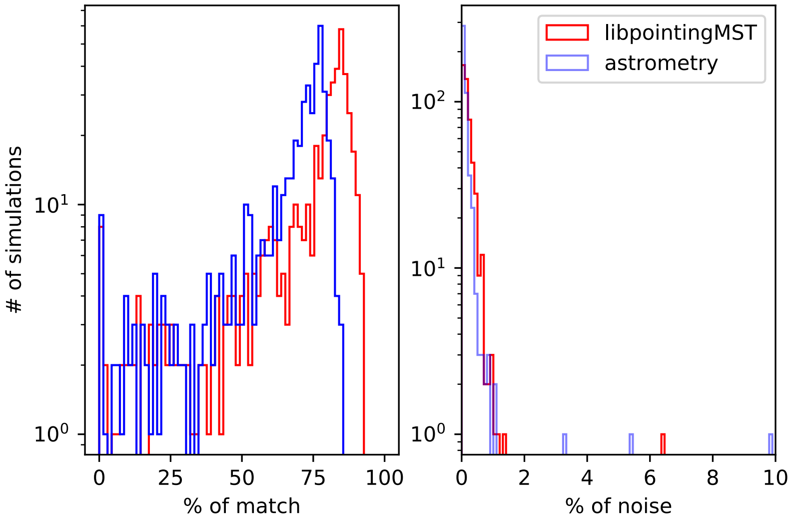

Fig. 6.12 Distribution of matching efficiency (left) and noise percentage (right) from **libpointingMST** (red) and **astrometry.net** (blue) among 500 simulations

from **astrometry.net** peak at 75%. Both tools give a similar noise distribution. This indicates that **libpointingMST** has a better star extraction ability. Notice that there exist a number of images with exceptionally low matching efficiency. This will be further discussed in Section 6.4.1.

Alternative Optimization

Though **libpointingMST** gives a better matching efficiency than **astrometry.net**, there is still another way to optimize the performance of **libpointingMST** by looking at the pixel intensity of the spots from an image and the integrated flux (the sum of the pixel intensity in a spot area after subtracting the background) of the spot from the output of the star extraction tool.

To do so, spots are extracted using loosest parameters without exceeding the CPU time, which are $t = 2$ and $s = [2, 500]$. By plotting the pixel value of each extracted spots versus the corresponding integrated flux, a linear relation is observed in an example shown in Fig. 6.13. Noise spots are at the one end of the graph, where both pixel values and integrated flux are low. This brings up an idea of implementing a cut on small pixel intensity and small flux value of extracted spots.

By looking at distributions of the maximum integrated flux and the maximum pixel value among the noise spots in 500 simulations in Fig. 6.14, a loose cut at 750 for the integrated flux and 2350 for the pixel value is picked. Extracted spots with value below these two cuts will be removed. Notice that the integrated flux cut is even smaller than the pixel value cut

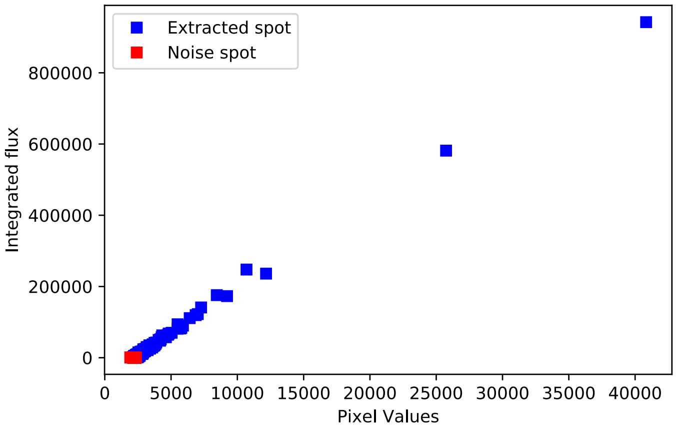

(a)

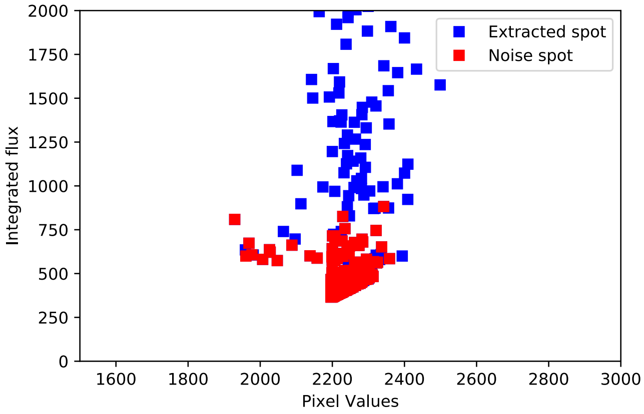

(b)

Fig. 6.13 Top: The pixel value versus the integrated flux for each extracted spot using loose extraction parameters ($t = 2$ and $s = [2, 500]$) in a simulated image. The blue spot are the extracted spot. Red spots that overlap blue spots are noise spots. Bottom: Zoom in.

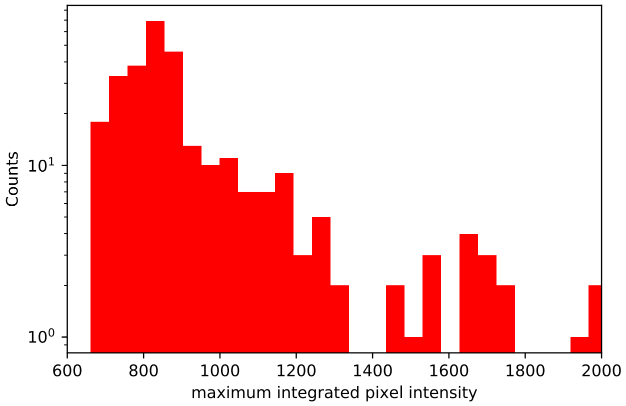

(a)

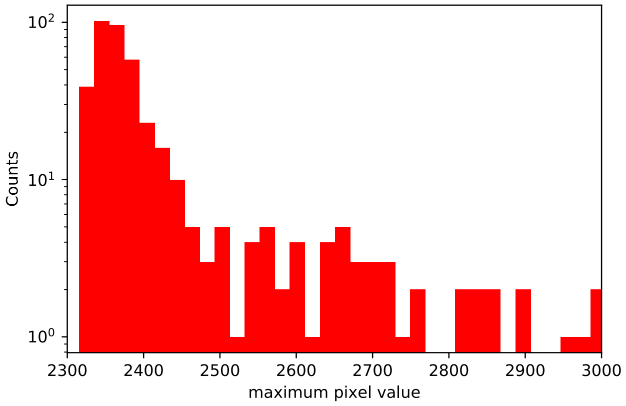

(b)

Fig. 6.14 The distribution of maximum integrated pixel intensity (a) and maximum pixel value (b) for the noise spots in each simulation among the 500 simulations.

because the integrated flux is calculated after subtracting the background. These fixed cuts are then applied to the rest of the simulated images.

The result is indeed surprising. Fig. 6.15 shows that the matching efficiency after a pixel intensity cut on all sets of extracted spots is not as good as expected, it only peaks at around 61 %. Yet the matching efficiency after an integrated flux cut on all sets of extracted spots is about 89 %, which is 4 % better than by just setting the harder parameters ($t = 2$ and $s = [4, 500]$) and at the same time their noise percentage distributions are similar. This is due to the cut removes noise spots directly without eliminate too many faint stars that are outside the extraction constraint set by the harder parameters.

However this alternative optimization is not as applicable as using the harder parameters. In the simulation, positions of noise spots are already known by comparing the spot positions with catalog stars positions, thus one can set the cut-value. In real images where the

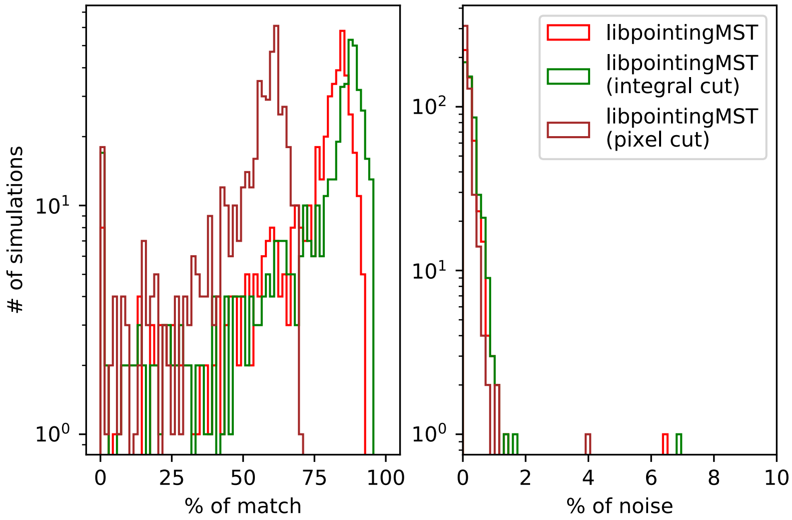

Fig. 6.15 Distribution of matching efficiency and noise percentage from **libpointingMST** among 500 different simulations. Red is with harder threshold ($t = 2$ and $s = [4,500]$), green is with looser threshold ($t = 2$ and $s = [2,500]$) and the integrated flux cut, brown is with ($t = 2$ and $s = [2,500]$) and the pixel value cut.

background noise level is different (i.e. due to the night sky background), the cut may not be the same in all images. Based on the fact that although the integrated flux cut gives a better matching efficiency, yet the efficiency is not significantly better, the hard parameters will still be used for the star extraction in this chapter.

In this section, it is proved that the star extraction tool **libpointingMST** is able to extract stars up to the apparent magnitude of 9 in the simulation with the exposure time of 20s. The tool gives a matching efficiency of 85%, better than that from **astrometry.net** which is 75%. The higher matching efficiency and the requirement of fewer input parameters prove the excellent working ability of **libpointingMST** on spots extraction. In the next section, the reconstruction ability of **libpointingMST** will be examined.

6.4 Pointing

After the optimization of the star extraction tool from **libpointingMST**, the reconstruction ability can be tested in this section. Here a pointing analysis will be demonstrated. After simulating an image, spots are extracted out as seen in Fig. 6.16 using the stars extraction tool with the optimized parameters.

By passing the extracted spots to the reconstruction tool **xy2radec**, these spots will proceed to hypothetical reference stars matching as mentioned in Section 6.1. The matches

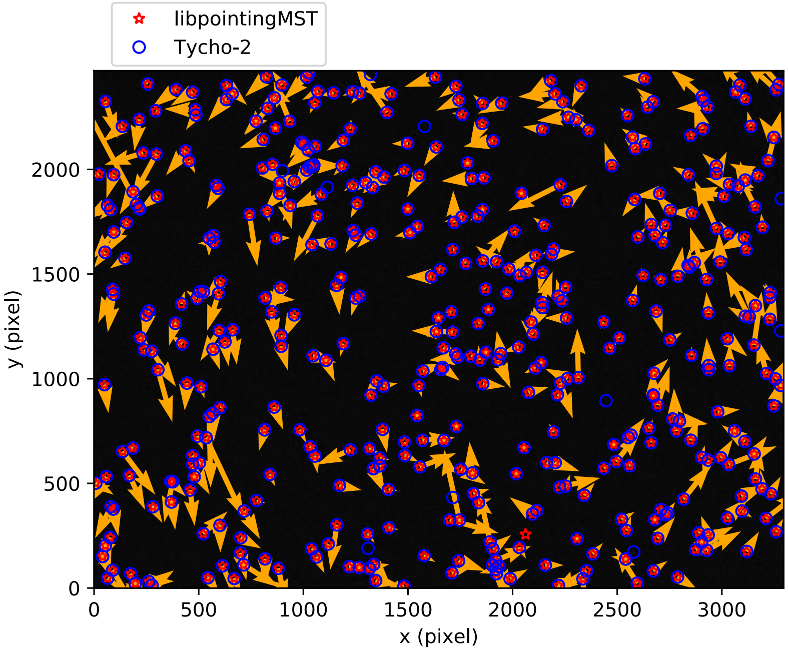

Fig. 6.16 An example of spot extraction image using **libpointingMST**. The blue circles are star positions in the catalog, the red circle are spot positions being extracted. The orange arrows indicate the distance between. The arrows are artificially 660X enlarged.

will be fitted to catalog positions from the index file based on the random seed. The model will try different parameters until the minimum χ^2 value is reached, which means a best fit is found, or when the fitting time hits a specified time limit, which is currently set at one minute. These positions are therefore transform from pixel-coordinates to equatorial-coordinates as indicated in Fig. 6.17 (a). The great circle distance (the shortest distance between two points on the surface of a sphere) distribution among these spots is shown in Fig. 6.17 (b), where the standard deviation is 1.1", and all reconstructed spots deviate smaller than 7". Notice not all extracted spots can be reconstructed successfully since some are far off the catalog stars in sky positions.

However there are some cases where the reconstructed positions do not match the catalog positions. Fig. 6.18 shows two typical examples of a failed reconstruction through mis-scaling and wrong rotation of the field due to the non-converge fit. This happens because the fitting is random based, which means starting parameters for the fitting might be too far off and that the best fit cannot be done within the scope of the fitting time. Thus to see the full working ability of the **libpointingMST**, it is crucial to look at a generally large amount of simulated images and to fit them as many times as possible.

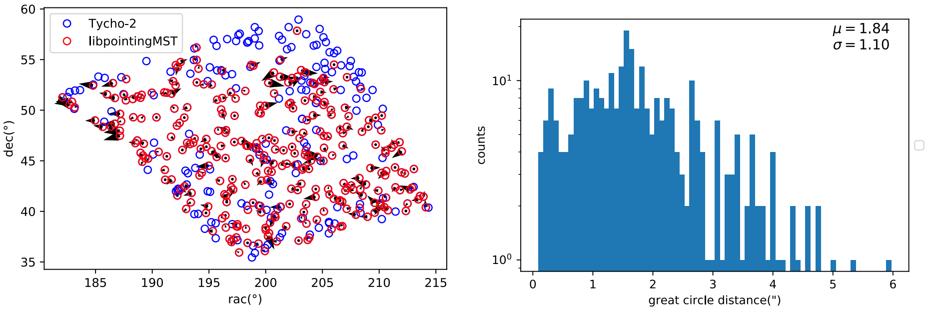

(a) (b)

Fig. 6.17 Left: the extracted spot positions being reconstructed into equatorial-coordinates. Right: the distribution of the great circle distance between all reconstructed spots and the corresponding catalog stars.

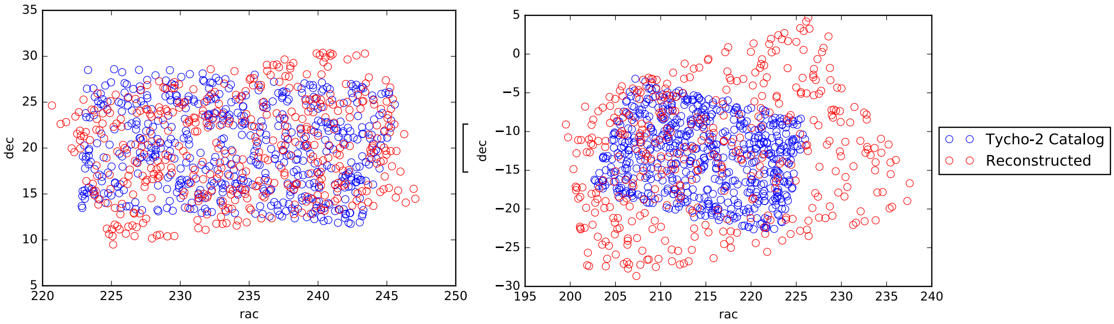

(a) (b)

Fig. 6.18 Two examples of failed reconstructions. Both the axes are in the unit of degree.

6.4.1 Problem of Fluctuating Matching Efficiency

In Section 6.3.2, it was pointed out that the matching efficiency from the star extraction is fluctuating among different simulations. This feature is not only perceived in the result from **astrometry.net** but also from **libpointingMST** as can be seen in Fig. 6.19, which shows the fluctuating matching efficiency for 10 simulations with random pointing direction. This suggests the fluctuating feature is related to something else rather than the star extraction tool. Since the matching efficiency from the star extraction might affect the number of matches to the hypothetical reference stars (generated based on a matched quad), this will essentially affect the fitting quality. Thus, it is crucial to first look into this problem.

By looking at the reconstructed pointing direction of all 500 simulations in Fig. 6.20, one can get the clue about the fluctuation. Based on Fig. 6.20, images that are near to the "boundary" of data set in radec-coordinates cannot be solved. This "boundary" region corresponds to the pointing altitude at around 0°. The simulated images (such as images

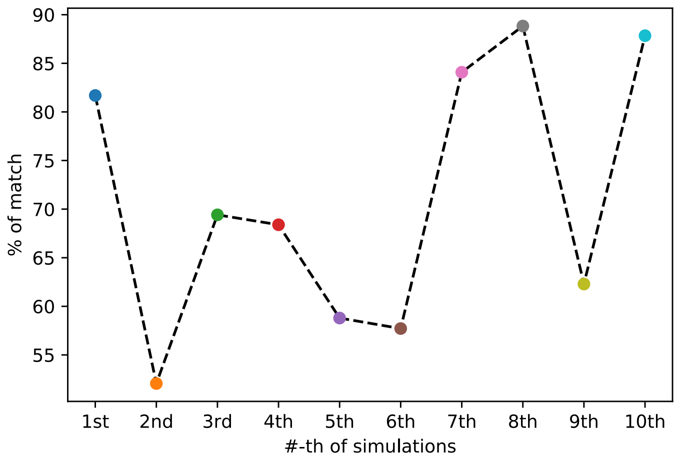

Fig. 6.19 The matching efficiency of 10 different simulations using the star extraction tool from **libpointingMST**. The color indicates different simulated images.

being labeled by orange and green dots) near this region have very low matching efficiency. This is understandable as the camera is pointing near the horizon where the atmospheric refraction is large, thus the relative brightness of stars decrease to almost invisible, resulting in narrower pixel intensity distribution and the distribution appears as the noise background as illustrated in Fig. 6.21. This faint brightness adds difficulty on star extraction and hugely decrease the number of extracted spots. When there are less than four extracted spots, a quad cannot be formed and thus the reconstruction cannot be done. Yet even if more stars are extracted out, their positions are probably not precisely extracted due to the faint brightness and thus the pointing accuracy is still bad.

On the other hand when the pointing direction is close to the "center", where radec = (250°, 40°), the matching efficiency is higher and the pointing accuracy is likely below or equal to 7". This "center" region is where the camera points closer to the zenith and has the minimum atmospheric refraction. Both the matching efficiency and the pointing precision are better because the stars are relatively brighter for the precise extraction. This is also why the the simulated image at this region has a broader pixel distribution (in color gray) as shown in Fig. 6.21. In the real application, the MSTs will point to elevations of larger than 24° (CTAWebsite [7]). Therefore the overall matching efficiency and reconstruction ability are expected to be better.

Although the random based fitting might sometimes not converge in a reconstruction, leading to a bad reconstruction result (i.e. not all images at the zenith are reconstructed precisely), one can notice from Fig. 6.20 (b) that the reconstruction is in general more precise (< 7") when the pointing direction has the azimuth above 180° and more worse

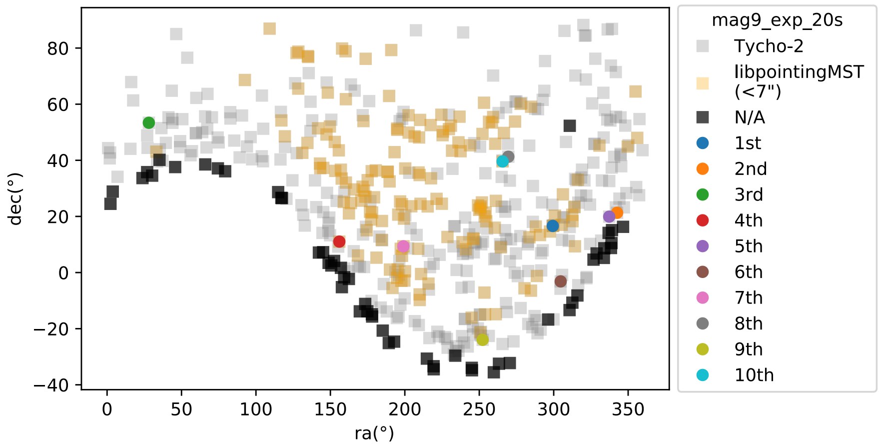

(a) ra-dec coordinate

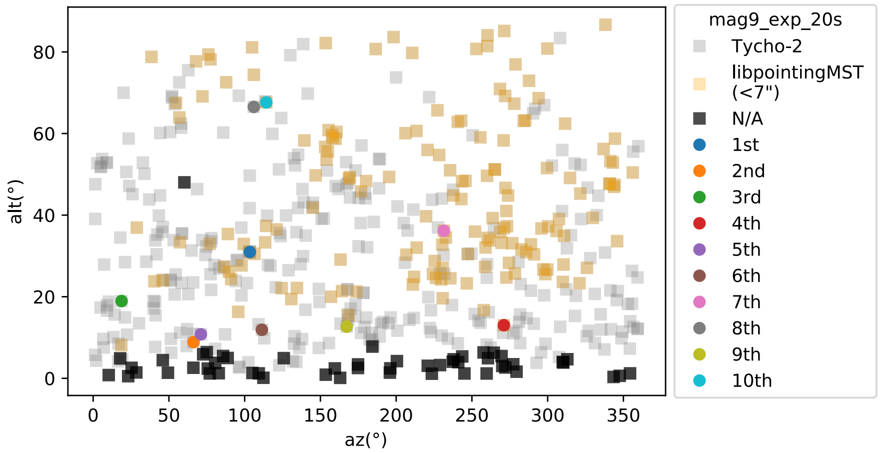

(b) az-alt coordinate

Fig. 6.20 The distribution of pointing direction among 500 simulated images in the radec- (a) and altaz- (b) coordinate. Gray are the simulated pointing centers. Orange are the reconstructed pointing centers that overlap the simulated pointing center by less than 7" precision. Black are images that cannot be solved. Other colors are the corresponding simulated images from the Fig. 6.19.

when the azimuth is below 180°. The answer can be illustrated by plotting the graph in galactic-coordinates as shown in Fig. 6.22. Except for the regions that are too close to the horizon (near the black spots), the pointing region with worse reconstruction includes where the camera points to the galactic plane which has huge amount of stars. The possible reason for the bad reconstruction is the short time limit for the fitting. When there are huge amount of stars in an image, it requires more time to find the best fitting parameters that can fit all stars. The fitting terminates before a best fit is found and thus gives the worse reconstruction.

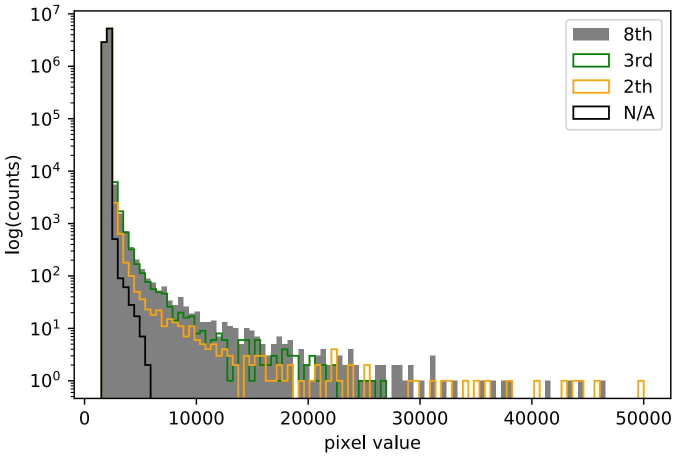

Fig. 6.21 The pixel value (intensity) distribution of the simulated images. Gray, green, yellow corresponds to the same simulated image from Fig. 6.19 and Fig. 6.20. Black is the image that cannot be solved for the reconstruction

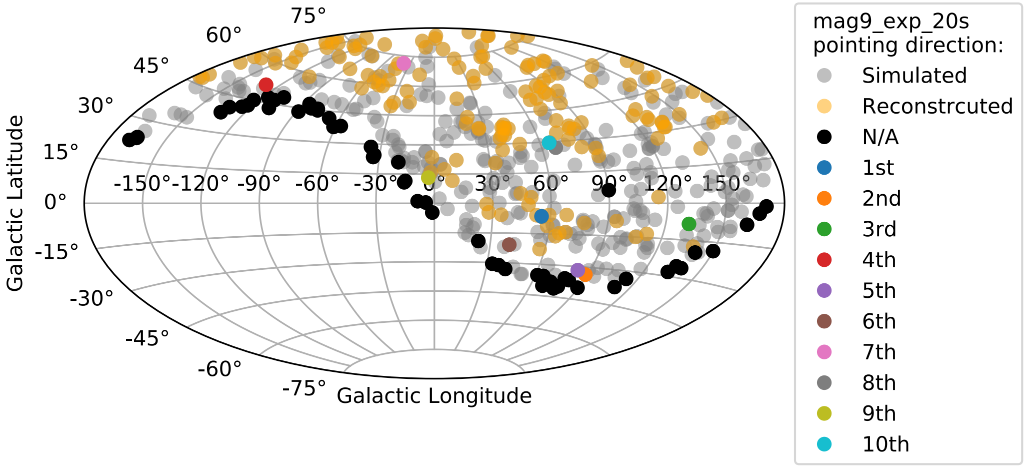

Fig. 6.22 The pointing direction distribution of 500 simulations (same as Fig. 6.20) in galactic-coordinates.

In short conclusion, it is observed that when the camera points towards the horizon where the atmospheric refraction is large, the matching efficiency for the star extraction is low and the reconstructed pointing accuracy are mostly > 7". When the camera points to the zenith where the atmospheric refraction is small, the matching efficient for the star extraction is larger and the reconstructed pointing accuracy are mostly < 7". It is also observed that when the camera points close to the galactic plane, the reconstruction accuracy of the corresponding image is worse because there are too many extracted from the image, result in a best fit for the reconstruction cannot be found within the fitting time limit. This feature will be further investigated in Section 6.4.4.

6.4.2 Variation of Exposure Time

Like previously for the optimization of the star extraction tool, it is interesting to explore whether the exposure time will affect the pointing accuracy. This is based on the measurement in Chapter 4, in which the positions of extracted corners of chessboard are affected by the exposure time. Therefore it is crucial to test whether this will affect the reconstruction ability of **libpointingMST** as well.

The study is done by looking at the reconstructed center in the simulation with different exposure times. Since the fitting is random based, it is expected that both initial starting parameters and the random seed for the fitting are different in each round, leading some results are good and some results are bad. Therefore the reconstruction is done in several rounds to minimize the this effect. The reconstruction result in each round is shown in Fig. 6.23.

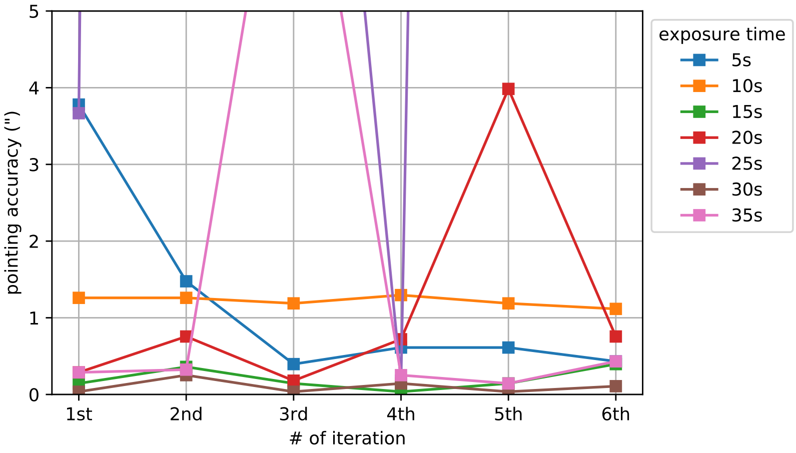

Fig. 6.23 The reconstructed pointing direction with different exposure times (indicate with different color squares) in each round of reconstruction for a simulated image located at azalt = (190.48°, 44.24°). The reconstruction is repeated for six rounds.

The relationship of the pointing accuracy and the exposure time is not very clear. Yet the general pointing accuracy discrepancy between different exposure times is within 2", which is very small. The simulation with exposure time of 30s has the best pointing accuracy among the six rounds of reconstruction. This means although increasing the exposure time to above 20 s does not further improve the star extraction ability as mentioned in Section 6.3.1, simulations with exposure time of 30 s allow the more precise stars extraction and thus give a more precise reconstruction result. Further increase the exposure time to 35 s does not improve the pointing accuracy, either due to the effect of random fitting or due to the greater field rotation which will elongate the stars appearance in the image and add the difficulty on locating the star positions.

Although the effect is small, based on the result in this section, the overall reconstruction ability will be assessed using simulations with 30 s exposure time.

6.4.3 Fitting Iterations

It is always a challenge when using the random based fitting because the results are different after each fitting. As mentioned in Section 6.1, this version of fitting algorithm consists of four smaller loops for different nonlinear optimization (called fit1, fit2, fit3 and fit4) to search for the best fit. Fit1, fit2 and fit4 use the same core of optimization algorithm while fit3 uses another core of optimization algorithm (see Appendix D). In a loop of reconstruction, stars that match the hypothetical reference stars in positions are firstly pass to fit1. By using the parameters from fit1, fitted stars are projected back to pixel-coordinates to do the re-matching. Stars that were originally hidden/not-matched might match to the catalog this time due to the. Re-matched stars will pass to fit2. If the result cannot fulfill the set constraint, the original stars (same as received by fit1) will pass to fit3. After the re-matching, these re-matched stars will pass to fit4. The reconstructed pointing direction from all four optimization algorithms can be extracted. Though one knows which optimization gives the best result by simply comparing them to the simulated center, one cannot do so in the real application since the camera optical axis is unknown. Thus it is reasonable to look at how the different optimization algorithms affect the reconstruction for the future usage.

As the fit2 and fit4 are related to the result from fit1 and fit3 respectively, the overall fitting qualities are expected to be different in each round of reconstruction. Therefore it is also reasonable to get a rough idea on how many times one should perform the reconstruction to order to get a reasonable result. Thus in this section, the optimal number of iteration of fitting is investigated for the later analysis.

The result is shown in Fig. 6.24. First it can be seen that though some optimization algorithms work better than the others in some specific cases, for example fit2 gives a better result in Fig. 6.24 (a) and (c), and fit1 gives a better result in Fig. 6.25 (b). Yet no specific optimization algorithm gives a generally best pointing accuracy among all images. This can be due to the optimization are derivative-free which are hugely affected by the random seed and some algorithm set the better initial parameters under certain cases, for example related to the distribution of stars. The re-matching process might also exclude the "good" stars and include the "bad" stars, which affect the reconstruction. This will be further investigate in

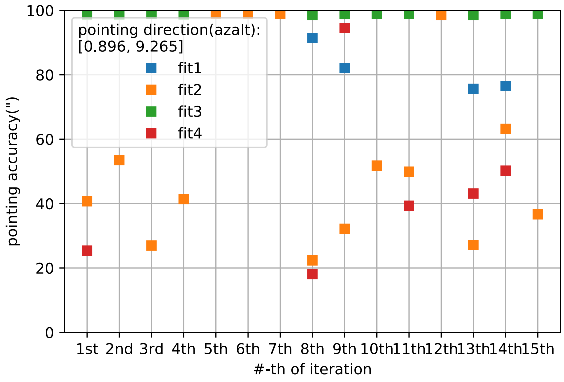

(a) close to the horizon

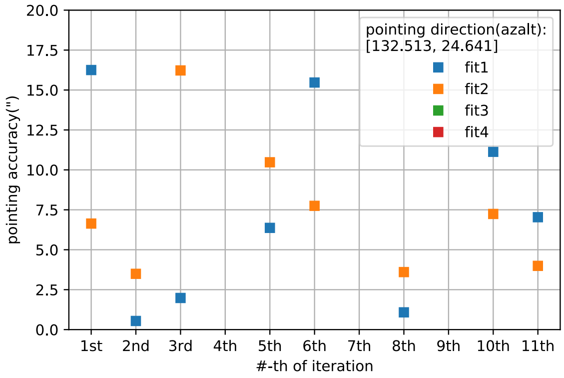

(b) away from the horizon

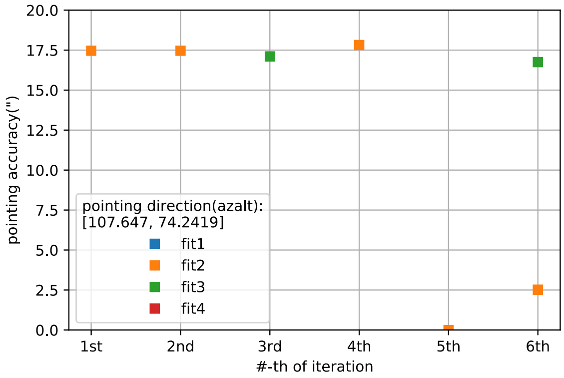

(c) close to the zenith

Fig. 6.24 The pointing accuracy of the reconstructed pointing center and the simulated pointing center at three different pointing positions. The simulated pointing directions are marked in the text box in azalt-coordinates. The x-axis indicates the number-th of round for the reconstruction and each round consists of four different optimization algorithms (fit1, fit2, fit3 and fit4 as indicated in different colors). The y-axis is zoomed in artificially, the data not shown are beyond the y-axis.

Section 6.4.4. This suggests that in the real application, one cannot only rely on a specific optimization algorithm for the fitting.

Second, the pointing accuracy cannot be improved after 15 rounds of reconstruction process if the camera points close to the horizon. The pointing accuracy are all above 20". This means by pointing to the horizon, there is nearly no chance to get the good reconstruction result. As in the real application, MSTs will points with elevation above 24°, this problem is not our concerns.

While both images that are taken closer to the zenith give a pointing accuracy smaller than 7" within 5 rounds of reconstruction process. This suggests the reconstruction result is largely affected by the different initial starting parameters and different random seed in the fitting. Therefore it is reasonable to take several round of reconstruction instead of just looking at one round. Based on the analysis in this section and the scope of this thesis, the reconstructions of 500 simulated images will be iterated for 5 rounds in the below section to see the ultimate performance of the **libpointingMST**.

6.4.4 Performance

The spot positions in pixel-coordinates are being fitted to catalog stars positions, in which they will pass the fitting model for stretching, rotating and scaling in order to match the real star positions. The model will try different parameters such that chi square value χ^2 reaches minimum. At the end, the model will output the value χ^2 and the number of matched spots N. The chi square value in the current algorithm is defined as:

$$\chi^2 = \sum (x_{star} - x_{spot})^2 \tag{6.1}$$

where x_{star} is the position of the catalog stars and x_{spot} is the position of extracted spots in pixels. By looking at $\log(\chi^2/N)$, one can identify how well each reconstructed spots match the catalog stars in sky position. Fig. 6.25 shows four plots of such graph with different fitting optimization algorithms in one round of reconstruction for 500 different simulations. They show the general feature that a smaller $\log(\chi^2/N)$ gives a better pointing accuracy. One also observes that there are several images off the linear trend, this indicate the fitting quality of different optimization loop is different. Their fitting quality will be further investigated in Section 6.4.4 IV.

In the real application, the exact optical axis of the camera is unknown. Therefore it is important to determine a universal cut on the $\log(\chi^2/N)$, such that the pointing accuracy between the reconstructed center and the simulated center (and later the real pointing center of the camera) is within 7".

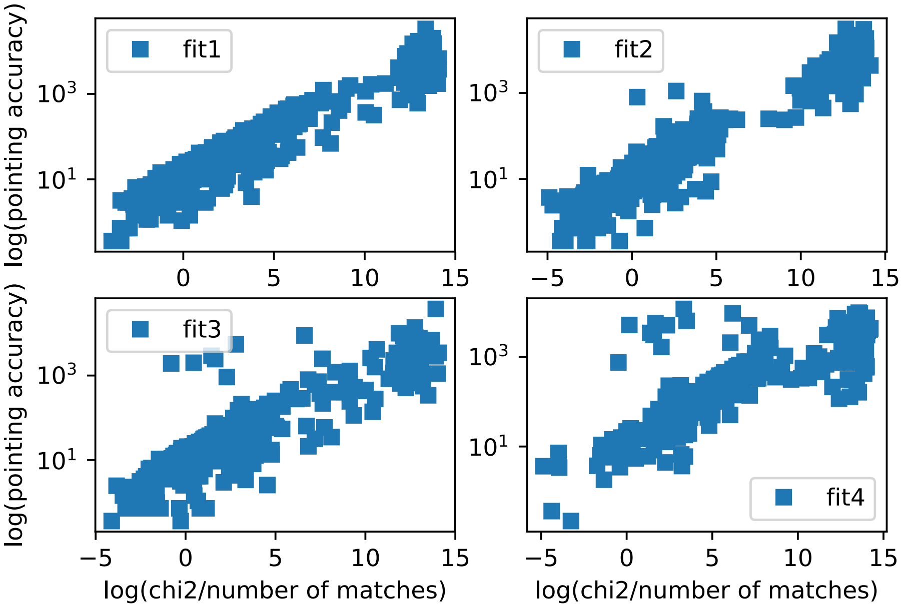

Fig. 6.25 The log(pointing accuracy) versus $\log(\chi^2/N)$ among 500 simulations for a whole round of reconstruction, which consists of four fitting optimization indicated as fit1, fit2, fit3 and fit4 in the text box in each graph.

Two sets of data containing the same 500 simulated images with exposure time of 30s and a cut on catalog stars up to magnitude 9 are tested. Both use the same star extraction parameters, which is $t = 2$ and $s = [4, 500]$, while the second set of data have included the mask area of the camera support structure that is present in real images, thus they only contain the stars outside the mask area, which is about 1/3 of the original stars. As the previous section shows that the pointing precision gets better after 5 rounds of reconstruction, these two sets of data will pass the fitting model for 5 rounds. A universal $\log(\chi^2/N)$ cut at -2 is chosen, only the reconstructed pointing direction that is below this cut from anyone of the four optimization outputs is recorded.

I. Reconstruction excluding mask

The distribution of simulated pointing direction and reconstructed pointing direction in radec-coordinates is shown in Fig. 6.26 (a). The corresponding distribution with minimum $\log(\chi^2/N)$ is shown in Fig. 6.26 (b). Among the 500 simulated images, 147 images are left after applying the $\log(\chi^2/N)$ cut at -2. Among these 147, 144 have the pointing accuracy < 7" while 3 of them are still > 7". This can be eliminated by adding more reconstruction iterations but it is beyond the scope of this thesis.

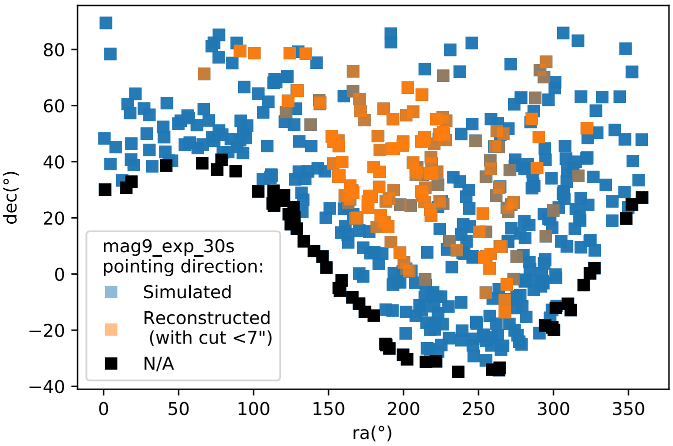

(a)

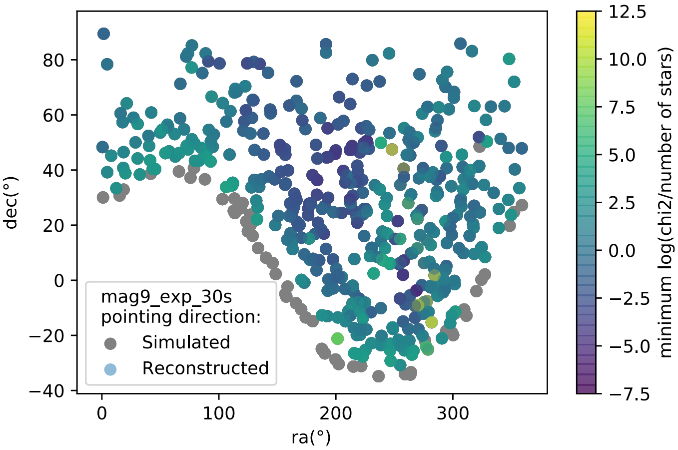

(b)

Fig. 6.26 (a): The simulated center (blue) of 500 simulations with stars simulated up to mag9 and exposure time 30s. Orange squares that overlap the blue squares are the reconstructed pointing direction with pointing accuracy < 7" by using the $\log(\chi^2/N)$ cut at -2. All images have been passed to the fitting model for 5 rounds. The data are plotted in semi-transparent color, thus the more solid the orange square is, the more time where the reconstructed center has the good pointing precision. The black squares are the simulated images that cannot be solved. (b): Same graph as above. The color indicates the value of $\log(\chi^2/N)$ of each reconstructed center. (Reconstruction excluding mask)

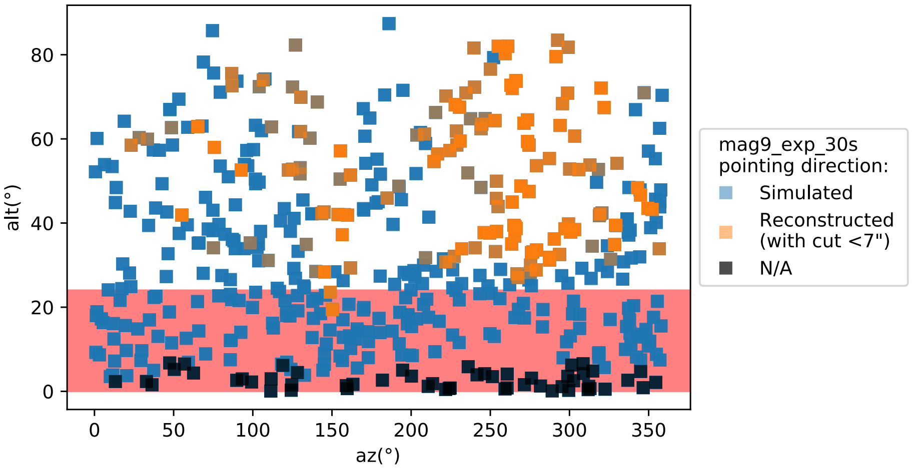

Fig. 6.27 Same graph as Fig. 6.26 (a) but in altaz-coordinates. The red region indicates that the elevation is smaller than 24°, which is too close to the horizon and below the required observation angle of the MSTs. (Reconstruction excluding mask)

The distribution in altaz-coordinates is shown in Fig. 6.27. Among the 500 simulated images, 299 have a simulated center larger than the required elevation of > 24° for the MSTs and 142 of them can be reconstructed with a pointing accuracy < 7" after applying the $\log(\chi^2/N)$ cut at -2. This gives a precise reconstruction (< 7") efficiency of 47.5%.

A summary of the results can be seen in Table 6.1

II. Reconstruction including mask

The distribution of simulated pointing direction and reconstructed pointing direction in radec-coordinates is shown in Fig. 6.29 (a). The corresponding distribution with minimum $\log(\chi^2/N)$ is shown in Fig. 6.29 (b). Among the 500 simulations images with the mask, 213 are left after applying the cut of $\log(\chi^2/N)$ at -2. Among these 213 images, 199 can be reconstructed with a pointing accuracy < 7" while 14 of them are > 7". This can be solved by adding more reconstruction iterations but it is beyond the scope of this thesis.

The distribution of simulated center and reconstructed center in altaz-coordinates is shown in Fig. 6.30. Among the 500 simulations images, 299 images have a simulated center larger than the required elevation of > 24° for the MSTs. Among them 199 images have a pointing accuracy < 7" in this region after applying the cut of $\log(\chi^2/N)$ at -2 and 21 images cannot be solved as less than four stars are able to be extracted from the image and thus a quad cannot be formed. By excluding the images that cannot be solved, this gives a high precision reconstruction (< 7") efficiency of 71.6%.

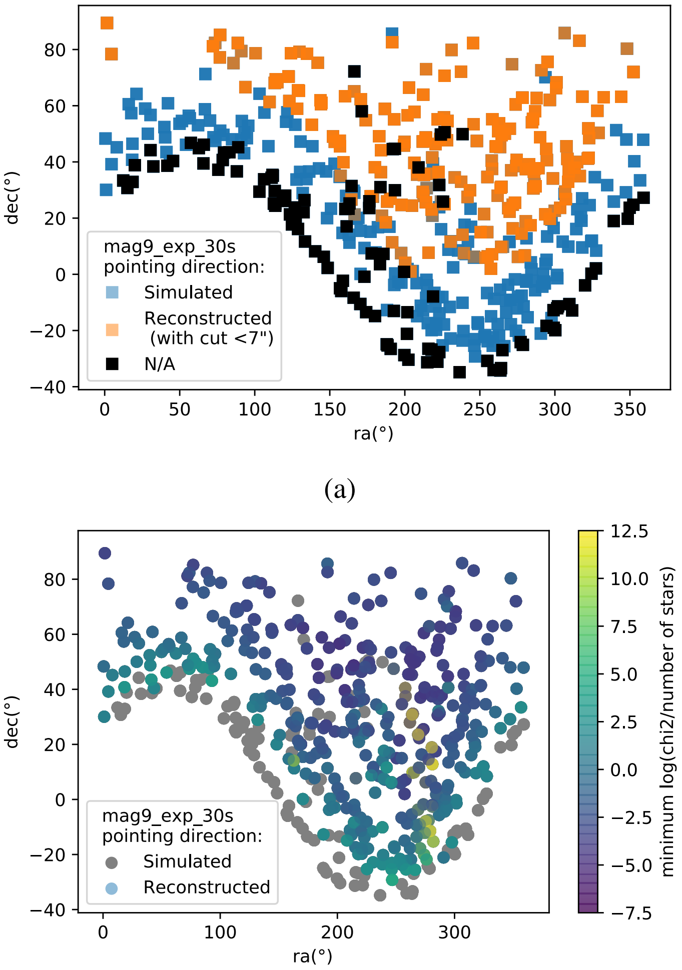

(a)

(b)

Fig. 6.28 (a): The simulated center (blue) of 500 simulations with stars simulated up to mag9 and exposure time 30s. Orange squares that overlap the blue squares are the reconstructed pointing direction with pointing accuracy < 7" by using the $\log(\chi^2/N)$ cut at -2. All images have been passed to the fitting model for 5 rounds. The data are plotted in semi-transparent color, thus the more solid the orange square is, the more time where the reconstructed center has the good pointing precision. The black squares are the simulated images that cannot be solved. (b): Same graph as above. The color indicates the value of $\log(\chi^2/N)$ of each reconstructed center. (Reconstruction including mask)

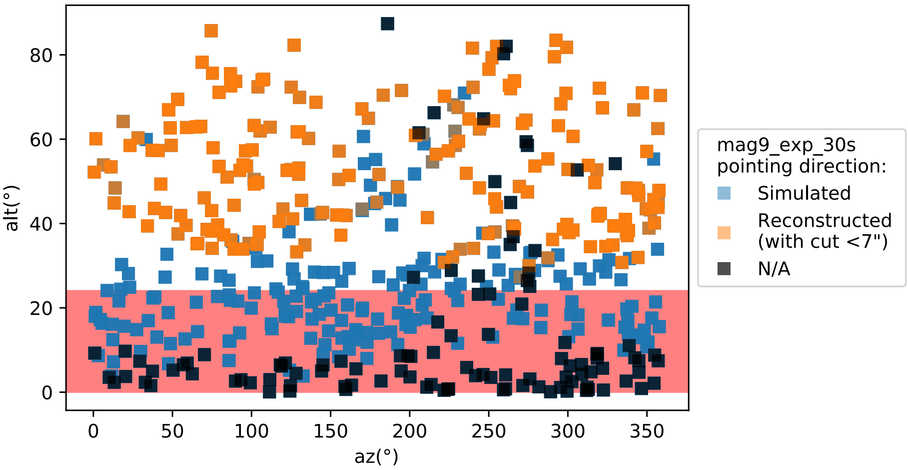

Fig. 6.29 Same graph as Fig. 6.28 (a) but in altaz-coordinates. The red region indicates that the elevation is smaller than 24°, which is too close to the horizon and below the required observation angle of the MSTs. (Reconstruction including mask)

By further increasing the required elevation to larger than 35°, there are 216 images left. 182 of them can be reconstructed precisely (< 7") with the cut and 14 images cannot be solved. After excluding the images that cannot be solved, the high precision reconstruction (< 7") efficiency reaches 90%.

The summary of the results from both excluding and including mask area can be seen in Table 6.1.

III. Interpretation

As mentioned in Section 6.4.1, the pointing accuracy is getting better if the camera points to the zenith and worse if it points to the horizon. This section further prove this argument, in which Fig. 6.26 (b) and Fig. 6.28 (b) show the generally smaller $\log(\chi^2/N)$ values when the camera points to the zenith, where the stars appear to be brighter and thus can be precisely extracted, which will at the end improve the pointing accuracy.

However it is surprising that the reconstruction including a mask area has greater percentage of precise reconstruction. One expects the reconstruction excluding mask area provides more star positions as the reference for the reconstruction, thus gives a more precise reconstruction result. Yet the distribution from Fig. 6.26 (b) and 6.28 (b) hardly agree with this assumption as the reconstruction with mask have in general even smaller $\log(\chi^2/N)$, which means the reconstructed spots fit even better to catalog star positions. By looking at the pointing accuracy distribution of the pointing directions that are precisely reconstructed (< 7") in Fig. 6.30, not only the percentage of precise reconstruction increases, the pointing

Table 6.1 Comparison of the reconstruction ability in the case excluding and including mask

Number of:	Reconstruction	
	Exclude mask	Include mask
Simulations	**500**	**500**
- After a cut at -2 [with accuracy < 7"]	147 [144]	213 [199)]
Simulations (elevation >24°)	**299**	**299**
- Exclude non-solvable images	299	278
- After a cut at -2 with accuracy < 7"	142	199
- Percentage of precise reconstruction	47.5 %	71.6 %
Simulations (elevation >35°)	**-**	**216**
- Exclude non-solvable images	-	202
- After a cut at -2 with accuracy < 7"	-	182
- Percentage of precise reconstruction	-	90 %

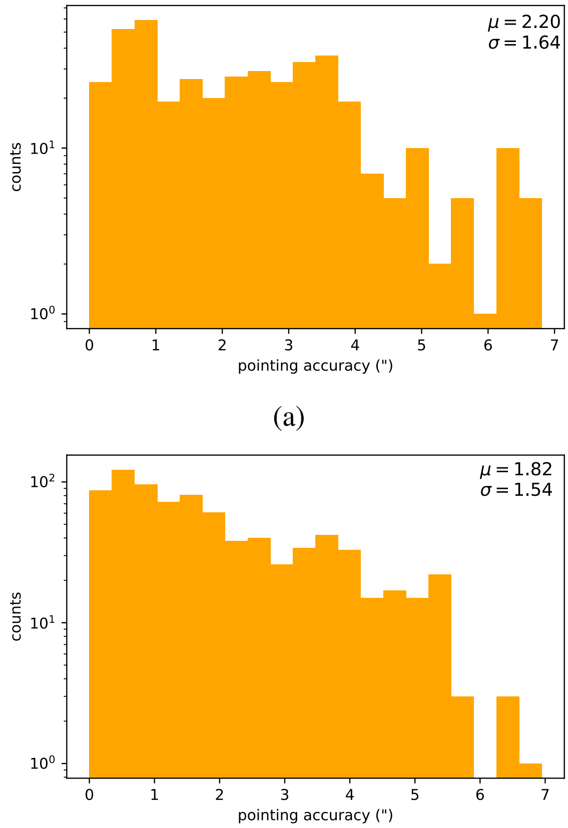

(a)

(b)

Fig. 6.30 The pointing accuracy distribution of reconstructed centers that have the pointing accuracy < 7". (a: Reconstruction excluding mask, b: Reconstruction including mask)

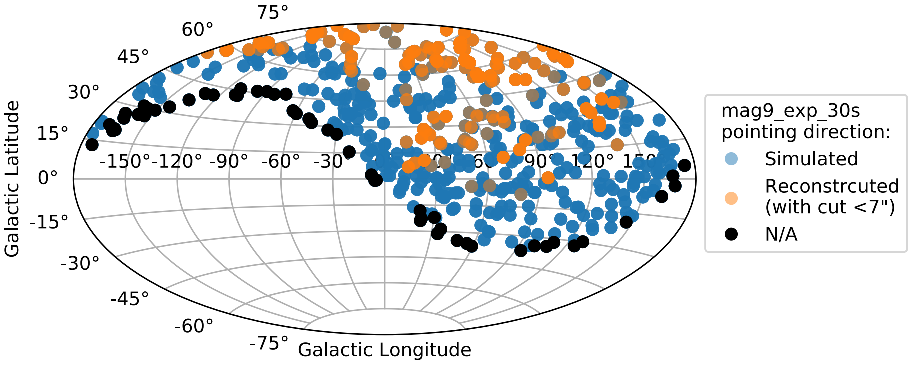

(a)

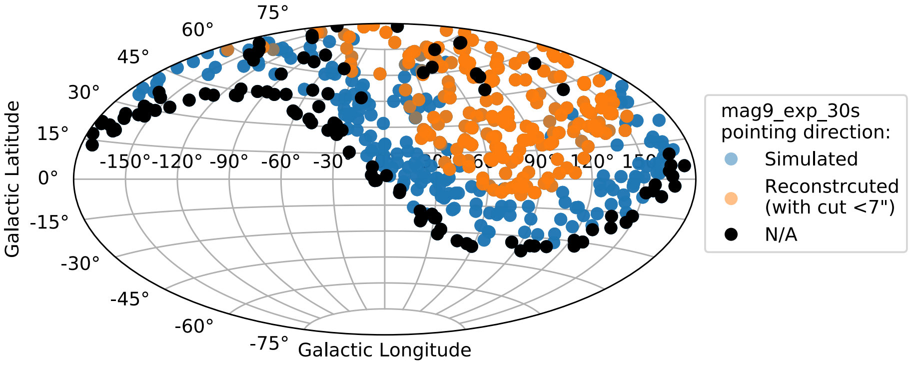

(b)

Fig. 6.31 Same graph as Fig. 6.27 and 6.29 but in galactic-coordinates. (a: Reconstruction excluding mask, b: Reconstruction including mask) accuracy distribution is closer to zero arcsecond when the reconstruction has included a mask area.

The reason for this result is related to the number of stars being input to the reconstruction tool. Fig. 6.31 shows the corresponding pointing direction in galactic-coordinates. In the case excluding the mask area, the pointing accuracy is worse when the pointing directions are close to the galactic plane. Most reconstruction at that region are either with pointing accuracy larger than 7" or only one out of five times where the pointing accuracy hits < 7" (the less solid orange spots). While the result is getting better when the pointing direction is at higher galactic latitudes where the number of stars are relatively less. As the fitting model will adjust fitting parameters based on the random seed until the χ^2 value reaches minimum or the fitting time reaches the specified time limit, the input of more stars to the model will require more fitting time and result in the fitting being terminated before the best fit is found. This is also the reason why the reconstruction is not good in all five rounds of fitting (the less solid orange spots) if the camera points near the galactic plane, since the random based fit cannot reach minimum χ^2 every time.

The above argument is further strengthen by looking at the case which includes the mask area, where only about 1/3 of original stars left. The pointing accuracy is still precise when the camera points to the galactic plane because the fitting model has more time to search for the best fit. On the contrary, the pointing accuracy is getting worse when the camera points away from the galactic plane. Firstly, there are more simulated images cannot be reconstructed. Secondly, the pointing accuracy at the top left corner in Fig. 6.31 (b) is hardly smaller than 7". These are either due to the fact that the number of residual stars are smaller than four in which a quad cannot be formed for the reconstruction or the few inaccurately extracted stars give a much great impact on the precision since the overall number of stars are less.

Notice one can see from Fig. 6.20 (a) and 6.26 (a) that there are more precisely reconstructed images with the exposure time of 20s at the elevation < 24° than that with the exposure time of 30 s. On the contrary, less images can be precisely reconstructed when the elevation is > 24° if the exposure time is at 20 s (even if only one round of reconstruction is done). This is because stars close to the horizon are relatively fainter and the increase in exposure time will increase the field of rotation which elongate the appearance of those stars. These add difficulties on the extraction. While at the region closer to the zenith, the elongation effect will be overcome by the brightness of the stars, giving a better extraction. As the MSTs will anyway point with an elevation > 24°, the exposure time of 30 s is still a good choice.

IV: Further Investigation: Deep into Optimization Algorithms

To ensure the dependency of the pointing accuracy and the fitting time, a further investigation is needed by directing looking at the optimization algorithms (their relationship has been discussed in Section 6.4.3). This can be done by examine the corresponding reduced χ^2 from each simulated images.

Fig. 6.32. show the 2D-histogram of $\log(\chi^2/N)$ versus the number of matches N from all four optimization algorithms for the case excluding and including the mask in 500 simulations. The number of solved images for both cases decreases to the same level in fit1 and fit2. This decrease is mainly due to the camera points to the horizon where no quad can be generated for the reconstruction. Since only the rejected result in fit2 will pass to fit3, this number further decreases in fit3 and reaches a minimum at fit4. Notice that there are in general less solved images for the case including mask because there are less extractable stars in those images for the reconstruction.

For the case excluding the mask, fit1 shows the number of matches ranging from 200 to 800 from all images. There is an obvious trend that $\log(\chi^2/N)$ is smaller if the number of matches is small. As the number of matches is related to the number of stars being input, this indicates a best fit is easier found if the number of input stars are small. This argument is further supported from the case including the mask, where only 1/3 of the original stars are extracted, there is a huge population of images with $\log(\chi^2/N)$ at around -2 which gives a good reconstruction result. Since the more the number of input stars requires a longer fitting time and that the current time limit is set to be 1 minute, this indicates that if there are too many input, the fit terminated before a best fit can be reached.

Notice there is a population of images with $\log(\chi^2/N)$ at around 15, these might be the images with the pointing direction too close to the horizon (elevation < 24 °) as indicated in Fig. 6.26 (b) and 6.28 (b).

As mentioned in Section 6.4.3, fit2 is done based on the re-matched results from fit1. The re-matching will remove the far off stars in fit1 and have chance to include the hidden stars. This can be seen in the graph where the overall number of matches decrease for the case excluding mask while increase for the case including mask. Both cases show a sudden increase of the population at $\log(\chi^2/N)$ around 15. This might be due to the re-matching process wrongly removed "good" stars, leading to fit2 perform badly.

Fit3 uses another optimization algorithm which is observed to be not as good as fit1 since the overall $\log(\chi^2/N)$ is larger than 0. Fit4, which is done based on the re-matched result from fit3, has again a sudden accumulation of population at $\log(\chi^2/N)$ around 15. This might be again due to the bad fitting result from fit3 leads to the re-matching process wrongly

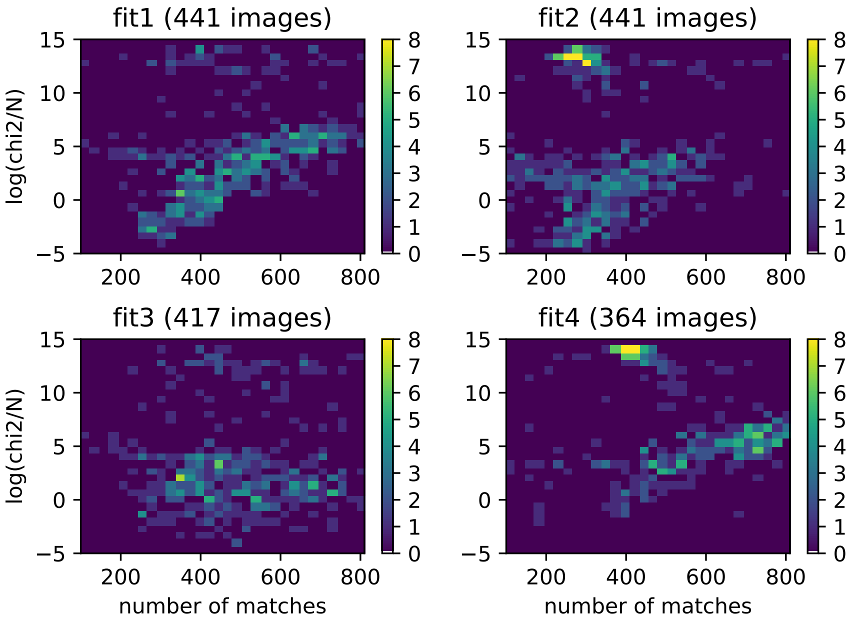

(a) Excluding mask

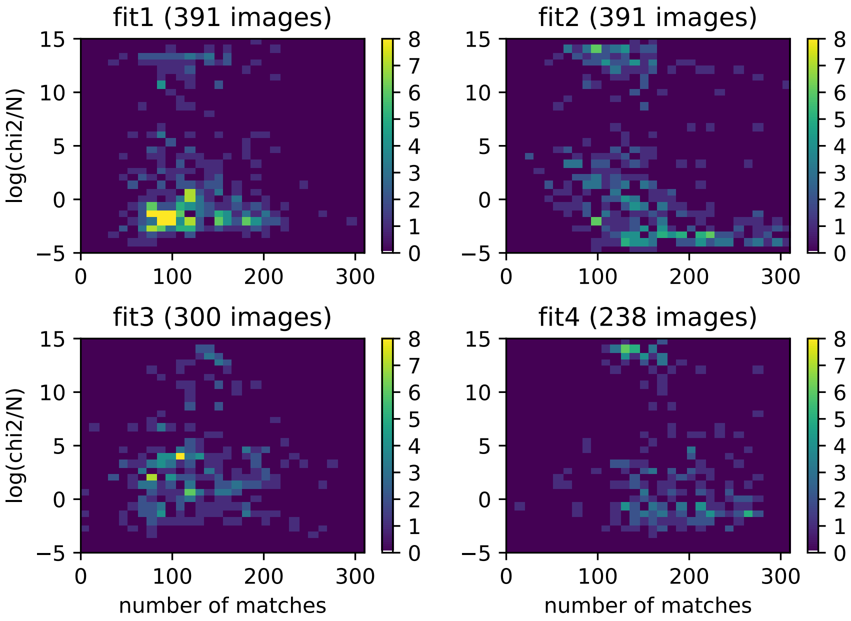

(b) Including mask

Fig. 6.32 $\log(\chi^2/N)$ versus N among 500 simulations for a whole round of reconstruction. The number of images indicates in each graph are the number of images that is able to be reconstructed in the specific optimization algorithm.

excludes "good" stars. Both fit3 and fit4 output only a few images with log(χ^2/N) below -2, indicates these two optimization algorithms are not so helpful in the reconstruction.

From this investigation, it is seen that only fit1 gives an obvious result that the number of matches (thus the number of extracted stars being input) is related to the fitting time. The core optimization algorithm from fit1 is generally better than that from fit3. It is also seen that the re-matching of stars always gives a sudden increase of number of bad reconstructed image. Since it is found that a log(χ^2/N) at -2 will gives a good reconstruction result, this corresponding to a level of $50 < N < 400$ (seen in Fig. 6.32) has higher chance to get a best fit without exceeding the time limit in fit1.

V. What We Know Now

To conclude, it is found that log(χ^2/N) is directly related to the pointing accuracy (Fig. 6.25). A log(χ^2/N) cut at -2 will generally gives a reconstructed result with high precision (< 7") (Table 6.1). The pointing accuracy is highly related to the number of stars being input for the reconstruction due to the fitting time (Fig. 6.32). The more the stars, a longer fitting time is needed and thus the higher chance that a best fit cannot be reached before times out. On the contrary when the number of stars are too small, it gives a greater impact from inaccurately extracted stars to the reconstruction (Fig. 6.31 (b)). Therefore it is very important to make a balance between having many stars as a reference points for the fitting and have less stars to facilitate the fitting process.

This section tells us the mask area that appears in the real application is no longer an obstacle for the reconstruction, it helps the reconstruction instead. What concerns next are how to extract the stars with even higher precision (i.e. changing the aperture, investigate how the presence of a mask image affects the extracted positions), how to shorten the fitting time (extending the time limit for the fitting is possible but we want to get a rapid reconstruction) and how to improve the optimization algorithm (i.e. try another optimization algorithm which the team is now working on). Yet these are beyond the scope of this thesis.

6.5 Application on Real Images

The CCD-camera was mounted onto the MST prototype in 2016 at Berlin (Adlershof) for image taking. Both the image taking time and the altaz-position of the telescope are given. Since the Cherenkov camera was not mounted on the MST prototype, the CCD-camera captured the mask from the camera support structure and about 1/3 of the image is covered as shown in Fig. 6.33.

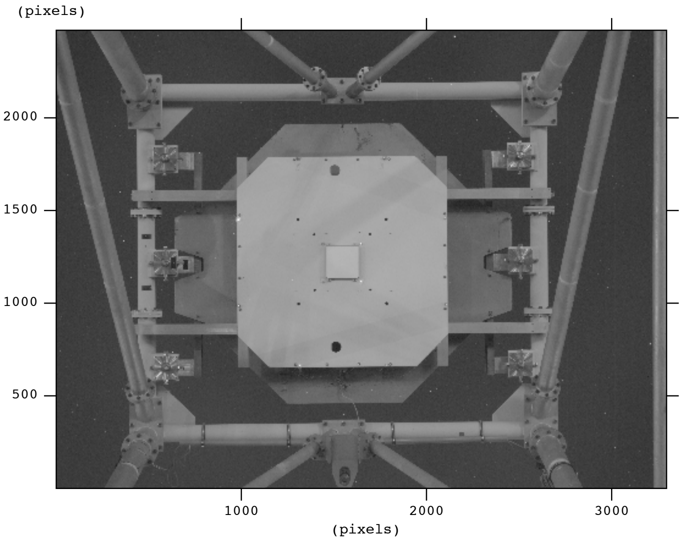

Fig. 6.33 Example of a real image taken by the CCD-camera mounted on the MST proptotype in Berlin (Adlershof)

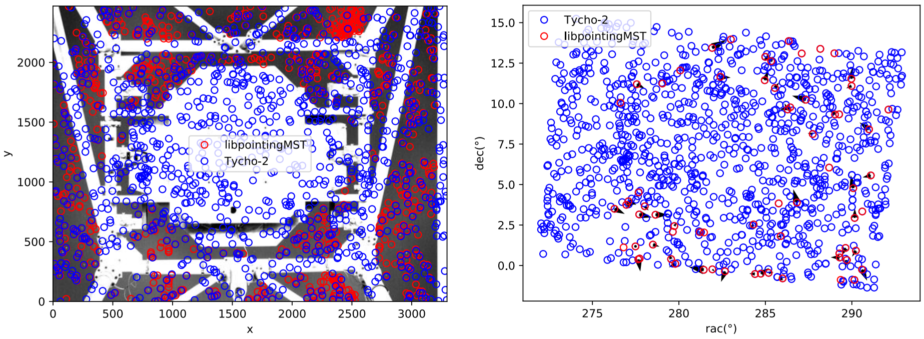

(a) (b)

Fig. 6.34 (a): The extracted spots(red) after using the star extraction tool with the optimized parameters tested in the simulation. The blue spots are the possible catalog stars position simulated by using the information of the camera axes and the image taken time. (b): The reconstructed position of the spots(red) and the simulated sky position of the catalog stars(blue). The arrow indicates the great circle distance difference.

The direct comparison of the reconstructed pointing direction and the CCD-camera optical axis is hard since the true orientation of the optical axis is not known. The optical axis of the camera is largely misaligned and tilted with respect to the nominal pointing of the telescope. Yet it is still interesting to see how the reconstructed center shift against the camera optical axis. Here the possible star positions are being simulated using the telescope optical axis position (this position is also expected to be hugely misaligned) and the date-time where the image was taken. By using the same optimized star extraction parameters as in

Section 6.3.2, one can see that there are too many noise spots being extracted as shown in Fig. 6.34 (a) and those spots are probably not precisely extracted, resulting in only few spots can be transformed into radec-coordinates through the reconstruction in Fig. 6.34 (b). The huge difference between the simulation and real image is the extra background noise in the real image, including the night sky background, the lighting system on the ground in the city and the reflected light from the camera support structure. Therefore it is highly encouraged to optimize the star extraction parameters in the real images. Yet this is beyond the scope of this thesis.

To investigate the working ability of **libpointingMST** on real images, 118 images taken in Adlershof are being examined. The images are accompanied with the corresponding information of the telescope axis. Fig. 6.35 shows the calculated telescope optical axes of the 118 images and the corresponding reconstructed center using **libpointingMST** with a $\log(\chi^2/N)$ cut at -2. Fig. 6.36 shows the minimum $\log(\chi^2/N)$ of each reconstructed center. The reconstructed center with $\log(\chi^2/N) < -2$ shifts against the telescope axis systematically. The pattern possibly arises from the misalignment of the camera axis to the telescope axis. Again a pointing model is needed to solve this problem, yet beyond the scope of this thesis.

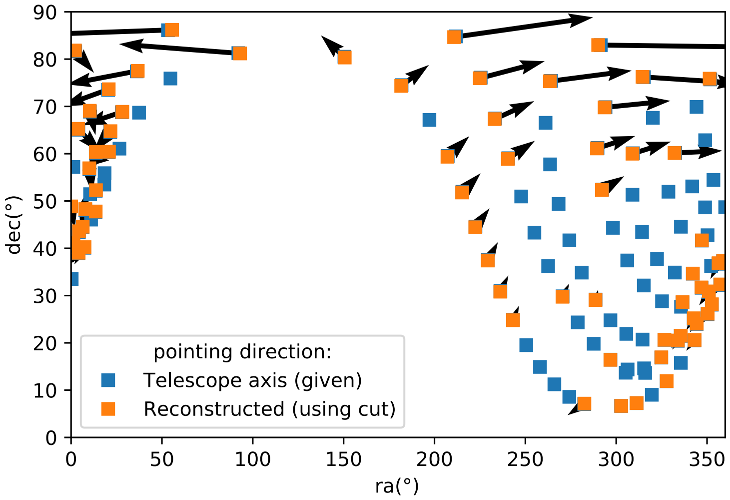

Fig. 6.35 The pointing direction of the 118 real images. Blue indicates the pointing direction derived from the telescope axis and orange indicates the reconstructed pointing direction with $\log(\chi^2/N) < -2$. The arrow indicates the difference in great angle distance between the blue and orange point, it is 72X enlarged.

Notice that it is expected that the great number of noise will give a big $\log(\chi^2/N)$ value, but the reconstructed pointing direction have in general small $\log(\chi^2/N)$. This might be due to the brightest stars are more favourable for the selection of quad. In the hypothetical matching process, the surrounding noise and faint stars are being rejected from the fitting

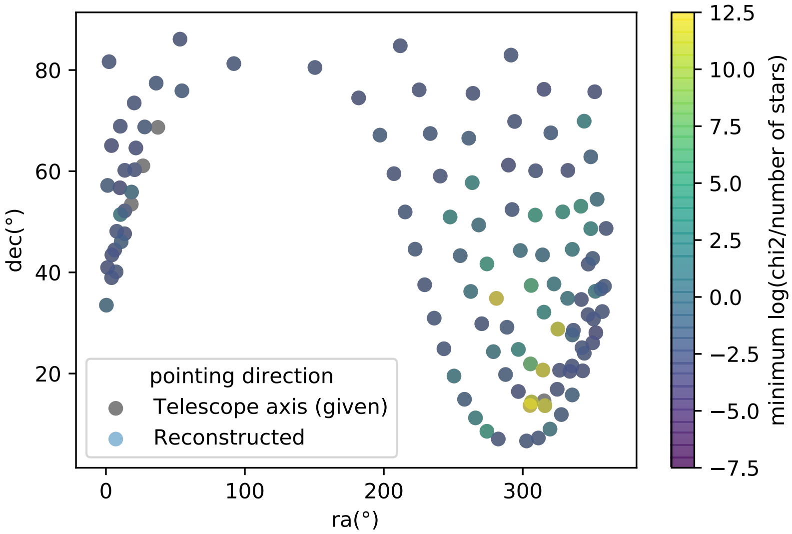

Fig. 6.36 The minimum $\log(\chi^2/N)$ value for the reconstructed pointing direction of the 118 real images.

model since they are far off the catalog star positions. This results in a smaller $\log(\chi^2/N)$ value than expected.

6.6 Chip Expansion on Simulation

To demonstrate the chip expansion effect in Chapter 4 on the pointing accuracy, an image with chip temperature -5.05 °C is simulated and the corresponding star positions are extracted. By using the equations of expansion factor derived in Section 4.2.2 and that assume the chip is glued at a single fixed point (2340.05, 2059.86), the corresponding star positions at chip temperature -23.2 °C is calculated. Fig. 6.37 shows the expansion effect on star positions with initial chip temperature set at -5.05 °C and being cooled down to -23.2 °C.

The reconstructed centers at chip temperature -23.2 °C with respect to the simulated center at chip temperature -5.01 °C can be seen in Table 6.2. The reconstructed pointing direction at chip temperature -23.2 °C is further away from the simulated pointing center as expected due to the chip contraction. Based on the experiment done in Chapter 4, it is expected that the pointing direction will shift by 1.6" when the temperature difference is 5 °C, thus a shift of 5.76" is expected in this temperature difference, which is 18 °C. However the best reconstructed center at chip temperature -23.2 °C shift away from the simulated center by 4.97" as indicated in Table 6.2, which is smaller than the expected 5.76". The possible reason is the reconstruction tool is able to twist and scale part of the spots in pixel-coordinates to radec-coordinates such that the chip expansion effect can be eliminated a bit. Since the

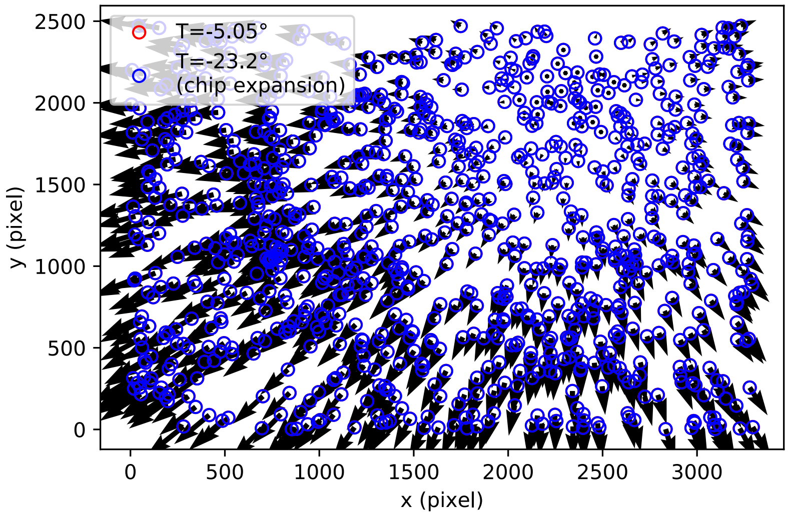

Fig. 6.37 A simulated image showing the pixel shift when cooling the chip from -5 °C to -23.2 °C. The black arrow indicates the direction of the shift, it is 329.6X enlarged.

Table 6.2 Summary of the best reconstructed center in the case of chip contraction.

Pointing direction from	Sky position		
	right ascension (°)	declination (°)	great circle distance ("")
Simulation (-5.05 °C):	282.383	7.05987	/
Reconstruction (-23.2 °C):			
round1	282.384	7.06083	4.97073
round2	282.384	7.06088	5.09752
round3	282.384	7.06087	5.07190
round4	282.384	7.06095	5.28022
round5	282.415	7.09247	163.838

expansion effect is not begin from the chip center, the fitting model cannot eliminate all the expansion effect by consider the radial symmetry.

This is certainly a challenge for the fitting model. Yet it is shown in Chapter 5 that the housing can ensure a stable chip temperature throughout the night time measurement of the telescope at La Palma, this inaccuracy will not appear in the real application.

6.7 Summary

In this chapter, the pointing analysis has been investigated with simulated and real images. The parameter for the star extraction tool have been optimized, where $t = 2$ and $s = [4, 500]$.

The matching efficiency for the star extraction tool from **libpointingMST** is 85 %, which is 10 % higher than that from **astrometry.net**. It is also found that the star extraction ability is maximal when the exposure time is at 20 s or above and the reconstruction ability is the best when the exposure time is at 30 s. Both the star extraction ability and the precision of the reconstructed pointing direction are hugely affected by where the camera points to. Pointing to the zenith gives the best spot matching efficiency and pointing accuracy, while pointing to the horizon gives the worse results.

The optimization algorithms in the fitting model have different behaviours. Yet, the overall precise reconstruction (< 7") efficiency for simulation without considering the mask area is 47.5 % when the camera points to an elevation above 24°, while that includes the mask area is 71.6 %. By pointing to an elevation above 35°, this number can even reach 90 % in the case with the mask. The discrepancy is related to the number of extracted stars, in which the less number of stars allows a best fit to be reached before the fitting is terminated. The pointing center can also be reconstructed in real images, however the pointing accuracy cannot be determined since the camera axis is unknown and the telescope axis is misaligned. A pointing model will be needed for further analysis, yet this is beyond the scope of this thesis.

Finally the effect of the chip expansion on the pointing accuracy is examined. The pointing direction shifted for 4.97" when the temperature difference is 18 °C, smaller than the expected 5.76" from the derived chip expansion factor in Chapter 4. Yet the housing in Chapter 5 ensures no chip expansion effect in the real application.

Chapter 7

Summary and Outlook

In this thesis, the Single-CCD concept has been investigated. The single-pointing CCD-camera has been characterized and optimized. The chip expansion effect on the image aberration has been explored and the expansion factor of the CCD-chip is determined. The pointing accuracy will be affect by 1.6" if the chip temperature changes for only 5 °C, this urges the need to keep the chip temperature constant throughout the measurement on the MSTs. To do so, a housing is built to protect the CCD-camera that will be mounted on the MSTs mirror dish and ensure the chip temperature can stays constant. The CCD-camera can operate well at the extreme working temperature range of MSTs at $-10\ ^\circ\mathrm{C} < T_{ambient} < 30\ ^\circ\mathrm{C}$, the chip temperature of -23 °C is proven to be stable throughout the working temperature range in the temperature chamber and at the nighttime measurements in La Palma. The new glass heater design also ensures that no condensation will occur on the glass surface of the housing when the humidity is below 90 %, such that the image taking process will not be affected. Finally the reconstruction ability of the CCD-camera using the library **libpointingMST** is examined. The star extraction ability of **libpointingMST** is 10 % higher than that of **astrometry.net**. The precise reconstruction (< 7") efficiency for the simulation with the consideration of the mask is 71.6 % if the camera points to the elevation above 24° and that without considering the mask is 47.5 %, indicating the less number of extracted stars will actually improve the reconstruction. By further increase the pointing elevation to above 35°, the precise reconstruction efficiency even reach 90 % for the case included the mask area. The working ability of **libpointingMST** is also tested on real image and the chip expansion effect on the reconstruction is examined.

For a more detailed study, it is suggested to increase the time limit for the reconstruction to investigate the ultimate fitting ability from all the four optimization algorithms in the fitting model. To avoid a fitting being terminated before a best fit is found, it is also important to improve the optimization algorithm in order to fasten the fitting process. The team is right now trying different optimization algorithms to improve the reconstruction model.

Also since the present of mask will affect the background distribution and thus the spots extraction, it will be good to know how these are correlated to the pointing accuracy. As it is found that the quality of extracted positions is more crucial than the number of extraction, it will be also interesting to look at how other CCD geometry will affect the extraction quality, for example by changing the aperture. Since the effect of star deformation is seen in real images, it is also important to include this to the simulation.

In the real application, the star extraction parameters should be optimized before use due to the existence of the night sky background. Although the pointing center can also be reconstructed in real images, the pointing accuracy cannot be determined since the camera optical axis is unknown. Yet the shifts of the reconstructed center with the calculated telescope optical axis follow a certain pattern, suggesting a pointing model should be built in order to derive the pointing accuracy.

The reconstructed center shifts for 4.97" when the chip temperature decreases for 18 °C by considering the chip expansion effect demonstrated in Chapter 4. This effect cannot be eliminated by the current fitting model since the expansion is not symmetric. Though the test performed in Chapter 5 ensure a stable chip temperature at the nighttime measurement in La Palma, one may still consider to include the chip expansion factors into the fitting model for safety.

References

[1] Aharonian, F. A. (2004). *Very High Energy Cosmic Gamma Radiation*. World Scientific.

[2] Ambrogia, L., Wilhelmib, E. D., and Aharonian, F. (2006). On the potential of atmospheric cherenkov telescope arrays for resolving tev gamma-ray sources in the galactic plane. *Astroparticle Physics*, 80:22.

[3] Bernlöhr, K. (2013). Monte carlo design studies for the cherenkov telescope array. *Astroparticle Physics*, 43:171.

[4] Bolton, D. (1980). The computation of equivalent potential temperature. *Monthly Weather Review*, 108:1046–1052.

[5] CTAConsortium (2011). Design concepts for the cherenkov telescope array cta: an advanced facility for ground-based high-energy gamma-ray astronomy. *Experimental Astronomy*, 32:193.

[6] CTAConsortium (2018). Science with the cherenkov telescope array. *World Scientific*, 1:12–27.

[7] CTAWebsite (2018). https://www.cta-observatory.org/project/technology/.

[8] Gaug, M. (2014). Calibration strategies for the cherenkov telescope array. *Proceedings of the SPIE*, 9149.

[9] Gillessen, S. (2003). Arcsecond level pointing of the h.e.s.s. telescopes. *Proceedings of the 28th International Cosmic Ray Conference*, 1:2899.

[10] Griffith, C. A. (2016). Charge coupled devices. *https://www.lpl.arizona.edu/~griffith/ptys521/2-CCD-Detectors.pdf*.

[11] Herpich, J. (2010). *Testing a Single-CCD-Concept for the H.E.S.S. II Pointing*. Ruprecht-Karls-Universität.

[12] Hofmann, P. (2015). *Entwicklung eines SingleCCD-Gehaeuse-Prototypen im Hinblick auf thermische Eigenschaften*. Friedrich-Alexander-Universität Erlangen-Nürnberg.

[13] Lang, D., Hogg, D. W., Mierle, K., Blanton, M., and Roweis, S. (2010). Astrometry.net: Blind astrometric calibration of arbitrary astronomical images. *The Astronomical Journal*, 139:5.

[14] Longair, M. S. (1992). *High Energy Astrophysics*, volume 1. Cambridge University Press.

[15] Mazin, D. (2015). Ground-based detectors in very-high-energy gamma-ray astronomy. *Comptes Rendus Physique*, 16:6.

[16] Molenaar, A. (2005). Pointing accuracy of h.e.s.s. cherenkov telescopes. *http://cops.tnw.utwente.nl/pdf/slides/HESS_Cherenkov_telescopes.pdf*.

[17] NASAWebsite (2018). Tycho-2 catalog. *https://heasarc.nasa.gov/W3Browse/all/tycho2.html*.

[18] Oakes, L., Garczarczyk, M., Kaphle, S., and Mayer, M. (2017). Techniques and results for the calibration of the mst prototype for the cherenkov telescope array. *AIP Conference Proceedings*, 1792(8):11.

[19] Okada, Y. and Tokumaru, Y. (1984). Precise determination of lattice parameter and thermal expansion coefficient of silicon between 300 and 1500 k. *Journal of Applied Physics*, 56:314.

[20] Ong, R. A. (1998). Very high-energy gamma-ray astronomy. *Physics Reports*, 305:3.

[21] Panter, M. and Puehlhofer, G. (1998). Precision determination of source location with the hegra iact system. *https://www.mpi-hd.mpg.de/hfm/CT/talks/panter_kruger.ps.gz*.

[22] Pühlhofer, G. (2017). The medium size telescopes of the cherenkov telescope array. *AIP Conference Proceedings*, 1792(8):2.

[23] Pühlhofer, G., Daum, A., Hermann, G., Hess, M., Hofmann, W., Koehler, C., and Panter, M. (1997). Locating tev gamma-ray sources with sub-arcminute precision: the pointing calibration of the hegra system of imaging atmospheric cherenkov telescopes. *Astroparticle Physics*, 8:101–108.

[24] Stecker, F. W., Tsuruta, S., and Fazio, G. G. (1967). The production of cosmic gamma rays in interstellar and intergalactic cosmic-ray collisions. ii: the effects of the decay of nucleon isobars and hyperons on the cosmic gamma-ray spectrum. *SAO Special Report*, 12:1.

[25] Tiziani, D. (2015). *Investigations towards a Single-CCD Pointing-Solution for the Medium-Sized Telescopes of the Cherenkov Telescope Array*. Friedrich-Alexander-Universtät Erlangen-Nürnberg.

[26] Völk, H. J. and Bernlöhr, K. (2009). Imaging very high energy gamma-ray telescopes. *SAO Special Report*, 25:173.

Appendix A

CCD-Camera Specifications

AIS Apogee IMAGING SYSTEMS

ASPEN® CG8050 & CG8050C
High Performance
Cooled CCD Camera System

DESCRIPTION

Aspen® is the newest in design innovation from Apogee Imaging Systems. Aspen® increases cooling performance in a smaller package, improves stray light baffling, adds a Network interface with a built-in web server, supports dual output CCDs up to 16Mhz and sets a new standard in shutter reliability. The Aspen® CG8050 has a 8-megapixel format interline transfer sensor with low noise and high quantum efficiency. The camera is available with a monochrome (CG8050) or color (CG8050C) sensor. Small pixels are ideal for microscopy. All Aspen® systems are backed by a 2 year warranty on the camera and lifetime warranty on the CCD chamber integrity.

SYSTEM FEATURES

- 1 to 16 MHz 16-Bit digitization
- USB and Ethernet interface
- Programmable cooling up to 65°C below ambient
- High reliability shutter (>5 million cycles)
- 32 MByte camera memory
- Subarray readout and fast sequencing modes
- Adjustable fan speed for low/zero vibration
- General purpose programmable I/O port
- Programmable status indicators
- 32/64 bit ActiveX drivers included
- Field upgradeable firmware
- AR coated silica windows
- Liquid cooling option
- Precision locking filter wheels optional

Imaging area of CCD

18.1 x 13.6mm

CCD SPECIFICATIONS

CCD	Kodak KAI-8050
Array Size (pixels)	3296 x 2472
Pixel Size	5.5 x 5.5 microns
Imaging Area	18.1 x 13.6mm (246.5mm^2)
Imaging Diagonal	22.6mm
Linear Full Well (typical)	20K electrons
Dynamic Range	64 dB
QE at 400nm	32%
Peak QE (500nm)	50%
Anti-blooming	300X

CCD SENSITIVITY

Fig. A.1 CCD specifications (source: https://alliedscientificpro.com/web/content/product.attachment/741/product_attachment/name)

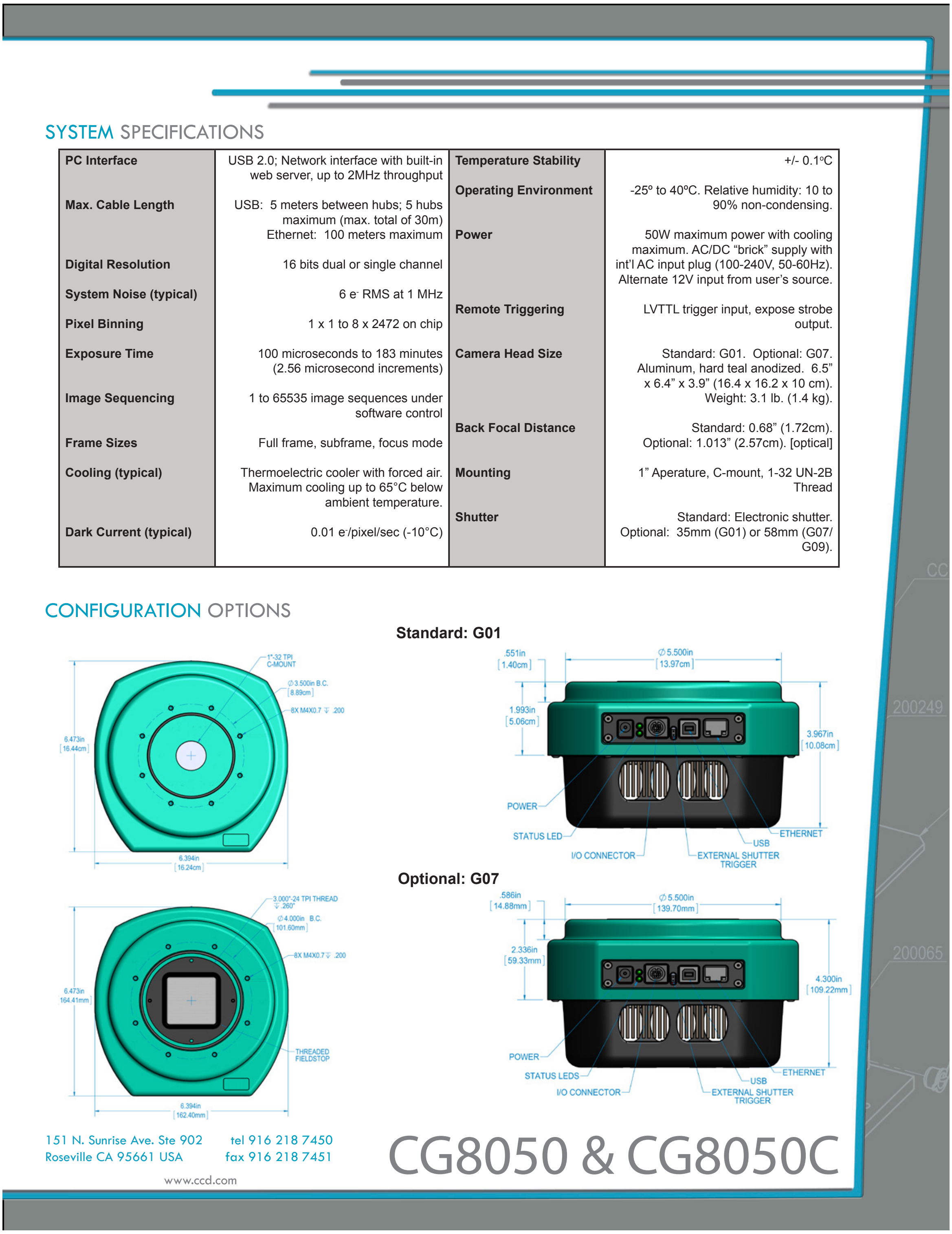

SYSTEM SPECIFICATIONS

PC Interface	USB 2.0; Network interface with built-in web server, up to 2MHz throughput	**Temperature Stability**	+/- 0.1°C
Max. Cable Length	USB: 5 meters between hubs; 5 hubs maximum (max. total of 30m) Ethernet: 100 meters maximum	**Operating Environment**	-25° to 40°C. Relative humidity: 10 to 90% non-condensing.
Digital Resolution	16 bits dual or single channel	**Power**	50W maximum power with cooling maximum. AC/DC “brick” supply with int’l AC input plug (100-240V, 50-60Hz). Alternate 12V input from user’s source.
System Noise (typical)	6 e$^-$ RMS at 1 MHz	**Remote Triggering**	LVTTL trigger input, expose strobe output.
Pixel Binning	1 x 1 to 8 x 2472 on chip	**Camera Head Size**	Standard: G01. Optional: G07. Aluminum, hard teal anodized. 6.5” x 6.4” x 3.9” (16.4 x 16.2 x 10 cm). Weight: 3.1 lb. (1.4 kg).
Exposure Time	100 microseconds to 183 minutes (2.56 microsecond increments)	**Back Focal Distance**	Standard: 0.68” (1.72cm). Optional: 1.013” (2.57cm). [optical]
Image Sequencing	1 to 65535 image sequences under software control	**Mounting**	1” Aperature, C-mount, 1-32 UN-2B Thread
Frame Sizes	Full frame, subframe, focus mode	**Shutter**	Standard: Electronic shutter. Optional: 35mm (G01) or 58mm (G07/ G09).
Cooling (typical)	Thermoelectric cooler with forced air. Maximum cooling up to 65°C below ambient temperature.		
Dark Current (typical)	0.01 e$^-$/pixel/sec (-10°C)		

CONFIGURATION OPTIONS

Standard: G01

Optional: G07

151 N. Sunrise Ave. Ste 902
Roseville CA 95661 USA

tel 916 218 7450
fax 916 218 7451

www.ccd.com

CG8050 & CG8050C

Fig. A.2 System specifications (source: https://alliedscientificpro.com/web/content/product.attachment/741/product_attachment/name)

Appendix B

Parameters for the Simulation

The list of parameters input to the simulation (from **libpointingMST** written by Domenico Tiziani):

- Exposure time [s] used for images. Typical value used in this thesis is 20 s or 30 s
- Aperture (f-number) used for images. Typical value used in this thesis is 7.3
- Focal length [m] of objective. Default value: 50e-3
- Photon collecting efficiency of simulated camera. Default value: 0.5
- Factor for size of confusion circles used for images. Default value: 1
- Altitude-range. Typical value used in this thesis is [0, 360]
- Azimuth-range. Typical value used in this thesis is [0, 90]
- Simulated CCD-Temperature [°C]. Typical value used is -5 °C
- Start-time. Typical value used in this thesis is "2018-05-22 23:00:00"
- Camera-edge. Default: no camera simulated
- Maximum magnitude of stars simulated. Typical value used in this thesis is 9
- Default: simulate atmospheric refraction
- Default: simulate horizon

Appendix C

Parameter Optimization for libpointingMST

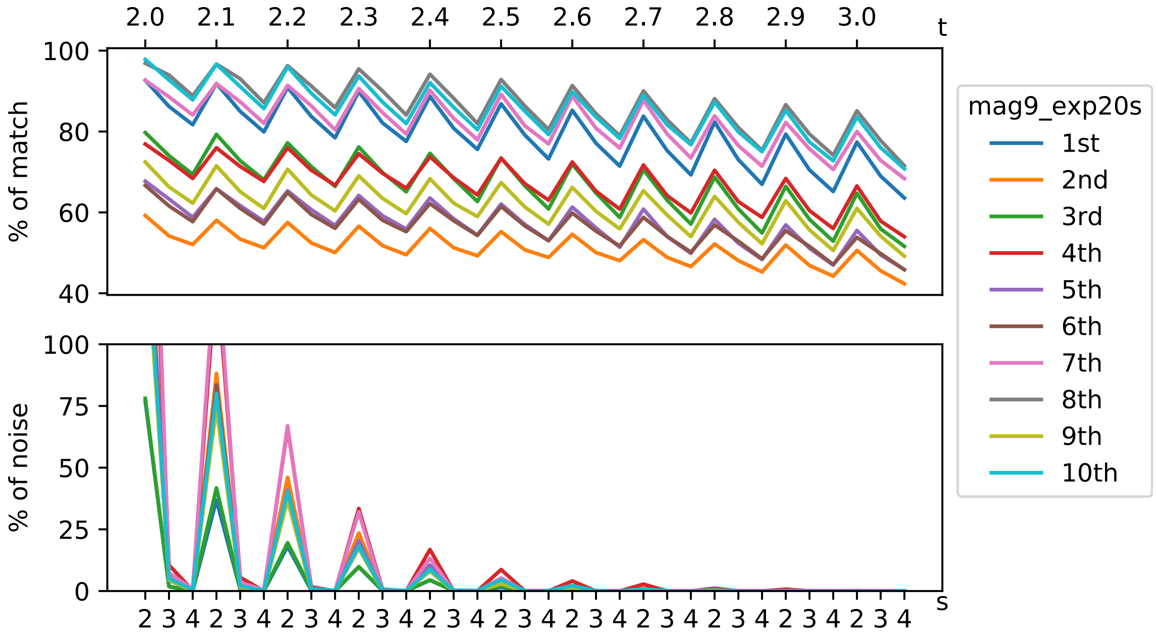

Fig. C.1 Parameter optimization of the star extraction tool from **libpointingMST** for different *t* and the lower limit of *s*. The ratio of matches and noise are shown on the y-axis. The top x-axis indicates the different values of *t* and the bottom x-aixs indicates the lower limit of *s*. The different line colors represent different simulated images.

Appendix D

Nonlinear Optimization for the Fitting

The following explanation of the algorithm is from the website https://nlopt.readthedocs.io/en/latest/NLopt_Algorithms/.

Fit1, fit2 and fit4 use the Controlled Random Search (CRS) algorithm with local mutation, which is a global derivative-free optimization. It stars with a random set (or population) of points and randomly evolve these points by heuristic rules.

Fit3 uses the Multi-Level Single-Linkage (MLSL) algorithm, which is a global derivative-free optimization using a sequence of local optimization from random starting points. It also uses the Constrained Optimization by Linear Approximations (COBYLA), which is a local derivative-free optimization utilize the successive linear approximations of the objective function.

Acknowledgements

Many kind and benevolent people have been met. They have been enlightening and accompany me throughout my studies. Here I would like to express my special thanks of gratitude to the following people:

- Prof. Dr. Christopher van Eldik for offering me this interesting topic and always encouraging and patient to discuss my work. Your valuable advice have enlighten many ideas in this thesis.
- Prof. Dr. Stefan Funk to be the second referee of this thesis and always friendly in the group.
- Domenico Tiziani for spending so much time on guiding me to use the CCD-camera and to understand the algorithm from **libpointingMST** and have solved so many technical issues. This work cannot be done without you indeed.
- Dr. Johannes Veh for always helpful and giving advice on organizing my work.
- Andreas Specovius and Giacomo Principe for giving joy to our office.
- The whole Gamma group for the friendly atmosphere and many memorable activities. It is my pleasure to join such an amazing group.
- Everyone in the ECAP for always glad to help me when I confront any issues. The staffs in the electronic workshop and the security team helped me a lot during the housing measurement.
- My parents and brother who always love, support and believe in me.

Declaration

I hereby declare that except where specific reference is made or quoted in the thesis, this thesis is my own work and contains no sources or aids from others. The contents of this thesis are original and have not been submitted for consideration for any other degree or qualification in this, or any other university.

Yu Wun Wong
Erlangen, 28 September 2018